Static and fatigue propagation of buckle-driven delaminations under bending and compressive loads

Kinawy, Moustafa

Award date:
2011

Awarding institution:
University of Bath

Static and Fatigue Propagation of Buckle-Driven Delaminations under Bending and Compressive Loads

Moustafa Kinawy

A thesis submitted for the degree of Doctor of Philosophy
University of Bath
Department of Mechanical Engineering

2011

COPYRIGHT

Moustafa Kinawy

Abstract

Impact damage to composites is a major concern for many industrial sectors such as aerospace, automotive and marine. Damage such as fibre breakage, matrix fracture and sub-layer delaminations may occur, where the latter is considered the most critical under compressive loading. Compression after impact (CAI) in composites has been extensively studied by researchers to predict the strength of the impacted laminate. So far, however, various numerical techniques were developed to predict the CAI strength. There is a considerable demand for analytical approximate models that could be utilised in the early stage of the design process rather than implementing time-consuming numerical methods. The present work focuses on buckle-driven delamination of impact-damaged composites. The study included experimental and analytical investigations for two different laminate configurations: sandwich composites under edge compression and solid laminates under pure bending.

The first part of the work investigated the behaviour of impacted foam-core sandwich specimens with composite laminated faces under uni-axial compression. The applicability of two pre-developed analytical models to predict the failure strain under static and fatigue loading was examined. Both models assumed that the thin sub-laminate damage existed within the laminate. This could be modelled as a plate structure prone to buckle and the propagation of such damage depended on its buckling strain. The propagation occurred in the load direction. An elliptical plate pattern resembling the damage morphology was incorporated into the static model and showed good agreement. Another modelling strategy was utilised to predict the fatigue failure strain by modelling it as a circle encompassing the whole damage and compared against the experimental fatigue trends for the studied laminate.

In order to verify the analytical model results, an initial experimental testing programme was carried out to establish a suitable setup that fulfilled the assumptions of both models. The main testing programme was then performed on the finalised specimen configurations under static and fatigue loading. The comparison between experimental and analytical models showed good agreement. Testing of specimens with two different face laminates, $[(\mp 45_C)_2,(90_C,90_G)_4,(\mp 45_C)_2]$ and $[(\pm 45_C)_2,(0_C,0_G)_4,(\pm 45_C)_2]$ showed two distinctive face delamination behaviours: opening and closing. A Digital Image Correlation (DIC) system was used to monitor the face damage propagation during loading. Two distinct failure behaviours were observed for each specimen leading to different fatigue resistance: the $[(\mp 45_C)_2,(90_C,90_G)_4,(\mp 45_C)_2]$ laminate showed an opening propagation of a

delamination while the $[(\pm 45_C)_2,(0_C,0_G)_4,(\pm 45_C)_2]$ laminate showed closing propagation. The failure modes and critical levels of static load causing face damage propagation were determined experimentally in both static and fatigue testing.

The second and third parts of the work were concerning bending of delaminated solid laminates. Through-width delaminated specimens were initially tested under four-point static and fatigue bending. A pre-developed non-linear kinematic model was initially utilised to explore the deformation behaviour of the thin sublaminate. The analytical model was then extended to include a mixed-mode propagation strategy in order to predict the propagation moment for three different lay-up configurations.

Fractography analysis was performed to distinguish between Mode-I and Mode-II contribution to the final failure of specimens. Comparison between experimental results and analysis showed agreement to within 5% in static propagation moment for two different materials. It is concluded that static fracture is almost entirely driven by Mode-II effects. This result was unexpected since it arises from a buckling mode that opens the delamination. For this reason, and because of the excellent repeatability of the experiments, the method of test may be a promising means of establishing the critical value of Mode-II fracture toughness, G_{IIC} of the material. Fatigue testing on similar samples showed that buckled delamination resulted in a fatigue threshold that was over 80% lower than the static propagation moment. Such an outcome highlights the significance of predicting snap-buckling moment and subsequent propagation for design purposes.

The final part was to experimentally investigate impacted composite plates under static and fatigue bending. The initial study included the establishment of a threshold impact energy level on the studied laminate. Static and fatigue testing were then performed. Specimens with circular embedded delamination were investigated to study the behaviour of single delaminations as a possible idealised methodology to understand delaminated two-dimensional plates under bending.

Acknowledgements

I would like to thank the Great Western Research (GWR) foundation, Agusta Westland UK, and Rolls-Royce plc for their financial support of my PhD. I would also like to thank Dr. Andrew Rhead, Mr. Neil Baker and Prof. Giles Hunt for their valuable support and advice on the analytical side of this work.

I would like to express my sincere appreciation to Dr. Richard Butler for his continuous support, supervision and guidance through the course of the work.

Finally I would like to dedicate this work to my wife Marwa and my sons Hamza and Rayan for their patience and sacrifice throughout the duration of this work.

Contents

List of Figures

List of Tables

List of Abbreviations

BVID	Barely visible impact damage
PTFE	Poly tetra fluoro ethylene
DIC	Digital image correlation
ESM	Electron scanning microscopy
DCB	Double cantilever beam
SERR	Strain energy release rate

Chapter 1

Introduction

Composite materials are a combination of two or more different materials having a distinct interface separating them. Such combination enables the new material to possess a high strength to weight ratio. A narrower definition of composites is restricted to those combinations of materials that contain high strength fibre reinforcements supported by high performance matrix materials. Both fibres and matrix materials could be of organic or inorganic in their chemical makeup. The fibrous reinforcement material is referred to as the discontinuous phase and the matrix material as the continuous phase. The primary engineering properties of the composite are derived predominantly from the mechanical and physical properties of the discontinuous phase, the fibre reinforcement. These are the fibre dominated properties of the composites. Composite materials are becoming substantial in many industrial applications, such as aerospace and aeronautical engineering, marine structures and automotive bodies. Understanding how these materials behave under different conditions and loads takes considerable attention from researchers and different companies who utilise their use. Hence, the study of failure of composite materials is of paramount importance for the safety of the final product. Different damage types are combined to composites because of their nature. The main failure encountered in composites is the interface separation within the layers, viz. Delamination, which is caused by difference between interlaminar tension, compression and shear stresses. Fibre fracture, matrix cracking and delamination are different modes of composites failure. The latter is considered one of the most critical failures. Such failures may be resulting from manufacturing faults or in-service accidents. An impact of the composite

part may lead to either apparent damage or a barely visible one, i.e. the damage is potent beneath the surface and not seen. Certain loading of the part may lead this inner damage to progress and result in a significant decrease of the stiffness and hence catastrophic failure.

Delamination is a common failure in composite. It becomes more critical under compression loading which leads the weaker separated sub-laminate to buckle and then the damage to further progress. Buckling induced propagation of delaminations is considered one of the critical causes of failure of damaged composites. This can arise from manufacturing faults or during service where low velocity impact damage can result in barely visible sub-layer delaminations. Such delaminations significantly decrease the load carrying capacity of the structure concerned.

A growing need in the aerospace industry is to have quick and efficient analytical tools for physical insight of damaged composites. Such tools are instrumental in the preliminary analysis phase to study damage tolerance of possible delamination scenarios.

1.1 Literature review

1.1.1 Impact of composite laminates

Low velocity impact damage can induce a barely visible indentation which includes internal layer separation within the laminate surface. It was reported in many studies that barely visible impact damage (BVID) caused by low velocity impact may result in up to 60% drop in the residual compression strength of composite structures [1].

Several researches were carried out to study the impact damage morphology of composite laminates. The influence of the reinforcement types on the impact damage morphology and its subsequent effect on the compression after impact strength was investigated by Bibo & Hogg [2] and [3]. They concluded that the damage spread across the thickness in a conical form, i.e. the damage separation size increased across the thickness as the depth increased from the impact spot.

They also found that the specimen with low bending rigidity exhibited smaller impact damage size than less flexible ones. This was due to the fact that a flexible structure dissipated more impact energy into deformation. Greenhalg et al [4] suggested that the delamination damage growth in a composite laminate due to impact was aligned with the fibre direction of the lower sub-laminate at the interface.

Choi & Chang [5] investigated the damage of graphite/epoxy laminated composites caused by low-velocity impact. From their experiments, they reported that once the delamination is initiated from a matrix crack, it grows mostly along the fibre direction of the bottom layer at the interface following the contours of interlaminar shear stress σ_{xz} and σ_{yz} which explains the characteristic "peanut" shape of the damage.

Bouvet & Barrau [6] developed a numerical technique to predict the damage pattern within a composite laminate due to low velocity impact. They assumed that at any interface of a damaged laminate, the propagation of the delamination depended on the fibre direction of the lower layer, i.e. the tension created in the lower layer due to the exerted pressure by the impactor results in an interlaminar opening at this interface. The model also suggested that when fibre failure occurred in a certain direction, the overall stresses decreased in this direction and then resulted in delamination growth in the perpendicular direction. Their technique was found to well predict the damage morphology compared to C-Scan images for different types of tested laminates.

Freitas et al [7] studied the damage growth mechanisms for carbon fibre laminates under impact loading. They investigated the impact of two different laminates and two different resin systems, T800 and 977-2, respectively. The resulted damage area was compared to a FEM strategy. Two quasi-isotropic layups, $[+45_3/0_3/-45_3/90_3]_s$ and $[+45/0/-45/90/+45/0_2/-45_2/90_2]_s$, were manufactured from each resin systems. A semi-spherical impactor of 16 mm diameter was used for the impact tests. The specimens were fixed in a standard fixture with an opened window of 122×75 mm and impact were carried out under different levels. After each impact, a C-Scan technique was employed to identify the damaged area. The initial outcome showed that the 977-2 resin specimens were less tough than the T800 laminates. Two significant morphologies were visualised; the first laminate types had a non-symmetric damage morphology where

damaged areas constructed a spiral peanut shape per each layer band. The damage areas increased in size when moving towards the back face. The damage for the second laminate, $[+45/0/-45/90/+45/0_2/-45_2/90_2]_s$, had a spiral peanut shape repeated across each interface. Another difference observed in the first laminate, where the layers were grouped in three layer bands, the damage peanut shapes were bigger than the other laminate as the depth between each interface is bigger than the other laminate. In both laminates, the whole damage shape was approximately encompassed by a circle. It was found that the area of the damage in the tougher resin, T800, was much bigger than that in the 977-2 resin. Furthermore, the second laminate was more damage tolerant as it had more layer interfaces. Another significant outcome was that the main factors affected the damage distribution were the transverse stresses through the thickness and the Mode-II fracture toughness, G_{IIC}. Moreover, the variation of the transverse stress depended on the linear distance of the interface from the neutral axis of the laminate. As the distance increased, the delamination horizontal width increased.

A large volume of research has been conducted to predict area of impact damage against impact force or energy. Davies & Zhang [8] predicted the limit of internal damage in carbon fibre laminates when subjected to low velocity impact. They evaluated the damage area vs. impact forces and energies for different thicknesses. They then introduced a simple analytical formula to evaluate the impact force sufficient for establishing delamination of the layers of laminates. The analytical relation was obtained in terms of impact force, thickness and the interlaminar shear strength (ILSS) of the laminate material which was taken as 50 MPa. The analytical results showed good correlation with small thicknesses, but for higher thicknesses large scatter existed and the relation did not match with experimental results. Ambur & Starnes [9] studied the low velocity impact effect of thin - curved composite laminates. They investigated the required energy levels to induce barely visible damage within the thickness for a variety of geometries. The plate radius and thickness were found to be influential for the required impact energy and the compression after impact strength of the specimens was also found to be dependent on the plate radius.

Some researchers have investigated the ILSS of composites experimentally as a characterising material property for delamination. Shivakumar et al [10] used a modified short beam shear (MSBS) test to measure the ILSS of nine different

composite materials with different resin systems. Their test method could quantify the ILSS more accurately than the standard test methods which are: short beam shear (ASTM-D2344) [11] and double-notched shear (D3846-99) [12]. The modified test (MSBS) gave good correlation with failure modes and less scatter than standard tests. The limitation of both methods was that they can not be applied in the case of thin laminates.

El Awadly [13] studied the interlaminar shear response of laminated composite. His main objective was to study the effect of stacking sequence and thickness of layers on the ILSS of the E-Glass/Epoxy composite. He used a FEM and short beam shear test (SBST) described by ASTM D-2344-84. Using scanning electron microscope analysis, the failure was shown to occur through the resin or the resin-fibre interfaces and fibres did not fail. It was also shown that the perpendicularity of adjacent layers results in high possibility to stress concentration. This was due to the mismatch of engineering properties when these layers moved against each other.

1.1.2 Non destructive testing of fatigue damage

Many non destructive testing techniques were used to evaluate the fatigue damage of composites. Melin & Schon [14] studied delamination growth under fatigue after impact on ply level with C-Scan. They tested zero dominated and quasi-isotropic laminated specimens made of carbon prepreg. They were initially impacted with 27.6 J and then were subject to compression-compression fatigue with loading ratios, ($R = \sigma_{min}/\sigma_{max}$), R=-1 and R=-5. The load frequency was 0.5 Hz. Digital Speckle Photography (DSP) was employed to measure out of plane displacements. The ultrasonic C-Scan images showed that delamination created by impact followed the direction of fibres of the adjacent ply close to the non-impacted side of specimens. It was also found that most delamination growth took place through width, i.e., in a direction perpendicular to the load application and they were shown to happen during the compression cycle of loading.

Chen et al [15] introduced a real time technique to measure the damage growth for carbon specimens under compression-compression fatigue loading after being impacted by 10 J. The tests were performed at a loading ratio of R=10 and a frequency of 1 Hz. They developed a new system of measurements attached to

the loading machine. The system was able to measure delamination growth that exceeded the detector area. The measurements for the carbon laminate showed steady growth of delamination area perpendicular to load direction through the width. They noticed that the failure occurred when the damage propagated to the whole width and the samples exhibited buckling under compression load. They claimed the damage growth limit was taken at 10^6 cycles, however more fatigue specimens were needed to confirm such growth behaviour.

Chai et al [16] developed a technique to monitor the damage growth of impacted laminated plates under compression. The system consisted of high speed photography which was utilised to measure the damage propagation while a Moiré technique was employed to measure the out-of-plane deformation history of the specimens. Damage propagation was observed to take place across the specimen width and perpendicular to the load application line.

1.1.3 Compression after impact strength

A further research area for understanding the post impact behaviour was to predict the compression strength which is considered the most critical loading condition. In all the numerical and analytical models employed in the study of compression after impact strength of composite laminate, the damage size and depth information was quite essential. Idealised damage morphologies, such as through-width delaminations [17], circular [18] and elliptical delaminations [19], were utilised in many studies for the purpose of calibrating the proposed models.

Short et al [20] developed a numerical solution for the compression strength of initially delaminated specimens. They tested several specimens with different artificial delamination geometry and depth across the laminate. Two buckling modes, local buckling of the sub-laminate and a global buckling, were distinguished according to the depth of the sub-laminate. Such strategy was used as a calibration methodology for different models.

Chai et al [21] developed a one-dimensional mathematical model to predict delamination growth in compressed delaminated plates assuming the material to be isotropic, homogenous and linear elastic. The plate thickness was assumed to be much bigger than the sub-laminate which was situated near the surface. The delamination growth was concluded to occur in one dimension of the plate. The model for thin-film configurations could denote the stability condition of the growth.

As an extension for their 1-D model, [21], Chai & Babcock [22] developed a 2D delamination-buckling model to study parameters affecting the growth behaviour such as the initial delamination dimensions, the elastic properties of the cover layer, the Poisson's ratio of the parent medium, the loading history and the fracture energy. Out of the conducted experiments, they reported that the growth of damage in impacted laminates is unstable and occurring predominantly normal to the loading direction. From the derived model they concluded that the strain needed to initiate delamination growth increased with the increase in fracture energy, while it increased with the reduction in delamination radius and extensional modulus along the loading direction. Furthermore, it was observed that placing the fibres in the loading direction decreased the buckling strength and the growth initiation strain.

On the other hand, when the fibres were placed normal to the loading direction, the growth initiation strain and the buckling strength increased. This also resulted in delamination growth in a direction normal to the loading axis. The growth stability condition was noted to depend on the elastic properties of the top sub-layer, the Poisson's ratio of the parent substrate and the fracture energy. Another significant outcome was that the difference between buckling and propagation strain was decreased as the delamination radius decreased or the sub-layer thickness increased.

Flanagan [23] developed a closed form model to predict growth of two dimensional damage for laminates under compression. The model evaluated the post impact strength by calculating the strain energy release rate along the axes dimensions of an elliptical thin sub-laminate. Both models of Chai & Babcock [22] and Flanagan [23] calculated the strain energy release rate for two-dimensional growth around the boundary of a thin elliptical sub-laminate. Hence they included both Mode-I and Mode-II contributions, albeit without distinguishing between them.

Shan & Pelegri [24] introduced an analytical model to study the combined global buckling of a beam with a central buckled delamination under axial compression. Their model accounted for the force and moment components at the delamination tips during the local buckling of the sub-laminate and the global buckling of the specimen. They assumed that the delaminated beam was bent under axial compression and that delamination buckling occurred before global buckling. Three expressions of total strain energy were obtained in terms of applied force and geometric parameters for different loading states; before local buckling, between local and global buckling and following to global buckling. The obtained moment component was found to be inversely proportional to the thickness to depth ratio. Although the model did not predict the damage propagation, it could be used to study delaminated beams for different buckling scenarios.

A key difference between buckling analysis and post-buckling analysis is that the first is linear resulting in the load that forces the structure to change from one status to another. On the other hand, the post-buckling nonlinear analysis investigates how this new status changes with respect to the input load or stress. Laminate failure due to buckling of near surface delaminations was covered by many researchers, e.g., [25], [26].

Kardomateas [27] studied the buckling and post-buckling of delamination in layered plates under compression loading. He developed an analytical method to predict the out-of-plane deflection in terms of applied axial force assuming an isotropic linear elastic material. He used the Elastica theory introduced by Britvek [28] which is an analytical methodology for elastically constrained structural elements under compression. He assumed the initial post-buckling deformation to be small. Furthermore, he expanded this closed form expression in terms of Taylor series to obtain the end rotations and end moments at the delamination front. He then utilised the mode mixity criterion of Suo & Hutchinson [29] to obtain the Mode-I and Mode-II fracture toughness at the delamination front. He concluded that for the same applied strain, for a deeper delamination, the Mode-I component was higher than for a delamination near the surface. Another significant outcome was that the loading condition at the delamination front became pure Mode-II at high levels of applied strain.

Hunt et al [30] used a four degrees of freedom Rayleigh Ritz approach to analyse the buckling and post-buckling of a delaminated composite strut under axial compression. The model assumed the beam was isotropic and the undelaminated end laminates were ignored in the prediction of snap-buckling moment, while the delaminated parts were modelled with bending and in-plane stiffness. Further assumptions were that rotations of the undelaminated region and each delaminated part were the same at their intersection, and that there was no relative shearing movement between laminates at the interface. These rotations were one of the degrees of freedom. Furthermore, a second degree of freedom represented the end-shortening of the sub-laminates over the delaminated region. A further degree of freedom was used to describe the buckling displacement of the delaminated parts. The model results showed good agreement with FEA results for the studied configurations. An interesting outcome was that the model captured the snap-buckling and the subsequent bifurcation modes for the tested configuration.

Wright [31] extended the model developed by Hunt et al [30] to analyse the buckling and post-buckling of a delaminated composite strut under axial compression. The model investigated nonlinear buckling behaviour of delaminated layers within a laminate under end compression. She used the four-degree of freedom nonlinear Rayleigh-Ritz formulation as in [30] which comprised two end undelaminated regions and a delaminated region of length. The model studied the effects of changes in delamination depths and introduced a parameter governing the relative stiffnesses of the layers. The end laminates were given both bending (EI) stiffness while the delaminated parts were modelled with bending and in-plane stiffness (EA). The assumptions for the model were: 1- Rotations of the undelaminated region and each laminate were the same. This was enforced by setting a parameter representing the end rotation. 2- There was no relative shearing movement between laminates at the interface which resulted in a second degree of freedom representing the total end-shortening over the delaminated region. Two further degrees of freedom were used to describe the sub-laminate buckling displacement and the side rotation at the delamination end. The latter degrees of freedom also included the position of the neutral axis relative to that of the centre line in the case where different materials were used for the delaminated layers and the base part.

The total stretching and bending energy terms for the system included all the nonlinearities governing post-buckling effects. The solution of the system of equations gave an explanation for the switching between closing to opening for thin sub-laminates. Such outcome is substantial in studying post-buckling behaviour.

A recent analytical low dimensional methodology to predict propagation strain for two dimensional single delamination was developed by Rhead & Butler [32]. They assumed that the propagation occurred as a consequence of delamination buckling. The main concept of their derivation was to obtain the difference in strain energy at the post-buckled state before and after delamination propagation. The difference in energy was compared to the Mode-I fracture energy for a unit length. They approximated the damage to be of a clamped circular sub-laminate that existed at a single interface through the thickness. A further assumption, based on previous study [33] on impacted quasi-isotropic laminates, was that the delamination diameter decreased linearly through 20% of the thickness near the back face. The interface with the minimum calculated propagation strain identified the weakest interface. The model was verified against experimental results and showed good correlation.

A similar modelling strategy by Rhead et al [34] was established to predict failure strain of free edge delaminations. In order to do that, they approximated the delamination to be of a semi-elliptical shape to resemble the morphology visualised by C-scan images. The boundary conditions were assumed to be clamped at the curved circumference and free at the flat edge. The VICONOPT software [35], which is a general buckling software for buckling analysis using finite strip method, was employed to model the damage delamination. The semi-elliptic shape of the damage was approximated as six connected equal-width finite strips with 12 constrained nodes at their junction. The calculated buckling strain for the assumed geometry was then incorporated to predict the threshold strain using the same formula presented in [32]. The predicted strain values were verified experimentally on a variety of composite stiffeners and showed good agreement.

Fatigue of impacted composite structures was covered by a great deal of researchers to verify the fatigue strength experimentally [36]. Some researchers have proposed empirical models to predict fatigue limits [37], [38]. Types of fatigue loading were also studied by Jones et al [39] which showed that compression-compression loading is more critical than tension-tension loading.

Katerelos et al [40] developed a semi-analytical model to predict the angle at which an impact damage propagate in quasi-isotropic composite laminates under compression-compression fatigue. For this purpose, they calculated the strain energy release rate (SERR) around the damage boundaries predicted by C-scan technique which was approximated as an ellipse. The SERR was obtained for each interface in terms of the applied strain and the difference in sub-laminate and the total laminate moduli. The series of the acquired (SERR) polar distribution indicated the growth direction and weakest interface at which propagation occurred.

Freitas & Carvalho [41] studied the residual strength for damaged carbon fibre laminates under compressive fatigue. The laminates initially had a drilled hole prior to their fatigue testing. Their work aimed to establish a relation between the delaminated area growth from the central hole and the corresponding fatigue life and the residual static strength of the laminate. The tested specimens were manufactured from Hexcel 913-HTA prepreg. Compression fatigue tests were performed on three different quasi-isotropic laminates using an anti buckling fixture with a window of 140x80 mm to allow out-of-plane deflection of the delaminated area. All tests were performed under load control and a frequency of 5 Hz. The specimens were then inspected by an ultrasonic C-scan machine at specific number of cycles. Through the fatigue cycles, the damage was observed to grow laterally constructing an elliptic shape with its major axis kept pointing laterally. As the delaminated area growth to a critical level, buckling occurred and overall collapse of the specimen was observed. They established an empirical formula relating the damage area grew rate per cycle, (dA/dN) in terms of the maximum amplitude for the strain energy release rate of the loading cycle. Furthermore, the obtained equation was then incorporated to obtain the residual strength of the laminate.

Butler et al [42] developed an analytical model to predict the fatigue strain limit of impacted composite laminates with opened delaminations. They defined the strain limit as the strain below which no damage propagation occurred under fatigue loading. They also adopted the assumption that the BVID morphology remains within its initial size until the final stages of the fatigue loading at which the sub-laminate buckles and then propagate. The model assumed a constant thin film delamination existed at a significant depth and constructed from a six adjoined finite strips. The boundaries of these strips were bounded by a circle

encompassing the whole damage and that the thin film was buckled. The total strain energy of the system was evaluated in terms of bending and axial strain energies. The strain energy release rate (SERR) was calculated in terms of applied strain, buckling strain and axial and bending stiffnesses of the laminate, A_{11} and D_{11}. As the thin film was assumed to buckle and then propagate in the load direction, the strain energy was equal to the Mode-I fracture toughness, G_I. The model was verified by experimental results for different sets of laminates. The samples were tested under cyclic compression loading using a loading ratio (R=10). An in-situ acoustography technique was employed to monitor the damage propagation during the loading application. The tests were stopped at a specific number of cycles to section the samples and determine the depth of delamination growth at different ply interfaces. They concluded that when the loading level was above the predicted fatigue level, propagation occurred and growth extended rapidly. A fatigue threshold strain established for the tested laminate was assumed to correspond to 10^6 cycles.

The aforementioned model [42] was further enhanced by Rhead et al [43]. They assumed that the buckling of multiple delaminations caused by impact could be modelled as a buckled circular sub-laminate with a single delamination at a critical depth fixed around its boundary. One significant difference in this model was that the stored bending energy was equivalent to the stretching (in-plane) energy released and the energy released in the lateral direction was small, i.e. the total strain energy release was only obtained in terms of axial stiffness, A_{11}, rather than A_{11} and D_{11} in the aforementioned model [42]. The enhanced model gave close prediction of propagation strain values for four different laminate configurations tested in earlier research works [44], [14], [15].

1.1.4 Sandwich structures

Sandwich composites are used extensively in many automotive, aerospace and marine industries due to their ability to produce structures with high stiffness-to-weight ratios. Under general loading conditions, the sandwich faces resist the compressible forces while the core increases the flexure rigidity which is a characterising aspect of sandwich structures. Due to the increase of their application, there is a growing need to certify these types of composites under controlled tests. Sandwich structures are often prone to impact in real environment, the influence

of impact damage on static and fatigue strength has been extensively studied. Many researches have investigated the damage mechanism of sandwich structures. Damage in sandwich structures may take many forms, face-core debonding, fibre breakage, face delamination and core crushing or core shear.

Rome et al [45] studied the compressive strength of impacted sandwich panels experimentally. Out of his experiments, he indicated that the compression strength after impact is 40% of the undamaged specimens. He then introduced a methodology to predict the compression after impact strength using a combined computational FE progressive failure methodology.

Kassapoglou [46] used an eigenvalue buckling analysis to evaluate the buckling and propagation of artificial delamination placed in sandwich faces. First, they tested sandwich specimens with three different layups used for the faces. An imbedded Teflon piece (0.002 in thick) was inserted in one of the faces to represent an elliptical delamination. The size of the delamination was changed for a series of specimens. In order to avoid crushing of the core under gripping, an aluminium peace was inserted between the faces at both ends and two aluminium tabs were used on both sides of the specimen. They identified the buckling load for the delaminated faces from the load-strain behaviour for those specimens. They finally introduced an expression to predict compressive buckling strength for the tested sandwich configuration.

Kassapoglou & Abbott [47] studied the compression after impact of sandwich specimens with delaminated faces. They used graphite epoxy faces (AS4/E7K8) with Nomex honeycomb core (Hexagonal 3 lb/ft^3). The core thickness was 1.0 inch and the two faces were identical for each panel. The specimen were impacted by different energy levels, ranging from 4.6 to 12 J. Elliptical damage morphology appeared in the post impact scans suggested that the semi analytical model developed earlier, [46] could be incorporated to predict the compression strength for the tested configuration. The prediction showed reasonable agreement with experimental results.

Ambur & Cruz [48] presented a model to predict low-speed impact response of sandwich panels with different face thicknesses, core thicknesses and different core densities. They modelled the impact face as a plate on elastic foundation to determine the contact force and surface strains. The force formula was used

to determine the out-of-plane displacement for the rest of the panel which was modelled as a homogenous plate. They reported that the damage-initiation energy levels for the tested sandwich panels were much lower than those for the face sheets. The threshold impact energy level was identified when the certain failure modes occurred, such as through-thickness shear, delaminations, the back surface of the face tension failure, core separation or crushing. They studied several face-core configurations against the threshold energy to induce damage. The faces for all tested specimens were made of Hercules IM7 graphite fibre prepreg with Narmco 5260 bismaleimide resin and made of 26, 32 and 52 plies. The face layups were $[(45/0/-45/90/0)_2/90]_s$, $[(45/0/-45/90/0)_3/90]_s$ and $[(45/0/-45/90/0)_5/90]_s$. In all specimens, the energy level causing apparent damage was 13.6 J except for the specimen with 52-layer face. The shear failure pattern and the ensuing delaminations between the -45 and 90 plies were clearly developed for $[(45/0/-45/90/0)_2/90]_s$ and $[(45/0/-45/90/0)_3/90]_s$ face laminates. They concluded that the impact energy for damage initiation in sandwich panels was much lower than that for the plates with the same properties as the face sheets and that was due to the local nature of the impact response for sandwich panels where the shear deformation is more dominant than the bending deformation. Their results showed that the impact response of sandwich panels was very local and not dependant of either the boundary conditions or the plate size. They also concluded that the failure mechanisms in sandwich panels were dominated by shear failures and delaminations regardless of their thickness value.

Many studies have investigated the post impact behaviour of sandwich structures, e.g. [49] and [50]. Czabaj et al [51] studied the compression after impact strength, CAI, for different sandwich configurations. The tested specimens were manufactured from different density aluminium honeycomb cores with faces made from different quasi-isotropic laminates. In order to induce damage in the sandwich faces and the core, rather than using impact, two spherical indentors with different diameters, 25.4 mm and 76.4 mm were used to apply quasi-static loading on the specimens. Four face arrangements were made of eight plies of IM7/8552 unidirectional carbon prepreg: $[45/0/-45/90]_S$; $[45/-45/0/90]_s$; $[-45/45/90/0]_s$; $[45/90/-45/0]_s$. Specimens were cut and then potted in resin to strengthen their ends during the compression. In addition, they were supported against any lateral movement by inserting them between two steel platens attached to the machine jaws. Furthermore, a spherical seat was used to evenly transfer the axial load into the specimen. The shadow Moiré technique was implemented to

monitor the surface damage progression during the test. The CAI strength was normalised with the corresponding strength for the undamaged specimens. The Moiré fringes suggested that the damage growth in compression tests was a result of the increase in the initial dent depth. Although most specimens exhibited delamination buckling that led to final failure, the first and fourth laminate types were more delamination resistant as they possessed smaller areas of delamination projected by the Moiré fringes. The first laminate had a bigger size delamination buckling pattern as the [0] layer was closer to the outer surface which increased the stiffness of the thin sub-laminate compared to the rest of laminates where it existed on a deeper level. Such high stiffness in the sub-laminate of the first laminate drew more load compared to other laminates which increased the likelihood for delamination buckling and hence failure. It was also concluded that specimens indented by the bigger size indentor had more residual compression strength compared with those indented by the smaller one.

Fleck & Sridhar [52] studied sandwich column behaviour under axial compression. Their main objective was to study the compressive strength in terms of column length and core density. The faces were made of four layers of 7781 E-Glass woven pre-impregnated by 914G epoxy resin and the core was made of closed cell PVC polymer foam. Three different density foams were used to manufacture three sets of specimens which were tested under compression using the ASTM C364-61 test method. In order to ensure a fixed-fixed condition, the specimens were inserted into a U-shape steel containers using an epoxy adhesive. Tests were performed under displacement control and failure strength was obtained in terms of specimen unsupported length. The observed failure modes were overall buckling, face micro-buckling and local face wrinkling. Finally, failure mode maps were established as a design and characterisation strategy for the studied sandwich types. For the tested specimens, face wrinkling was less likely to occur as the micro-buckling strength or the buckling strength were higher than wrinkling strength.

The fatigue failure of sandwich cores was considered by many researchers to be critical under shear loading. Kulkarni et al [53] investigated the fatigue of sandwich panels tested by a three point bending fixture at 3 Hz and a stress ratio of $R = 0.1$. The crack initiation was near the compression surface below the top face/sheet core interface. It then moved parallel to the beam axis from point of initiation to the end support. Three events of damage propagation were recorded

before failure. First, the crack moves along beam length at a small distance under the face/core interface. This process took 85% of fatigue life. The crack then turned across the core due to shear (second step) until it reached the bottom face sheet/core interface. Quick propagation of the crack occurred and which resulted in a delamination in the core/face interface. It occupied about 7-8% of fatigue life and ended at the support. The stiffness degradation during fatigue cycles was monitored to occur rapidly once the core shear began. The authors introduced a semi-empirical model to predict the fatigue life as a function of crack length and stress level. The fatigue limit for the specimens was found to be 60% of the ultimate strength.

Burman & Zenkert [54] used four point bending tests to characterise the fatigue behaviour of two foam core materials; Divineycell H100 and Rohacell WF51. One face material was made of DBL-850 Fabric and Vinyl-ester 8084. The other face material was epoxy impregnated quasi-isotropic glass fibre [0/45/90/-45] prepreg. The advantage of four point bending is that no large stress concentration was present. They used a fixture that allowed for both tension and compression cycles. Static tests were initially performed to get relevant load levels for fatigue tests and mode of failure at different load ratios. A digital thermometer was then used to monitor the temperature of the core. It was shown that stress amplitude had greater influence on fatigue life time than mean stress. The tests showed small variation in stiffness during the majority of the recorded life time.

Zenkert & Burman [55] studied the fatigue of sandwich structures with three foam types under tension, compression and shear fatigue. The foam materials were Rohacell WF51, WF110 and WF200. They used faces of glass fibre sheets in shear fatigue testing. The shear fatigue was performed under four point bending. The tension fatigue strength for the WF51 foam was higher than those of compression and shear. For higher density foams WF110 and WF200, the compression fatigue strength was higher than tension and shear. The acquired S-N curves for the different density foams showed that the shear fatigue strength was the lowest with similar slope as recorded in the compression case. They also noted that face buckling was the most probable cause for triggering failure mechanism in compression for the low density foam.

To better understand the compression fatigue strength of sandwich composites, the compression after impact behaviour was of interest to many researchers. Free-

man et al [56] tested sandwich specimens of carbon faces with foam filled honeycomb core after impact with 10, 20, and 30 J. Two sets of specimens with two and four layers in each face were tested under four point bending fatigue. The foam density for the four layer specimens was 106 kg/cm^3 and for the two layer specimens, 164 kg/m^3 and 106 kg/m^3 foam materials were used. The tests were conducted at 90%, 80%, 70%, and 60% of the ultimate strength while using an R = 0.165(=$\sigma_{min}/\sigma_{max}$) and a frequency of 1 Hz. They failed in the shear region, i.e. between the outer support points. The crack initiated at the interface between the top face sheet and the core, then it propagated through the sample for most of its fatigue life. The crack was visualised to turn through the core until it reached the opposite face-core interface then propagated along the face-core bond until failure. Specimens with two layer faces and two different densities were tested and showed little effect of impact on fatigue life.

Shipsha et al [57] addressed the effect of low velocity impact damage on post-impact failure mechanisms of foam core sandwich beams with faces of FRP subjected to edgewise compression and bending load cases. The core material was rigid PMI foam Rohacell WF51 with density of 52 kg/m^3 and a thickness of 50 mm. The faces lay-up was $[0, 90, \pm 45]_{2s}$ with a thickness of 2.4 mm made of E-glass weave. The specimens were impacted by a steel cylinder across the whole width of the specimen using energy levels of 6.6, 13.3, 20, 26.5 and 52J. After impact, no residual indentation on the laminate surface was recorded, other than whitening spots observed on the surface after 26.5 and 40J impact level. The sandwich core was crushed with an open cavity between the face and the core. Next, the specimens were tested under static compression and four points bending to measure the critical buckling stresses of the delamination faces. They verified that the residual buckling stresses were 15% and 23% of the corresponding undamaged ones under edge compression and bending respectively. Furthermore, there was no significant difference between buckling stresses under compression and four point bending at the same impact level. They finally noted that low-velocity impact can cause serious damage in the core and face-core interface without any significant damage in the laminate faces.

Kardomateas & Huang [58] introduced a general nonlinear beam model for the prediction of buckling and post buckling behaviour of a delamination within sandwich beams under compression loading. The model allowed for large deformations and assumed both the faces and the foam materials were homogenous.

A further assumption was that the delamination existed within the faces or at the face/foam core interface. The formulation included the transverse shear for the delaminated and the substrate parts which was found to decrease the critical buckling strain for the delaminated single layer. The model could describe different sandwich configurations including different face laminates.

1.1.5 Bending of solid laminates

Although many researchers have studied buckling driven delamination under compressive loading, so far, there has been little discussion about buckling driven delamination under bending loading.

Kardomateas [59] studied the possibility of snap-buckling for delaminated composites under pure bending as an extension of previous work studying the snap-buckling phenomenon using energy methods. The model assumed an orthotropic beam-plate subjected to pure bending moment which has an interlayer crack positioned a depth near to the compression side and it is situated at the middle of its length. It also included the geometry nonlinearities and the change of force along the upper delaminated layer from compression to tension at its inflection points. He used similar expressions for end forces and moments as described in Britvek [28]. The critical moment was derived by solving a system of three non-linear equations: force equilibrium, compatibility conditions of deflection for delaminated layers and finally the difference between total strain energy and initial energy. He conducted a series of experiments to verify the developed model. Three specimens were made of 15 plies of unidirectional Kevlar-49 prepreg. Each specimen had a Teflon strip placed at one depth at the 1st, 3^{rd} and 4^{th} ply. Four-point bending tests were performed on those specimens and strain measurements were obtained from gauges placed on the middle of the delaminated layer so that the point of snap buckling can be determined from the sign change of the strain. The results showed 50% difference from the model at the first ply delamination depth and 6-11% difference for the 3^{rd} and 4^{th} ply depth. This showed the model was not able to predict the critical moment correctly for a delamination situated at a small depth.

Dransfield et al [60] tested HTA/6376 carbon laminates under bending and compression after being impacted by 35 J. Two thick laminates were tested 4 and 8

mm. The C-Scan images taken after impact of showed that in the 4 mm specimens, the scatter in size of the damage was small compared to that in the 8 mm specimens. In the 4 mm specimens, the damage was distributed through the whole thickness. On the other hand, in the 8 mm specimens, the damage was only confined within the upper third of the whole thickness. The specimens were then tested under bending and edge compression up to failure. Some specimens were tested while the impacted side was under compression and others were tested while the impacted side was under tension, i.e. the largest delamination was under compression. In the 4 mm specimens, 10% reduction of failure load was observed when the impact side was under tension and the failure was delamination buckling behaviour. For the 8 mm thick specimens, 15% reduction in failure load was observed when the impact side was under compression. The far field strain for the 8 mm specimens was shown to be 40% higher than the 4 mm specimens when the impacted side was under tension. They also showed that the far field strain for the specimens under bending was higher compared to in-plane compression. Failure strain under compression was recorded at 45% and 19% lower than the failure strain of the specimens under bending when the impacted surface was in tension and compression respectively.

Wang et al [61] studied the snap-buckling of an inner delamination in an initially curved beam under a closing bending moment. Their model was based on a non linear analysis for large arch deflections. They assumed that the snap-buckling would occur near to the inner surface when high interlaminar stresses were induced due to an applied bending moment. The general model required the solution of a system of five equations including five variables which was transformed into a simpler form using more assumptions, which were: the delaminated layer was near the surface; stress within the thin sub-laminate was uniform and that global beam curvature before and after the delamination was constant. It was possible to provide a solution for the simplified system using theses assumptions which reduced the use of complicated elliptic integrals. By equating the strain energy of the system with the fracture energy, the resulting fracture moment was obtained in terms of critical fracture energy (based on Griffith fracture criteria), thicknesses of sub-laminate and substrate, initial curvature of the beam, longitudinal modulus of the beam. The obtained moment was inversely proportional to the initial radius of curvature of the beam, i.e. bending of short curved beam might incur snap-buckling and consequently delamination near inner surface at small bending moment.

Lu et al [62], introduced a numerical solution for the prediction of delamination propagation in beams made of orthotropic materials. The mode ratio (Mode-I/Mode-II) was sought in two different problems: straight cantilever delaminated beam under tip shear force and an initially curved delaminated beam under opening bending moment. In order to reduce the number of material parameters in the model, two new parameters were introduced. One parameter characterised the longitudinal-transverse moduli ratio while the second was an orthotropy parameter relating the three moduli and Poisson's ratios for the material which was equal to unity in case of an isotropic material. The strain energy release rate $(G_I + G_{II})$ was obtained in terms of the aforementioned parameters. For the case of cantilever beam, it was shown that $(G_I + G_{II})$ increased by increasing the orthotropy factor. For curved beams with a delamination near the surface, i.e. small thickness to depth ratio, it was found that when the delamination length increases, Mode-II energy component increases relatively faster than Mode-I component until it reached a peak value at a certain angle for each thickness/depth ratio. The total amount of energy release increased proportionally with the mentioned ratio until the delamination reaches a length where it did not increase any more. For small thickness/depth ratio, pure Mode-II occurred at delamination fronts as it propagated or for delaminations with large lengths. For a delamination near the inner surface (tension surface), small cracks exhibited negative Mode-II release rate until an arc angle of 20^o and a thickness/depth ratio of 1/3, it became positive.

A considerable amount of literature has been introduced to characterise mixed mode failure for different composites, i.e. provide a value for critical toughness value G_C according to mode mixity ratio G_I/G_{II}. O'Brien [63] established a programme within NASA to characterise composites with different damage and crack configurations. Methodologies produced by the programme would be included in the new Mil-17 military handbook. The methodologies include the calculation of fracture toughness for different damage scenarios and a life prediction tool for each case.

Davidson & Zhao [64] studied the dependence of the critical toughness value, G_C, on mode mixity. In order to do that, the energy release rate was graphically acquired by plotting fracture locus diagram for a set of standard fracture toughness tests. The availability of mixed-mode failure curves could be possible through performing different testing for the material in question, such as, DCB to obtain G_{IC}, ENF for G_{IIC} and MMB to acquire the fracture value at different mode mixity ratio. Such method was time consuming and including laborious testing work. With this in mind, they proposed a model to predict failure criterion for continuous fibre epoxy composite laminates under different mixed-mode conditions. The model was to offer an expression for toughness versus mode mixity and was verified using extensive test data from previous literature, like cantilever beam, end notched flexure and single leg bending tests. The model provided a bi-linear expression with a break point at $G_{II}/G = 0.4$ and incorporating G_{IC} and G_{IIC}. Finally the model was used to fit the experimental data using a limited input Bi-linear criterion.

Matsubara et al [65] examined the behaviour of unidirectional and fabric composites under Mode-II fatigue testing using ENF test configuration. The tests were run at different stress ratios for tension-tension, tension compression and compression-compression load schemes. Out of these experiment and after examining the fracture surface, they found that in unidirectional carbon, the crack growth was dominated by Mode-II. Another outcome was that by changing the stress ratio did not change the threshold value of Mode-II. In the unidirectional type, they found the threshold was about 0.16 of its static value, while in the mixture of unidirectional and fabric, the threshold was higher.

Williams [66] introduced strain energy release expressions for cracked strips under different loading configurations. His solution included calculating the release rate for uniform notched delaminated specimens under peeling force and moments. He then extended the derived expressions to account for plastic deformations in some loading cases. For this purpose, he used a simple beam analysis to account for strain energy release rate, by first calculating the strain energy at the delaminated or notched edge. The release rate was obtained by differentiating it with respect with crack or notch length.

Kim et al [67] developed a model to predict delamination buckling and subsequent growth of thin fibre layer in a laminated wooden long beam under bending. The model was derived for a four-point bending apparatus and did not include mode mixity factor in the calculations. Furthermore, they assumed a Cosine function for the post buckling shape of the sub-laminate and the moment component on the sub-laminate edge was discarded. They concluded that the critical buckling load and moment were within 2% of experimental results. The stability of delamination growth in experiments were compared to analysis by incorporating G_{IC} of the sub-laminate into the model.

Asp et al [68] investigated the delamination growth under Mode-I and Mode-II loading in fatigue of a carbon composite material. For Mode-II, the threshold value was 10%; while for MMB (mixed mode) was 15% and 23% for Mode-I (DCB). The different modes showed different fracture patterns when looked upon using the electro scnanning microscop techniques, ESM. In the DCB specimens, Mode-I fracture occurred in the resin rich areas. While in ENF, Mode-II, shear cusps were observed in the ESM images.

Rothschilds et al [69] studied thin film delamination under compression and suggested that the delamination geometry was not symmetric about the delamination front. Hence the opening moment for the top delaminated layer gave rise to interlaminar shear stresses at the delamination front. Both actions significantly increased Mode-II component more than Mode-I.

Shan & Pelegri [70] introduced an analytical and a FE numerical model to study the fracture behaviour of a cross-ply composite cantilever beam with an artificially embedded delamination, also incorporating the friction and contact. The model incorporated the effect of loading asymmetry in the delamination contact zones using finite elements. They investigated the contact zone formation during the local buckling of a delaminated beam under bending and its consequences on propagation of this delamination. Deflection and rotation of the undelaminated parts of the beam were presented in terms of applied tip force and beam geometry at different sects of the beam assuming simple beam deformation theory. After verifying the analytical results for deflection with experiments, the total energy release rate of the system was derived as a superposition of the force and moment components acting at the delamination end. Experiments were performed on cantilever beams with different thickness to depth ratios. The characterising load-

displacement plot had a change in slope upon delamination occurrence and a drop in load at propagation. They also modelled the effect of loading asymmetry in the delamination contact zones by finite elements. Incorporating the contact zone effect in the finite element analysis enabled them to compute the Mode-I, Mode-II and the intensity ratio, (K_{II}/K_I), at both delamination ends for the different studied beams. From the FEA results, it was concluded that this ratio was equal to 20 at the delamination end near the tip and 50 at the inner delamination end. For a tested beam deeper delamination the mixity ratio at outer end (near tip) was 1.5 and 30 at the inner one. These results suggested that the fracture at the inner tip was dominated by Mode-II fracture. At the outer tip, a mixed mode fracture was denoted, i.e. it depended on curvature of the beam; when increased, the contact zone increased in length and consequently the Mode-II component. The ratio at either tips increased as the thickness to depth ratio decreased. They also concluded that the failure behaviour was dominated by Mode-II effects due to the large contact zone which was characterised by geometry and loading parameters and that the deeper the delamination, the weaker the structure becomes with respect to propagation.

Tanaka & Tanaka [71] concluded that fixed stress ratio of fatigue testing of Mode-II delaminations in ENF tests caused fixed crack propagation rate. Changing stress ratio from tension-tension to tension-compression reduced the threshold G_{II} toughness value. Their fatigue threshold value was recorded at $10e^{-9}$ m/cycle.

Wang & Shenoi [72] developed an analytical model to study the delamination propagation for a curved composite beam with a delamination placed near the outer surface under an opening moment. They assumed the curved delamination and main beam to be linearly elastic, homogenous and orthotropic before and after delamination. They implemented a linear beam analysis to model the problem using polar coordinates. The displacement equations of the beam along with compatibility conditions comprised seven equations with seven unknowns. The solution of these equations gave the displacements of the base beam, delaminated layer and the corresponding applied moments at their delamination fronts. The strain energy in each beam was consequently acquired and differentiated with respect to initial crack length to obtain the release rate. By equating the final equation with the critical release rate of the material, the critical moment for propagation was obtained in terms of crack angle and fracture toughness of the

material. For a centred symmetric delamination, they concluded that the initial beam curvature and the arc angle of the delamination have significant effect on propagation of the curved beam.

A research was performed by Williams [73] to predict the delamination propagation in a cracked beam. His motivation was to introduce a simple analytical method rather than complicated numerical techniques. He started with linear beam assumptions to calculate rotations at delamination edges, through which he obtained the bending moment components at these edges. Finally he derived an expression calculating SERR in terms of moment components acting at both sides of delamination front. After using one component representing the strain energy release rate, he introduced a more detailed methodology to obtain Mode-I and Mode-II SERR at the delaminated edges. The analysis was then applied on different configurations to provide expressions for Mode-I and Mode-II SERR terms under constant load and displacement. He then derived formulae for delamination of struts including both Mode-I and Mode-II SERR, G_I and G_{II}, respectively. He concluded that for a delaminated beam under compression, G_{II} would dominate over G_I when the ratio (P/P_C) equals to five, where P_C was the buckling load for the thin sub-laminate.

The sublayer delamination problem has been covered in the analysis of micro electro mechanical systems (MEMS). On those small-scale structures, any excessive stress build-up can cause delamination buckling failure or peeling of the insulating film covering the sub material.

Kosel et al [74] presented a mathematical model predicting the level of axial force for delamination of the top layer of a two-layer plate. Their model included the elasto-plastic effect between the bonded layers and was solved numerically and verified by experimental testing. Fang & Wickert [75] studied the post buckling behaviour of micro-machined beams under in-plane compressive loading. Their nonlinear model related out-of-plane deformation to compressive stress and included initial imperfection. The initial imperfection was included in the displacement and energy equations. Such imperfection explained the smooth growth of the resulting buckled delamination from the pre-buckled status to the post-buckled one. The imperfection displacement was expressed as a linear expression of the initial beam length. The solution for the system included three different roots, where the imaginary were ignored. The positive real roots of the system

represented possible state of the post-buckled system, while the negative roots represent impossible state where the thin delaminated beam passes through the main sub material.

Wang & Qiao [76] studied the split of shear deformable bi-material beams by obtaining the force and moment components at the delamination front, which addressed the extraction of fracture modes; Mode-I and Mode-II. Compared to Suo & Hutchinson [77], they modelled the cracked tip while implementing shear forces at delamination edges. They modelled the two delaminated edges using Reissner-Mindlin first order deformation plate theory to include the transverse shear force at the tips. The strain energy release rate for Mode-I and Mode-II could were then obtained in terms of the edge force and moment components. They concluded that their model was reduced to that of Suo & Hutchinson [77] (classical plate theory based model) when ignoring such shear force at the edges.

Bolotin & Nefedov [78] studied propagation of delaminations in thick composite beams under bending fatigue. The delamination thickness was assumed to be small compared with the total thickness. The main beam was subjected to uniform bending, assuming displacement control of load application. Whilst assuming the ends of the delamination were clamped, the displacement of the delamination was expressed as a superposition of beam curvature and a cosine function representing out-of-plane amplitude. By equalising the end shortening of the delamination to resulted strain from loading, critical strain for buckling was obtained. Post-buckling out-of-plane displacement was finally derived in terms of axial strain in the delamination and beam geometry. By ignoring the imaginary roots of the aforementioned equation, the real roots were representing possible the out-of-displacement values of the sub-laminate. The analysis was essential to further understand the stability of buckled delaminations. It was possible to calculate the total strain energy in the delamination buckled configuration of the beam, expressed in two parts: axial strain energy and bending strain energy. The strain energy release rate of the system was obtained by differentiating the energy equation with respect to crack length. The release rate increased as crack length increased until reaching a peak and then becomes to a flat plateau. The applied strain is proportionally resulting in increasing the total release rate of the system. Equalising this total release rate expression to a critical fracture toughness value of the material may lead to only one delamination propagation at small fracture toughness levels or two propagation possibilities at higher levels.

Murphy & Nichols [79] developed a low-dimensional model to predict the critical moment at which buckling of a thin sub-laminate delamination within a cantilever beam under static bending. They employed a similar nonlinear technique used for delaminated struts under axial compression developed by Hunt et al [30]. The model covered the case of delamination buckling in thin composite cantilevered beams subjected to a transverse end force. The beam was modelled as two different regions: the delaminated region was presented as geometrically nonlinear elastic Euler-Bernoulli beam and the rest of the beam as a linear elastic Euler-Bernoulli Beam. The equilibrium of the system was obtained by minimising the difference between the total strain energy and the external work. Due to the buckling occurred in the delaminated region, axial stretching of the neutral axes was considered which gave the nonlinear expression in the model. In order to verify the developed model, an experiment was conducted to measure the strain over the delaminated region of a cantilevered beam. The beam was made of 16 plies of carbon fibre cross ply laminates. The 20 mm long delamination was placed at the second ply depth and spanned the entire width of the beam which was then loaded by a screw-controlled micrometer at the free end to evaluate both forces and displacements. It was shown that by increasing the load, the strain measured on the top surface of delamination decreased until a certain value of load where it suddenly changed its sign. The model showed close behaviour to what recorded in experiments prior to buckling. However, the post buckling values were lower than those of the experiment i.e. the model was stiffer than the experiment. The difference also might be greater than discussed as the applied force direction was not perpendicular to the neutral axis of the beam throughout the loading application.

Yin [80] studied cylindrical post buckling of laminated structures under axial compression. They derived a one dimensional model including the bending-stretching coupling stiffness elements (B_{16}, B_{66}) that affecting the cylindrical buckling of the laminate. The inclusion of such elements reduces the overall value of bending stiffness. Using plate theory, membrane strains were obtained in terms of force and moment components and the combined bending-stretching stiffness matrix of the laminate. Such decrease in bending stiffness reduced the buckling strain for the sub-laminate that was derived by many researchers assuming homogenous material. Moment and force components obtained at the delamination edges allowed the calculation of strain energy release rate at these delamination fronts.

The bending of delaminated laminates stimulated the investigation of Mode-II toughness component. Warrior et al [81] developed a numerical model to predict pure Mode-I, Mode-II and mixed mode delamination. They used explicit FE code that included failure and post failure damage law. The code was verified against a variety of mode mixity tested specimens and showed good correlation.

1.2 Thesis objectives and overview

Amongst the different failures of composite structures, the buckling-driven delamination is considered one of the most critical. Hence prediction of such failure is of substantial importance. Although many models currently exist, there is a growing need in many industries, such as aerospace, to have the ability of accurately predicting such failure modes in early design stages. The required tools utilised in the preliminary design should be quick and accurate. While the numerical tools, such as FEA, are time consuming and usually being applied in late detail design phases, analytical tools are highly demanded in the early design and analysis of complicated structures.

The objective of this work was to analyse buckling-driven delaminations on two types of composite structures under static and fatigue loading. The first part of the thesis was to investigate the delamination behaviour of impacted sandwich structures with composite faces under compression. Two pre-developed low dimensional analytical models, [32] and [43], were employed and experimentally verified to check for their applicability for similar static and fatigue loading cases in industry.

The second part was to explore the buckling of delaminations under bending for through-width delaminated composite struts. The main objective in this part was to predict the buckling, post-buckling and final propagation of such delaminations under bending. These behaviours were modelled and predicted using a combined analytical strategy. Initially a non-linear pre-developed model was used, [30] was introduced to examine the kinematics of the delaminated struts. A linear fracture mechanics technique, [77], was then incorporated in order to predict the propagation failure of the delamination. A series of fatigue experiments were carried out on similar laminates based on the conclusions acquired from the static testing.

The third part was to experimentally examine the buckling of delaminations in impacted plates under both static and fatigue loading. The degradation effect of such real delaminations was compared to similar laminates with similar-size circular imbedded delaminations. The latter case can be used as a calibration data for future analytical and numerical models.

Chapter 2

Face Damage Growth Of Sandwich Composites Under Compressive Loading

2.1 Summary and objective

The current chapter includes a study of compression after impact (CAI) strength of sandwich specimens with laminated faces under static and fatigue compression in two perpendicular directions. The face laminates in these directions, defined as $[(\pm 45_C)_2, (0_C, 0_G)_4, (\pm 45_C)_2]$ and $[(\mp 45_C)_2, (90_C, 90_G)_4, (\mp 45_C)_2]$, are typical of those used in helicopter rotor blades. The subscripts C and G denote carbon and glass, respectively.

The post-buckling behaviour of the delaminations was explored by pre-developed analytical models to predict failure strains for the tested specimens under static and fatigue loading. The models calculated the critical strain energy release rate (SERR) for delamination growth of an axially-loaded laminate containing a thin, post-buckled sub-laminate, and related this to the critical Mode-I energy (G_{IC}) for the material. The models were based on the assumption that the propagation strain could be calculated in terms of the buckling strain of the thin sub-laminate produced by the impact damage.

A preliminary experimental study was carried out to first establish a suitable specimen configuration and test setups for the subsequent static and fatigue experiments.

Different non-destructive techniques were utilised to investigate the damage morphology that was involved in both analytical models. A Digital Image Correlation system (DIC) was used to monitor the impact-damaged face behaviour under compressive loading and results were compared with existing analytical models for prediction of CAI strength of composite laminates. The main test programme was then performed and the results were compared with both static and fatigue model results.

2.2 Analytical modelling

2.2.1 Analytical modelling for prediction of static failure strain

In order to evaluate the threshold strain to be applied to the specimen at which propagation of damage due to buckling occurs, a theoretical analysis was performed. Here the assumed mode of buckling is one in which a delamination is opened, see Figure 2.1-a. A closing mode has also been observed for some laminates, see Figure 2.1-b, but this is not modelled here. Laminate-foam separation is not covered within this study

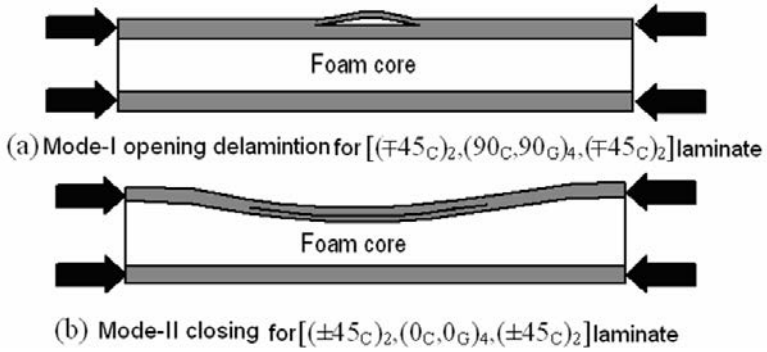

Figure 2.1: Different buckling modes of the two sandwich specimens with different face laminates.

The critical strain level for the thin sub-laminate to buckle was first calculated, from which it was possible to determine the strain at which propagation of the damage occurred from previous work [32]. The critical buckling strains were determined using the software VICONOPT [35], which models the sub-laminate as a series of joint finite strips. VICONOPT is a Fortran 77 program for exact vibration and buckling nalysis or design of prismatic plate assemblies. The program uses Fourier series to derive the governing differential equations for a plate by calculating the total potential energy. It models the plate as a series of connected strips with their ends are constrained in order to approximate the plate boundaries. The buckling deformation is approximated by trigonometric series functions along the strip longitudinal axis. The program is efficiently capable to model buckling of anisotropic plates. The critical loads for the system are obtained using eigenvalue analysis. The analysis of composite sub-laminates is performed by initially calculating the strain field produced by the base plate. The obtained strain is then applied on the sub-laminate to calculate the buckling strains.

The edges of the strips were constrained by nodes approximating a circular or elliptic boundary, as in Figure 2.2, along which the thin sub-laminate is assumed to be clamped. The critical strain depends on the face layup, delamination size and its position within the layers of the laminate. A unit axial compressive strain is applied to the full laminate before the load vector acting on the sub-laminate is obtained assuming compatibility around the delamination perimeter. This load vector is entered into VICONOPT to obtain the critical buckling strain of the thin sub-laminate produced by the delamination. The threshold strain, ϵ_{th}, at which the damage propagates is calculated as follows [32]:

$$\epsilon_{th} = \epsilon_c \left(-1 + \sqrt{4 + \frac{2G_{IC}}{(\epsilon_c)^2 A_{11}}} \right) \tag{2.1}$$

where ϵ_c, A_{11}, G_{IC} are respectively the buckling strain, the axial stiffness of the thin sub-laminate in the direction of load and the strain energy release rate for Mode-I propagation.

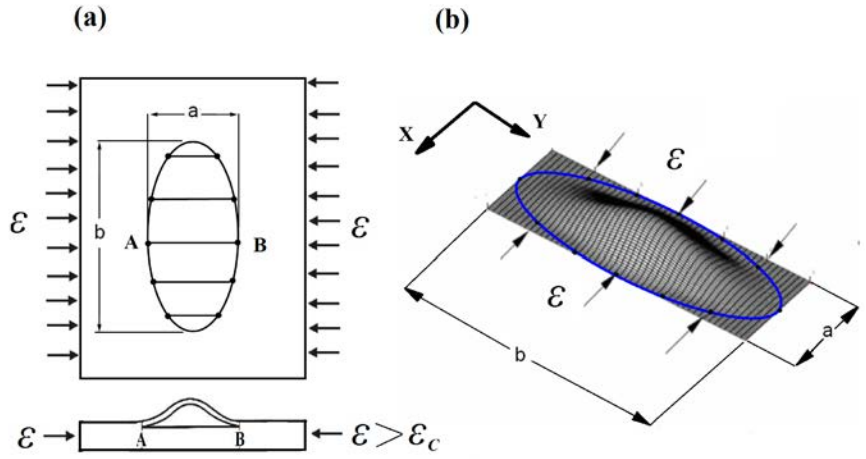

Figure 2.2: Thin-film model showing (a) plan view of an elliptical sub-laminate illustrating VICONOPT discretisation technique, (b) post buckled mode for the sub-laminate.

The initial damage morphology was modelled as accurately as possible to represent the actual impact damage in the specimen. Here the delamination at each interface must be determined by through-thickness imaging or sectioning of the damage.

2.2.2 Analytical model for prediction of fatigue threshold strain

In the case of fatigue loading, the damage was assumed to have grown to reach a critical state at which propagation is in the final stage of growth just prior to rapid growth and failure [43]. Here, the delamination shape and size is assumed to be a circle of diameter that just contains all of the initial damage indicated by the post-impact C-Scan. This delamination was modelled, in turn, at each possible interface within the laminate. The threshold strain, given by Equation 2.1 , was calculated for each delamination position and the fatigue threshold was taken as the lowest value of the threshold strain. Such strain value indicated the critical interface.

2.3 Experimental setup and specimen sizing programme

2.3.1 Objectives

The analytical methodology was based on studying buckling-driven delamination as a means to predict the failure strain of composite laminates under compression static and fatigue loading. The models assumed that the delamination would occur under uni-axial strain, hence the experimental setup should ensure sufficient axial compression strain through the sandwich faces. The outcome of the experimental investigation was to offer suitable specimen configurations and appropriate test setups to fulfil the analytical model assumptions. The initial experimental study was carried out in two steps. The first step was to study the effect of core thickness on the impact damage size and shape morphology. In order to do that, sandwich specimens with two core thicknesses, 8 mm and 20 mm, were used. The impact damage morphology of the different core specimens was investigated using different non-destructive techniques.

The second step was to carry out static and fatigue test trials on both specimen configurations. The main purpose was to investigate the capacity of different test setups to induce damage propagation within the impact without any stiffness loss within the faces. This was to exert sufficient loading for the impact damage to propagate up to failure without failing the foam core or exhibiting any overall face buckling. The testing procedures were also performed to ensure an even and uniform axial strain field within the sandwich faces throughout the test. The specimen face layups in the study were $[(\mp 45_C)_2,(90_C,90_G)_4,(\mp 45_C)_2]$ and $[(\pm 45_C)_2,(0_C,0_G)_4,(\pm 45_C)_2]$, respectively.

Specimens with the two different thicknesses were initially manufactured then impacted by 8J. The impact energy level was decided based on a previous study on a similar specimen configuration to induce sufficient damage size on the face laminate [82].

Six specimens with 8 mm core thickness were utilised for the initial study. The specimens, designated as Test-1 to Test-6, had similar face layup as the proposed

laminates. Two tests, Test-1 and Test-2, were performed on an 8 mm core specimen under static load to investigate the occurrence of damage propagation prior to other specimen failure mechanisms. Test-3 and Test-4 were carried out to explore the applicability of the DIC technique to monitor the damage propagation during the test. Test-5 and Test-6, were conducted to verify the capacity of the specimen configuration to withstand fatigue loading.

Figure 2.3 shows a 2D view of the sandwich specimen geometry. The dimensions were proposed to allow for clamping on a standard impact fixture window of 125×75 mm. The specimen also had an H shape in order to facilitate gripping on the compression loading fixture and avoid any excessive load application directly on the foam core i.e. the axial compression strain was ensured to be applied through the faces.

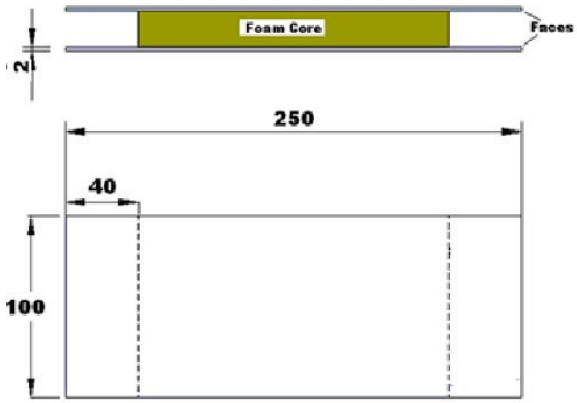

Figure 2.3: Pilot specimen dimension (All dimensions are in mm).

The impact test results shown in Table 2.1 show that the core thickness had no significant effect on the maximum impact load. The force-time response of the impact for both specimens is shown in Figure 2.4.

Table 2.1: Impact parameters for 8 mm and 20 mm core specimens.

Core thickness (mm)	Maximum load (N)	Impact velocity (m/s)	Total time (ms)	Impact energy (J)
8	4709	1.6	6.2	7.76
20	5091	1.6	5.9	7.82

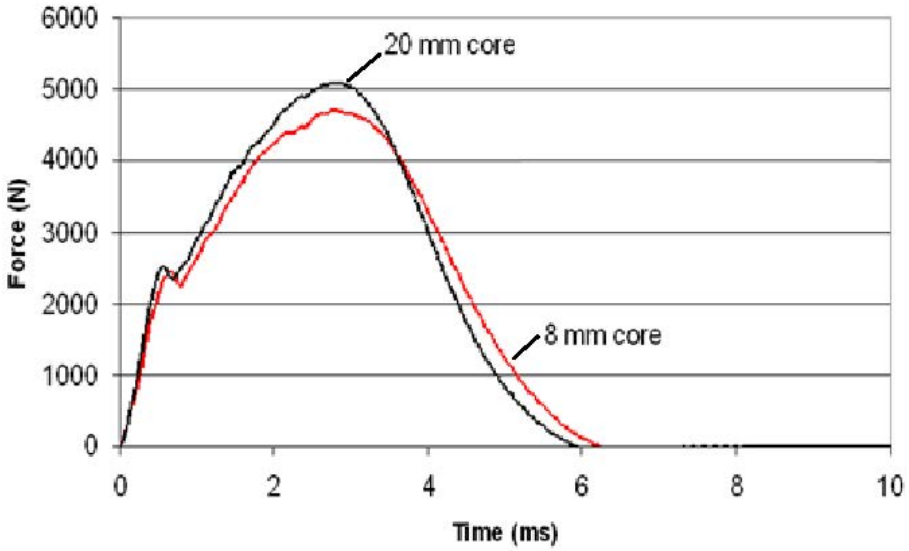

Figure 2.4: Impact response of 8 mm and 20 mm core specimens.

2.3.2 Overall buckling calculations for sandwich specimens

In order to check for the likelihood of any overall buckling of the sandwich specimen under compressive loading, the critical buckling load was calculated for the different tested configurations. The following Allen's formula [83] was used to calculate the modified critical buckling load for the sandwich section.

$$P_{cr} = \frac{P_E}{1 + P_E/(AG_C)} \tag{2.2}$$

The load was calculated in terms of the specimen geometry, face laminate stiffness, the core shear strength and the Euler buckling load for the section.

P_E is the Euler's critical load for the laminate faces assuming fixed-fixed conditions:

$$P_E = \frac{4\pi^2 (EI)_{eq}}{L^2} \tag{2.3}$$

where L is the beam length, and $(EI)_{eq}$ is the equivalent bending stiffness of the

sandwich cross-section, which is calculated as follows:

$$(EI)_{eq} = 2E_f bf(c + f/2)^2 \tag{2.4}$$

E_f is the face modulus in direction of the load, while f, b and c are section dimensions shown in the following Figure 2.5. The modified area, A is obtained as: $A = b(2c + f)$ and G_C is the core shear modulus.

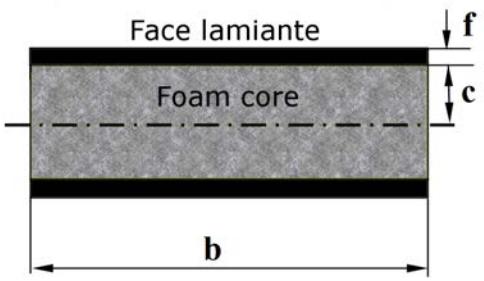

Figure 2.5: Sandwich specimen section parameters.

The stiffnesses for $[(\mp 45_C)_2,(90_C,90_G)_4,(\mp 45_C)_2]$ and $[(\pm 45_C)_2,(0_C,0_G)_4,(\pm 45_C)_2]$ face laminates were obtained using a laminate analysis software as 22 GPa and 55 GPa, respectively. The shear modulus, G_C, and the density of the foam core were 70 MPa and 110 kg/m^3, respectively. The critical loads for the aforementioned specimen configurations are shown in Table 2.2. The slight change between the calculated values of the critical load shown in Table 2.2 was due to the fact that the critical load was mostly dominated by the core shear modulus rather than face moduli as can be seen from Equation 2.2.

Table 2.2: Overall buckling loads for different specimen configurations for sandwich specimens $[(\mp 45_C)_2,(90_C,90_G)_4,(\mp 45_C)_2]$ and $[(\pm 45_C)_2,(0_C,0_G)_4,(\pm 45_C)_2]$ face laminates. Loads are in kN.

Free length (mm)	80		60	
Core thickness (mm)	8	25	8	25
$[(\pm 45_C)_2, (0_C, 0_G)_{4S}, (\pm 45_C)_2]$	72	189	73	190
$[(\mp 45_C)_2, (90_C, 90_G)_{4S}, (\mp 45_C)_2]$	71	187	72	189

2.3.3 Evaluation of damage morphology

In order to evaluate the damage size, a thermography camera was used. Although the damage size in both specimens appears to be equal, the technique did not give a clear image for the whole depth of the specimen face. Figure 2.6 shows the image of the damage obtained from thermography. Damage in both specimens was observed as an elliptical shape with an approximate major axis dimension of 33 mm.

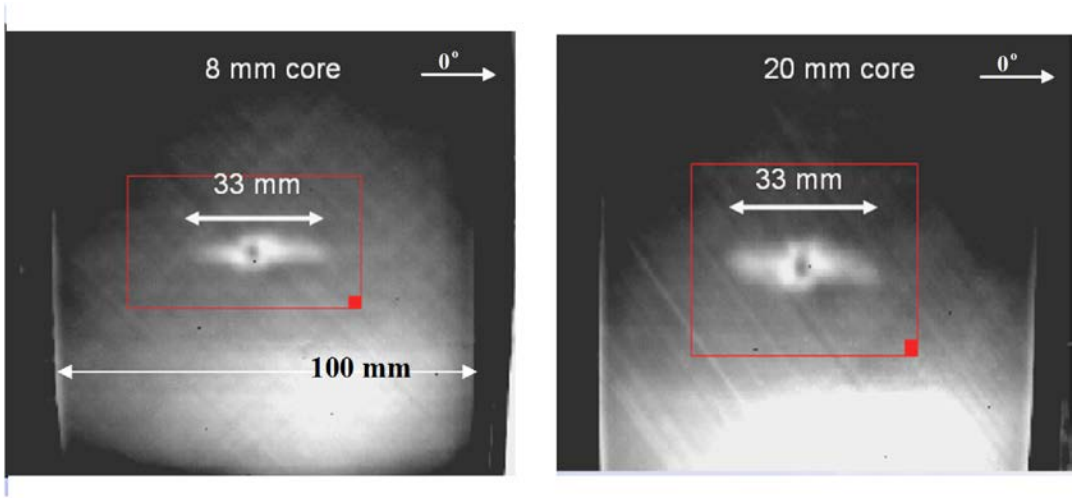

Figure 2.6: Thermography images for the damage in 8 mm and 20 mm thick core specimens.

Both specimens were then scanned using an ultrasonic C-Scan system to observe the damage morphology within the face laminate and to obtain a clear shape of damage through the thickness. A 15 MHz ultrasonic probe was used to perform the scan. It was found that both types of specimens had a similar size at the prescribed impact energy level. Figures 2.7 and 2.8 show the C-Scan image for the 8 mm and 20 mm core specimens, respectively. The damage in both specimens included two distinctive morphologies, an ellipse which existed near the impact surface and two peanut shapes seemed to exist at a deeper level.

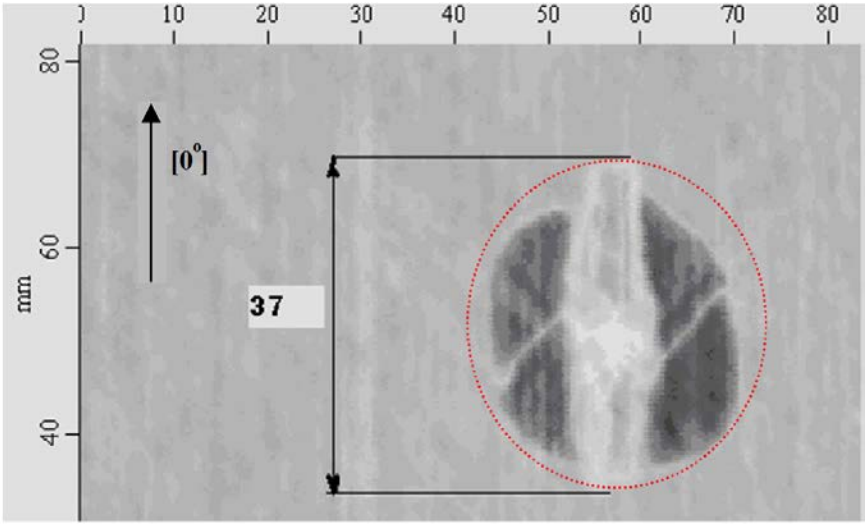

Figure 2.7: C-Scan image of 8 mm thick core specimen.

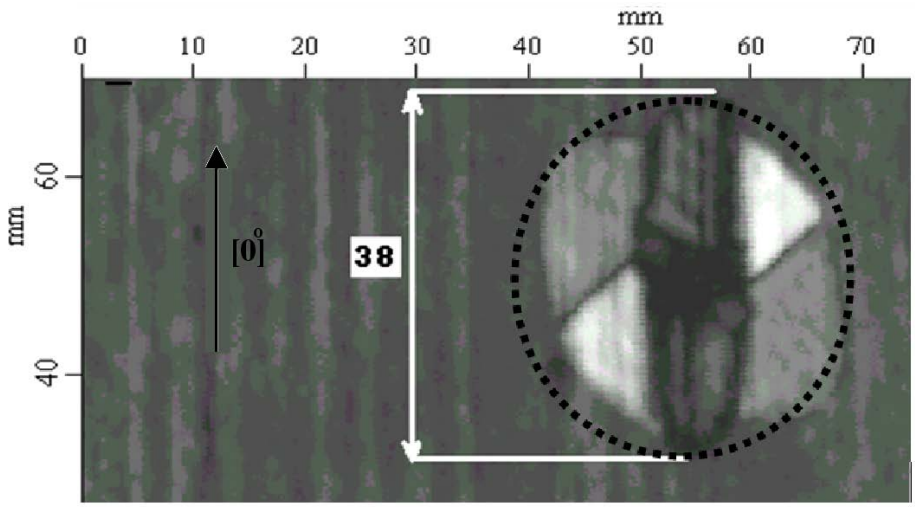

Figure 2.8: C-Scan image of 20 mm thick core specimen.

In order to better visualise the levels at which delamination would commonly take place as a result to impact, one of the impacted specimens with 8 mm core thickness was cut through the central axes at the impact point. The cut piece was then moulded in a transparent resin and polished to allow clear visualisation of the cut section by an optical microscope. It was clear that there was a local separation between the foam core and the impacted face of about 22 mm length just below the impact position. The optical micrograph in Figure 2.9 shows that a layer separation existed between after 4^{th} ply near the core. This separation was the longest among other separations within the thickness.

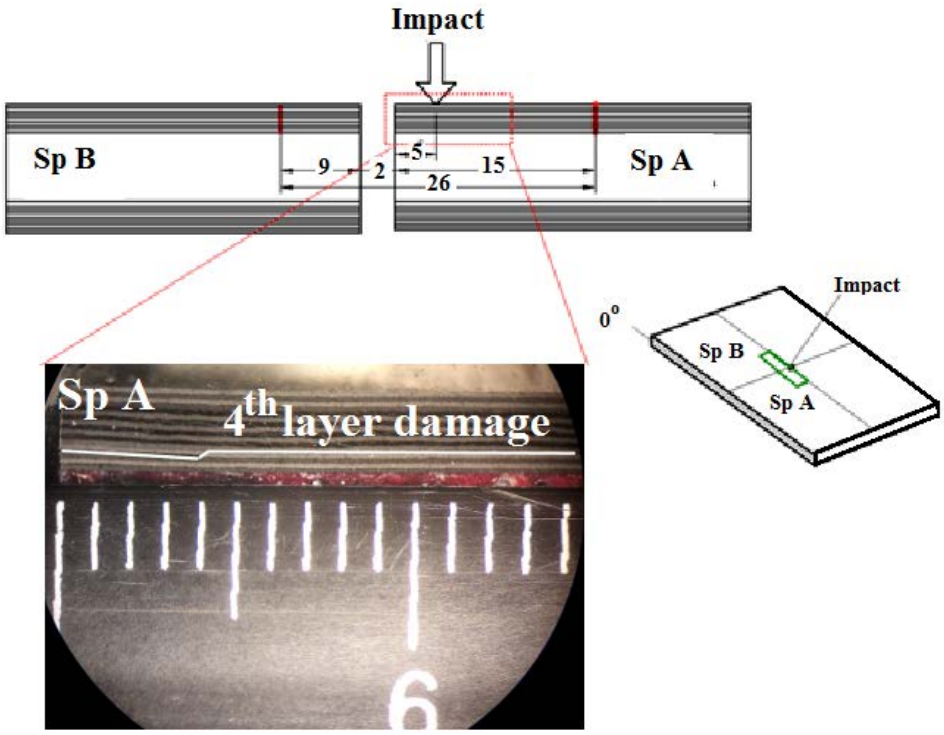

Figure 2.9: Damage at the point of impact, Top: position of impact. Right: Cutting position of the sample. Bottom: Optical microscope showing layer separation of one sample.

A further specimen with 20 mm thick foam core was investigated. Two sections were cut along axes A-A and B-B, shown in Figure 2.10, in order to better understand the position of the longest delamination dimensions across the thickness. The vertical cut plane A-A shows a maximum dimension of 30 mm existed between the fourth and fifth layer, whilst looking at the section taken through plane B-B demonstrated a corresponding delamination of 8 mm length after the fourth layer. As the cutting planes might have not been accurately taken through the centre spot of the damage as shown in the C-Scan image, different dimension measurements were observed when compared with the sectional views. It can be concluded that there were two significant damage morphologies through thickness: an elliptical damage shape near the surface with major and minor axes aligned with the [0] and [90] directions in the laminate; and another damage enclosed within a circular pattern situated at a deeper level near the foam core.

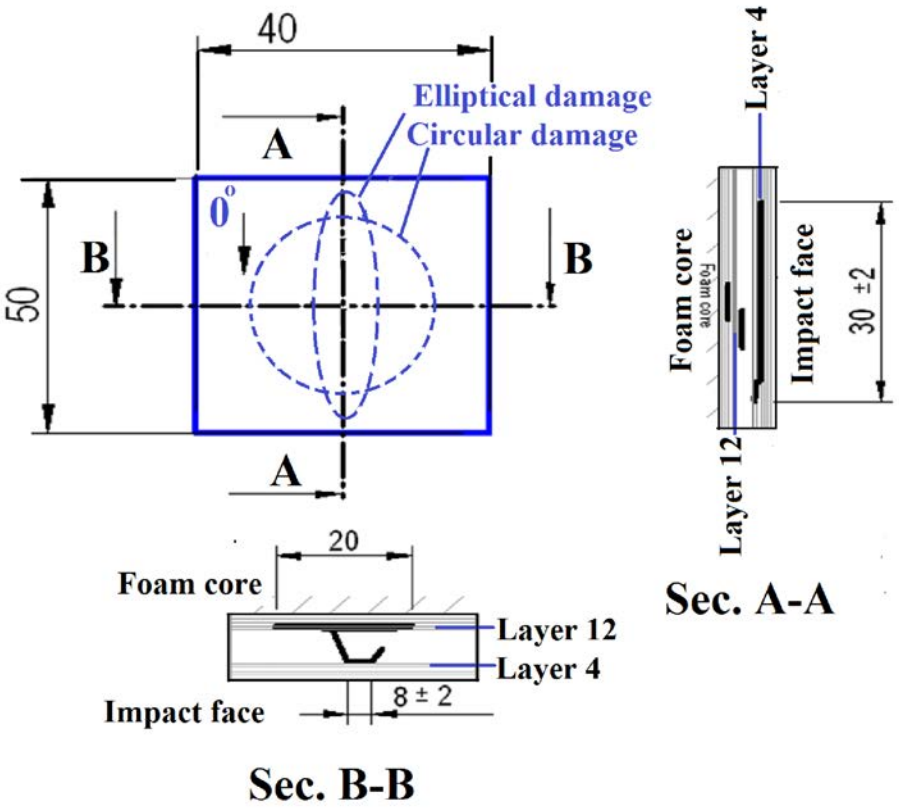

Figure 2.10: Sectional view of 20 mm core specimen damage.

2.3.4 Fixture design

In order to apply compressive loading through the faces, a loading fixture was designed and manufactured to evenly apply the compression load to the specimen ends without inducing any overall buckling of the specimen or excessive shear in the foam core. The testing setup was designed to induce an axial strain field in the damaged face enough for the delamination to propagate without causing overall buckling of the specimen or foam damage. The fixture consisted of two main halves to be mounted on the machine grips. The ends of the specimens were fixed by the fixture's movable grips. The fixture is similar to that prescribed in the ASTM C364-99 technical standard, [84]. Figures 2.11 and 2.12 show 3D and a 2D scheme of the fixture.

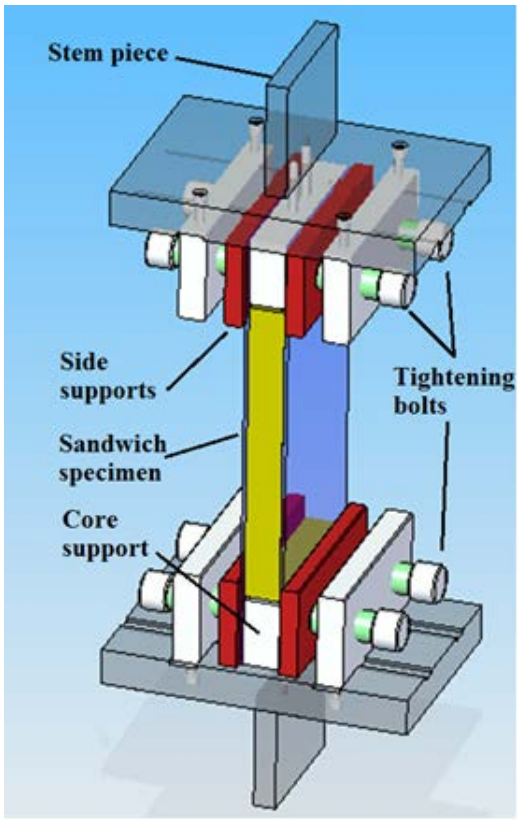

Figure 2.11: 3D view of the loading fixture.

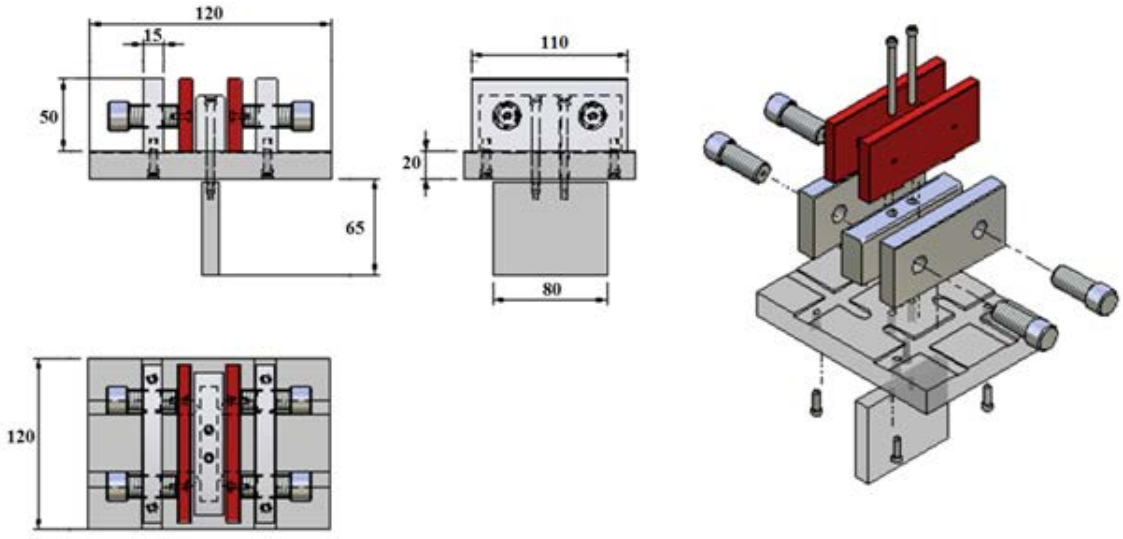

Figure 2.12: 2D and exploded views of the fixture.

Different tests were performed to investigate the influence of impact damage on the static and fatigue behaviour of sandwich specimens. The programme consisted of two phases: the first one was to evaluate the static strength of the specimens after impact; the second was to investigate the fatigue behaviour of the sandwich specimens. Table 3.4 below summarises the different parameters for the following tests.

Table 2.3: Test result summary for sandwich specimens with 8 mm core.

Test No.	Face laminate	Free length (mm)	Longitudinal modulus (GPa)	Failure strain (μstrain)	Failure mode
1	$[(\pm 45_C)_2,(0_C,0_G)_4,(\pm 45_C)_2]$ static	120	55.9	3560	face buckling
2	$[(\pm 45_C)_2,(0_C,0_G)_4,(\pm 45_C)_2]$ static	60	56.0	3650	face buckling
3	$[(\pm 45_C)_2,(0_C),(0_G)_7,(\pm 45_C)_2]$ static	120	40.2	4200	face buckling
4	$[(\pm 45_C)_2,(0_C),(0_G)_7,(\pm 45_C)_2]$ static	80	38.8	6300	face buckling
5	$[(\pm 45_C)_2,(0_C),(0_G)_7,(\pm 45_C)_2]$ fatigue	60	56.0	—	edge brooming
6	$[(\pm 45_C)_2,(0_C),(0_G)_7,(\pm 45_C)_2]$ fatigue	60	56.0	—	edge brooming
7	$[(\mp 45_C)_2,(90_C,90_G)_4,(\mp 45_C)_2]$ static	60	22.0	6200	face damage
8	$[(\pm 45_C)_2,(0_C,0_G)_4,(\pm 45_C)_2]$ static	60	56.0	5400	face buckling
9	$[(\pm 45_C)_2,(0_C,0_G)_4,(\pm 45_C)_2]$ static	60	56.0	3900	edge failure
10	$[(\pm 45_C)_2,(0_C,0_G)_4,(\pm 45_C)_2]$ static	60	56.0	5250	edge brooming

2.3.5 Test-1: Static testing of undamaged specimen with 8 mm core

Specimens with 8 mm foam core were initially tested. An undamaged specimen was initially tested to evaluate its longitudinal modulus and final failure mode under compression. Six strain gauges were attached to both surfaces using the methodology outlined in Appendix A. The gauges helped checking that the strain

distribution was uniform and even through the faces. An initial load was applied in order to ensure a uniform strain distribution through the faces. The levelling of the specimens was then accomplished by inserting metallic shims below the face edge that exhibited lower strain readings after removing the load. Low load levels were steadily applied up to 5, 10 and 20 kN. During each step, the load was halted at each level and strain measurements were monitored. If a bigger deviation than 10% of strain was obtained compared with the average attained strain level, levelling with the shims was repeated until a satisfactory strain distribution was obtained. The fixture in Figure 2.11 was used to support the specimen by clamping both ends and establishing a built-in condition. The test speed was 12 kN/min. An apparent longitudinal modulus of 55.9 GPa was calculated using the average faces cross sectional area. At a load level of 77 kN, corresponding to strain level of 3560 μstrain, an overall buckling occurred and excessive shear in the foam core was observed resulting in final failure of the specimen. The experimental buckling load was found to be slightly higher than the predicted value, 71 kN, using Equation 2.2.

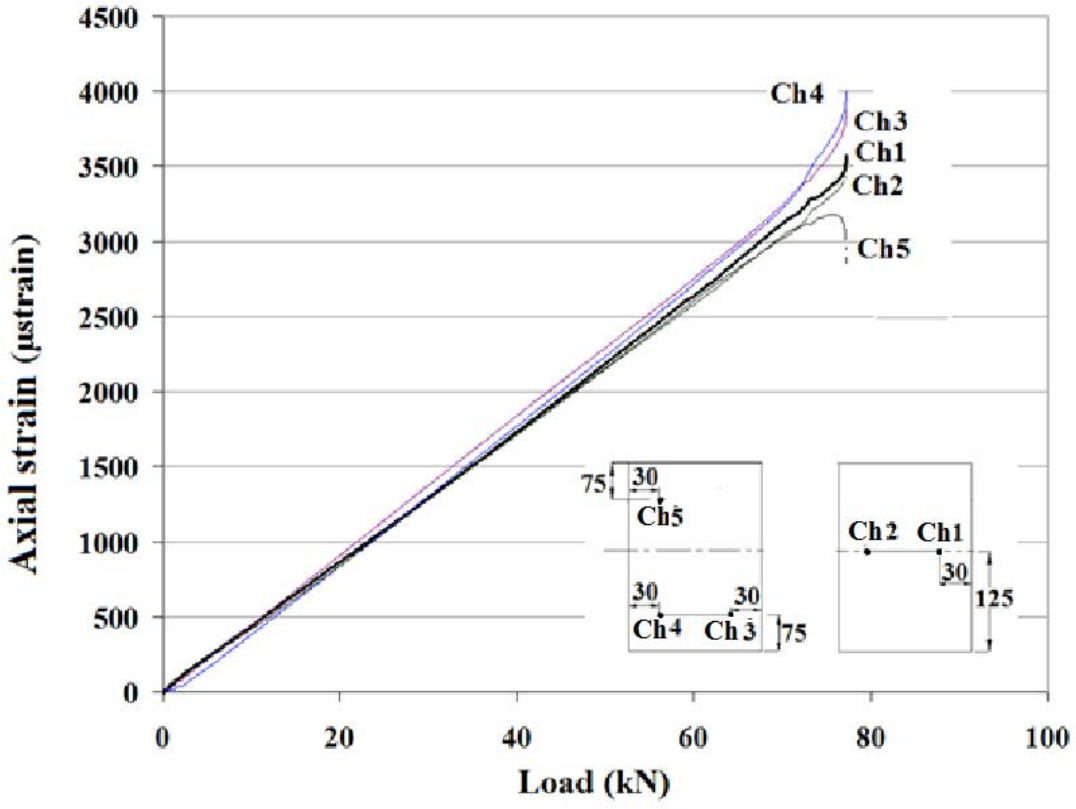

Figure 2.13: Load-strain plot for an un-impacted specimen with 8mm core, Test-1.

2.3.6 Test-2: testing an impacted specimen with 8 mm core

In order to avoid the overall buckling, a smaller unsupported length was chosen. The unsupported lengths on the impact and back faces were 60 mm and 25 mm, respectively. The test setup is shown in Figure 2.14. The average estimated modulus from the test was 56 GPa. By examining the strain distribution in Figure 2.15, face buckling seemed to start at a load level of 60 kN followed by an overall buckling at a load level of 77 kN towards the impact face direction. Compared to Test-1 setup, although the specimen had face damage, no evidence of face damage growth was visualised using the ultrasonic C-Scan after the test.

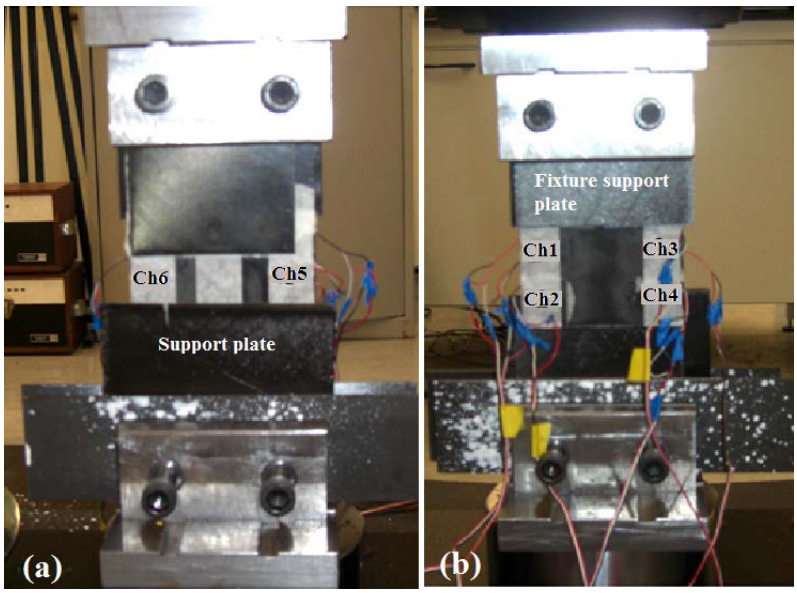

Figure 2.14: Test setup and strain gauge positions for a sandwich specimen with 8 mm core, Test-2. (a) Back face, (b) Impact face.

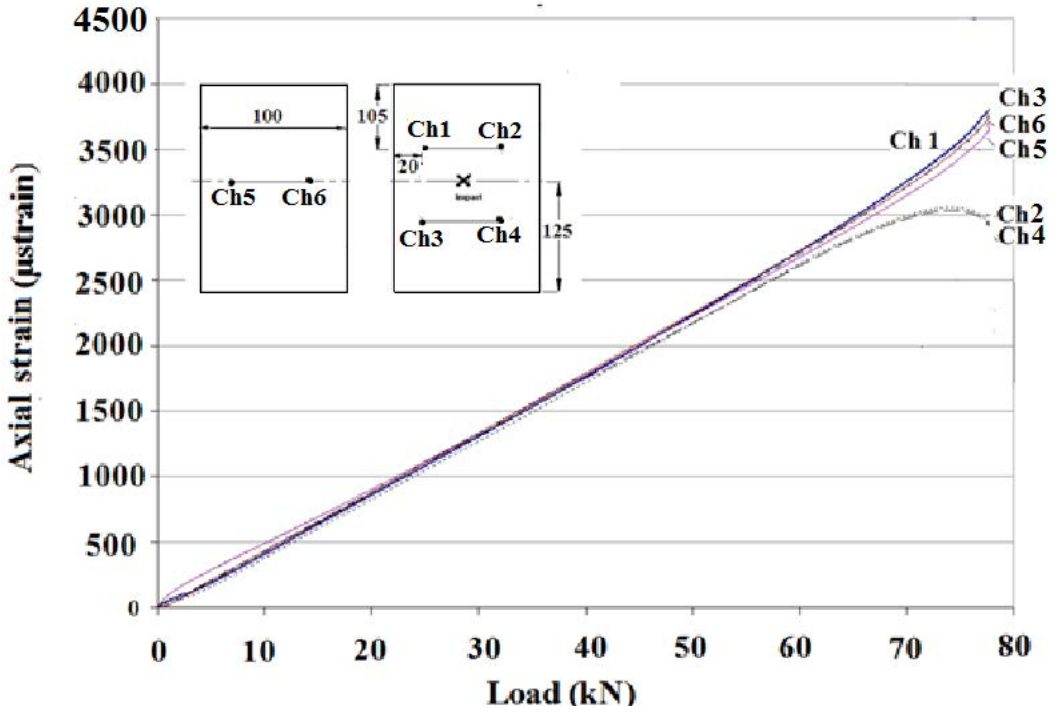

Figure 2.15: Load-strain plot for an impacted specimen with 8mm core, Test-2.

2.3.7 Test-3: Static test of a sandwich specimen with 8 mm core

Two impacted specimens with $[(\pm 45_C)_2, (0_C), (0_G)_7, (\pm 45_C)_2]$ face laminates were tested to calibrate a non-destructive technique, DIC, used to monitor the outer face deformation. Both specimens, labelled as Test-3 and Test-4, were impacted with 8 J using the same impact test configurations. The C-Scan images for both specimens showed a similar damage pattern to the previous specimens. The maximum damage was enclosed within a circle diameter of 37.2 mm. The first specimen was inserted and fixed using the fixture in Figure 2.12. The side plates in each grip were tightened against specimen edges in order to ensure built end condition at both specimen sides. Four strain gauges were attached to the specimen surfaces at the positions described in the Figure 2.16. The gauges were initially used to induce an even axial load in both faces at the start of the test using the levelling procedure described above. The procedure was repeated until a reasonable deviation of strain was visualised. The test speed was 0.15 mm/min corresponding to 12 kN/min. It was observed that channel 1 was malfunctioning

during the test and hence was not included on the graph below. Final failure of the specimen took place at a load level of 76 kN corresponding to strain level of 4200 μstrain. The failure was due to overall buckling of the specimen which induced excessive foam shear. Figure 2.17 shows the foam failure pattern after the test. The effective compressive modulus for the specimen was calculated using the average strain trend from the data and the average faces area. The nominal experimental modulus was found to be 40.2 GPa, lower than the previous specimens measured modulus value of 56 GPa. The predicted buckling load for the tested configuration was 70 kN, which was smaller than the experimental load level.

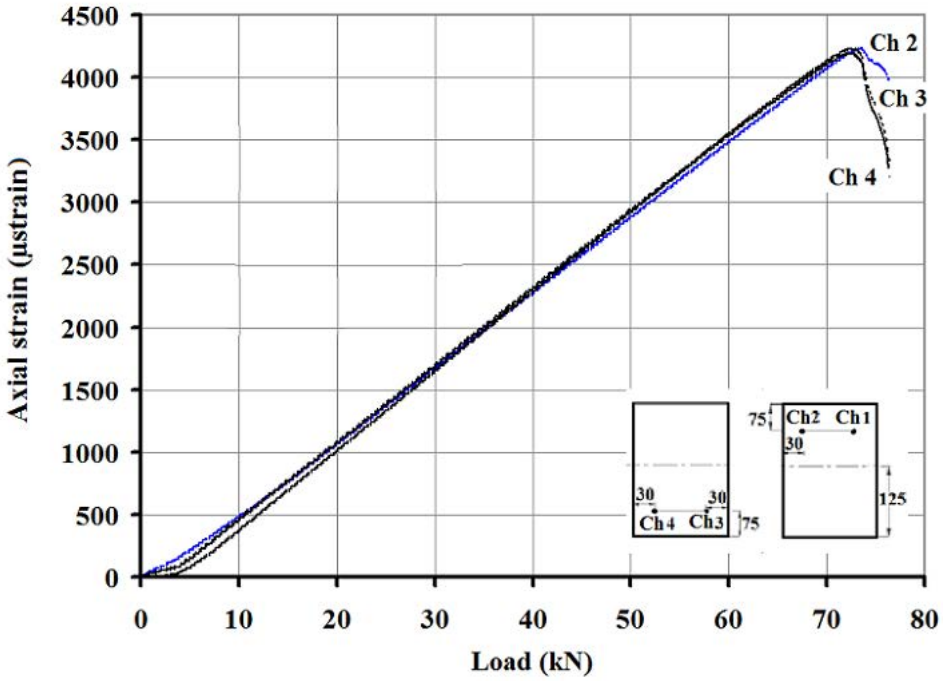

Figure 2.16: Load-strain plot for an impacted specimen with 8mm core, Test-3.

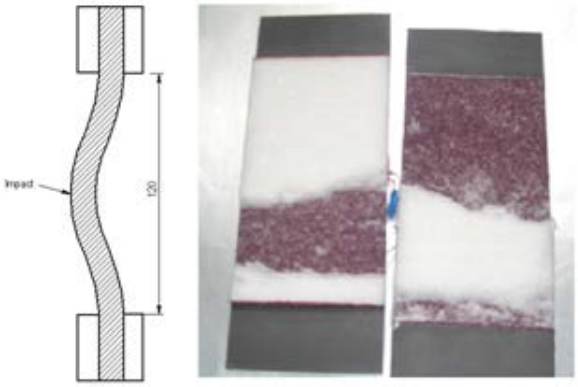

Figure 2.17: Failure pattern of Test-3 specimen.

2.3.8 Test-4: Static testing of a sandwich specimen using DIC technique

The second specimen with 8 mm foam core and $[(\pm 45_C)_2, (0_C), (0_G)_7, (\pm 45_C)_2]$ face laminates was tested under static compression using an Instron screw-driven machine. In order to observe the outer face deformation, Digital Image Correlation (DIC), shown in Figure 2.18, technique was utilised. Six strain gauges were attached to both impact and back faces of the specimen as shown in the scheme in Figure 2.19. In order to investigate its fidelity as a measuring technique, the strains obtained from the strain gauges were compared with the average face strain collected using the DIC technique. The DIC post processing software also allowed the deformation of the surface in three dimensional coordinates to be extracted (as shown in Figure 2.20). While Figure 2.21 shows the out-of plane deflection curves taken at a vertical cut plane through the impact face. Near a failure load of 80 kN, corresponding to 6300 μstrain, an overall surface buckling occurred. The latter result could also be observed from the strain plot in Figure 2.19. It can be shown that the damage initially buckled towards the foam side before overall specimen buckling occurred. The strain plot shows that that the obtained strain from the DIC results was in perfect match with the average acquired strain using the gauges.

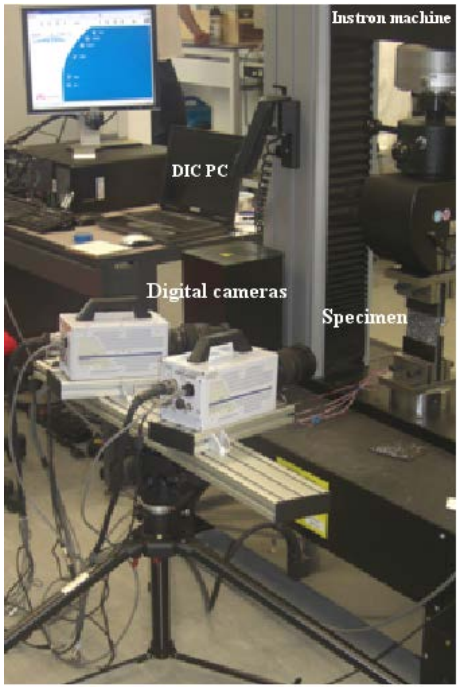

Figure 2.18: Test setup for sandwich specimen using a DIC system, Test-4.

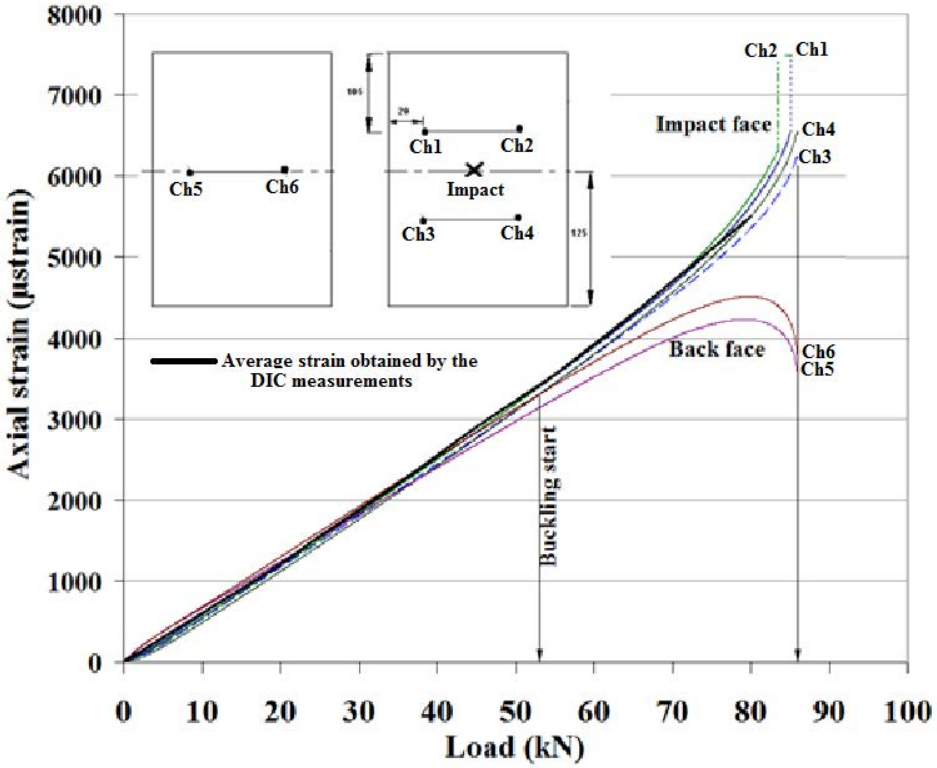

Figure 2.19: Load-strain plot for an impacted specimen with 8 mm core, Test-4.

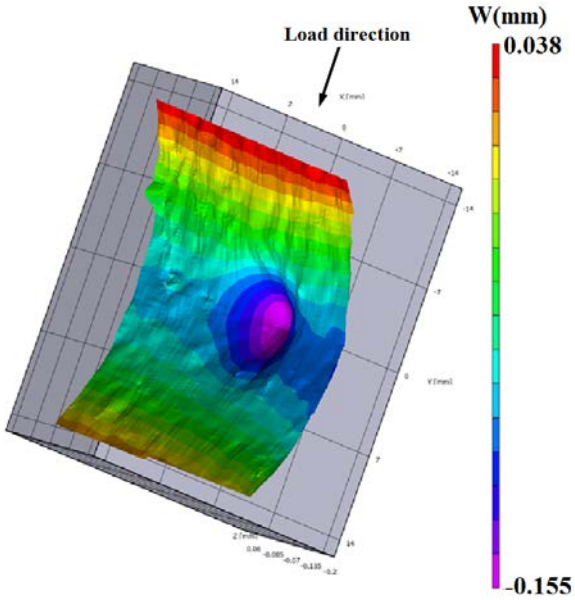

Figure 2.20: 3D representation of out-of-plane displacement of the damage face for Test-4 sandwich specimen.

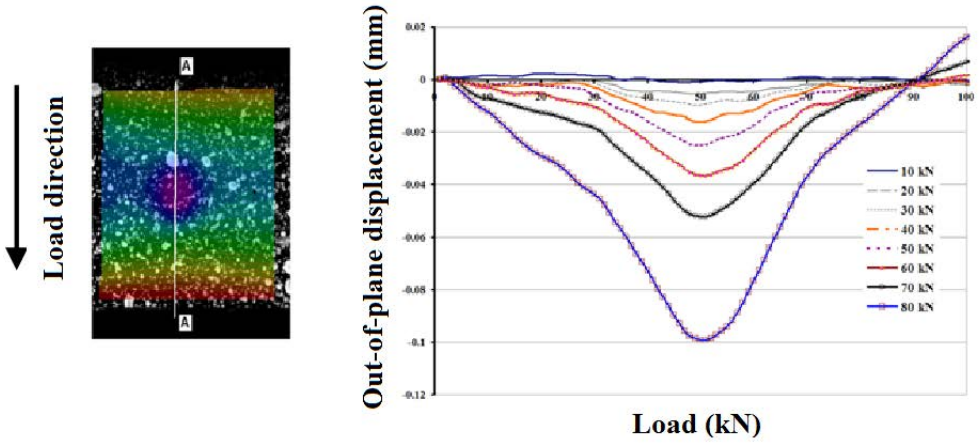

Figure 2.21: Out-of-plane displacement curves measured at a sectional plane A-A.

Although the specimens in Test-3 and Test-4 had lower estimate of the longitudinal moduli obtained from the experimental strain values, no face damage propagation occurred at the higher strain value compared to the rest of the previous tested specimens with $[(\pm 45_C)_2,(0_C,0_G)_4,(\pm 45_C)_2]$ and $[(\mp 45_C)_2,(90_C,90_G)_4,(\mp 45_C)_2]$

face laminates. A summary for Tests 1-4 is shown in Table 3.4.

As a result of the systematic buckling of the specimens of Tests 1-4 prior to any evidence of propagation, a new fixture was designed in order to better support the tested specimen under compression, seen in Figure 2.22. The main objectives for the new design were to avoid any possible overall buckling of the specimen using steel faces. One of the faces had a window of 60×70 mm to allow for speckle pattern spread and a space to attach strain gauges, while the other face had two smaller widows of 20×20 mm to provide sufficient space for two strain gauges at the back face. The lengths of the steel faces were shorter than the specimen faces by 2.5 mm, in order to allow a possible strain level up to 12,500 μstrain during the test.

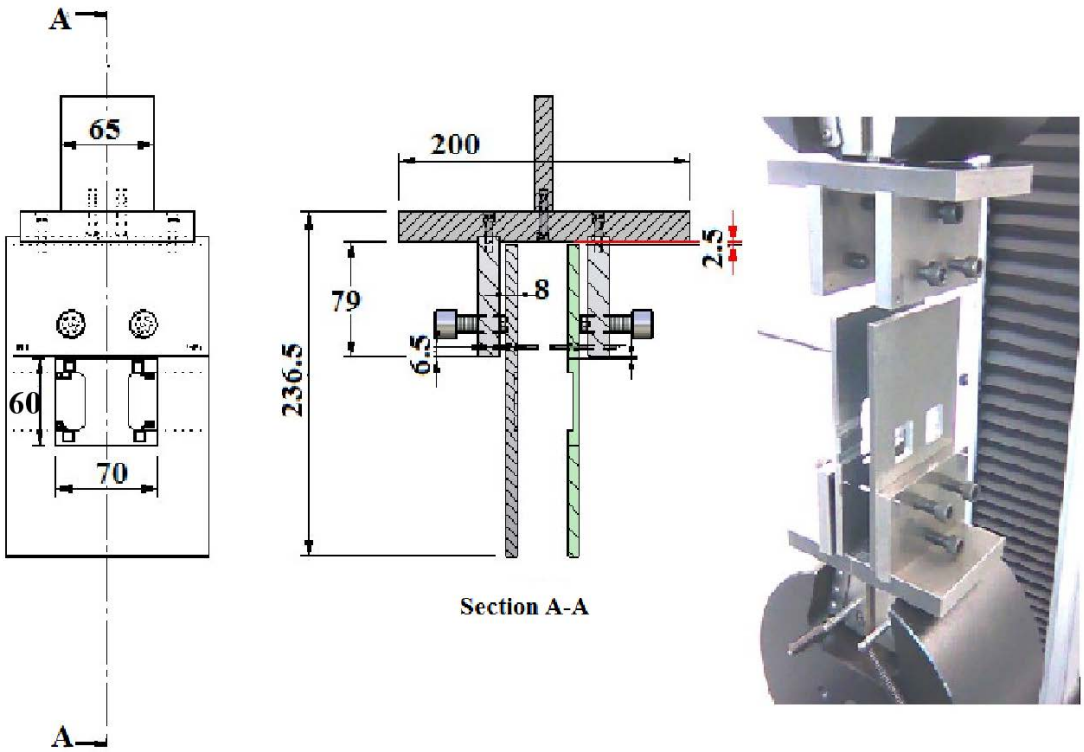

Figure 2.22: Second fixture design, all dimensions are in mm.

2.3.9 Test-5: Fatigue test of 8 mm core specimen

Fatigue tests, Test-5 and Test-6 were carried out on specimens with 8 mm core and $[(\pm 45_C)_2,(0_C,0_G)_4,(\pm 45_C)_2]$ face laminate to monitor the face damage growth

over cycles using the fixture shown in Figure 2.22. For Test-5, the compression-compression loading severity was equal to 0.58. The severity is the ratio between maximum cycle load to the average maximum failure load, (77 kN), acquired in the static tests, Test-1 and Test-2. The tests were performed using a loading ratio, $R = 10$, under load control and a loading frequency of 3 Hz. The stress waveform for Test 5 and Test 6 are presented in Figure 2.23. The strain variation within the cycle was between 220 and 2200 μstrain). The test was stopped after one million cycles. Although no overall buckling took place during the test, severe edge brooming, (edge crushing), was observed as a result of matrix crushing under the fluctuating loading. The brooming was seen to be uneven through both faces. As a result, significant strain variation of the specimen faces was monitored through the loading cycles. The specimen was then scanned by the ultra-sonic C-scan which showed no evidence of damage growth after the aforementioned number of cycles.

2.3.10 Test-6: Fatigue test of 8 mm core specimen

A second test trial was performed using a higher severity level of 0.91 and a loading frequency of 3 Hz. The load levels are defined in Figure 2.23. The test was also stopped after one million cycles and the specimen was then examined using the C-Scanner which showed no evidence of damage growth. Severe edge brooming existed at all four end parts of the specimen. Although the specimens were thoroughly tested under compression-compression loading and the gripping steel faces were strongly tightened against it, slight side-motion of the ends occurred due to the local buckling of face areas unsupported by the foam cores at the ends.

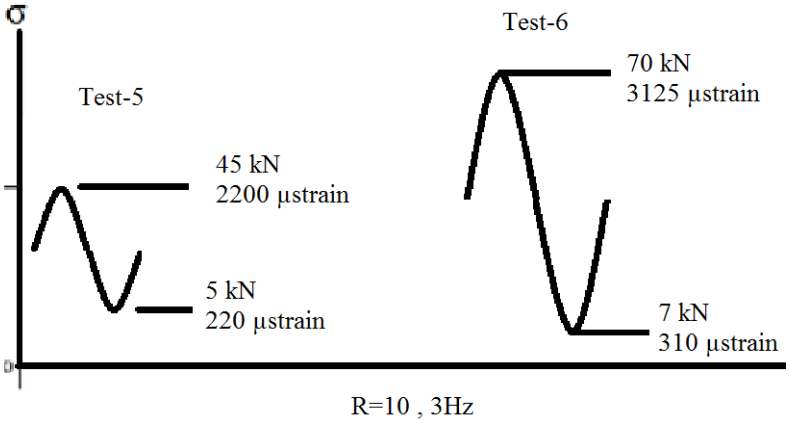

Figure 2.23: Fatigue test scheme for Tests 5 and 6.

2.3.11 Test-7: Static test of a sandwich specimen with $[(\mp 45_C)_2,(90_C,90_G)_4,(\mp 45_C)_2]$ face laminate.

The second specimen type with $[(\mp 45_C)_2,(90_C,90_G)_4,(\mp 45_C)_2]$ face laminate and 20 mm core was tested under static compression loading. Strain gauges were used as discussed previously to check any evidence for buckling of the specimen faces. In order to check uniform loading of both faces of the specimen, four strain gauges were placed on the two faces as shown in Figure 2.24. Gauges 1 and 2 were placed on the opposite face of impact and gauges 3 and 4 were on the impact face. Figure 2.25 shows the arrangements for the test. The specimen was placed on the fixture and gripped by the fixture grip. The grips were clamped into the machine jaws and a rotating pivot was inserted between the top half of the fixture and the upper jaw. The pivot eliminated any misalignment between the machine loading axis and the specimen faces.

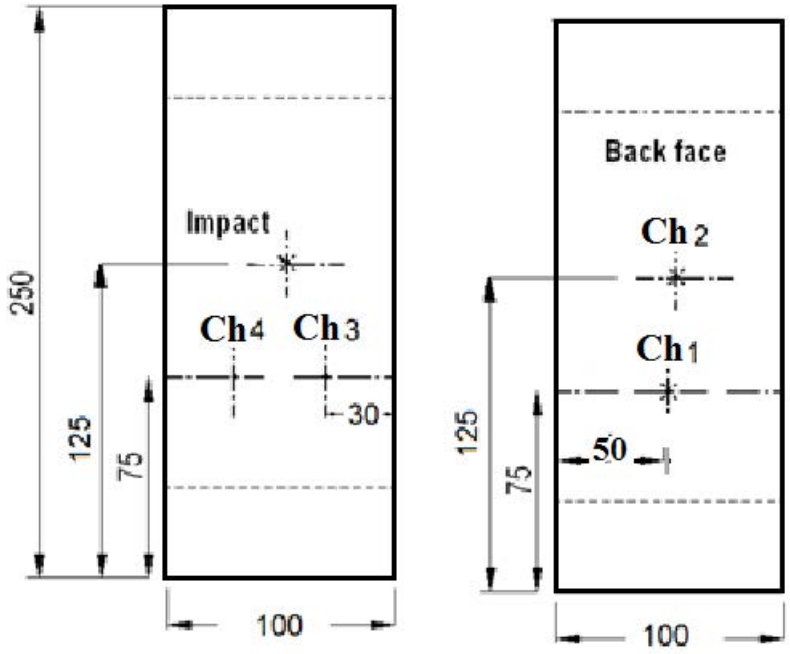

Figure 2.24: Schematic drawing for sandwich specimen with $[(\mp 45_C)_2,(90_C,90_G)_4,(\mp 45_C)_2]$ face laminate, Test-7.

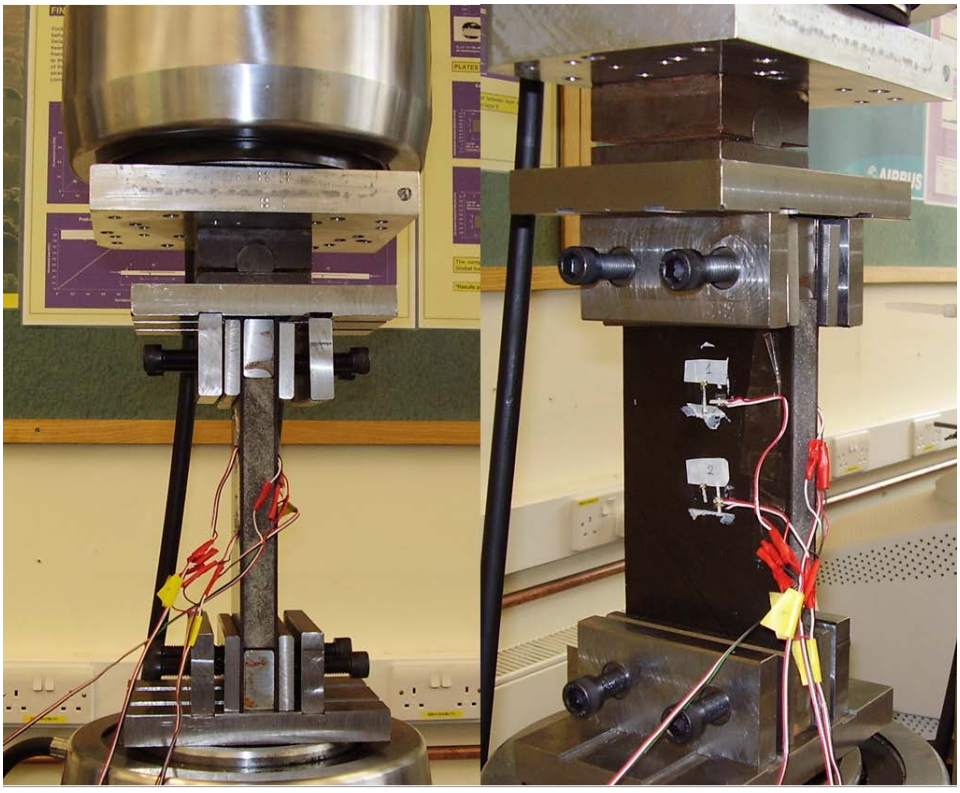

Figure 2.25: Static test setup for sandwich specimen with $[(\mp 45_C)_2,(90_C,90_G)_4,(\mp 45_C)_2]$ face laminate, Test-7.

Figure 2.26 shows the strain measurements of the sandwich specimen which showed the load was applied uniformly and linearly up to 40 kN, then the curve indicated some local buckling may have occurred between 40 and 50 kN, i.e both faces bent in the same direction. Failure occurred at 57 kN with corresponding strain of 6200 μstrain due to damage growth which resulted in layer separation.

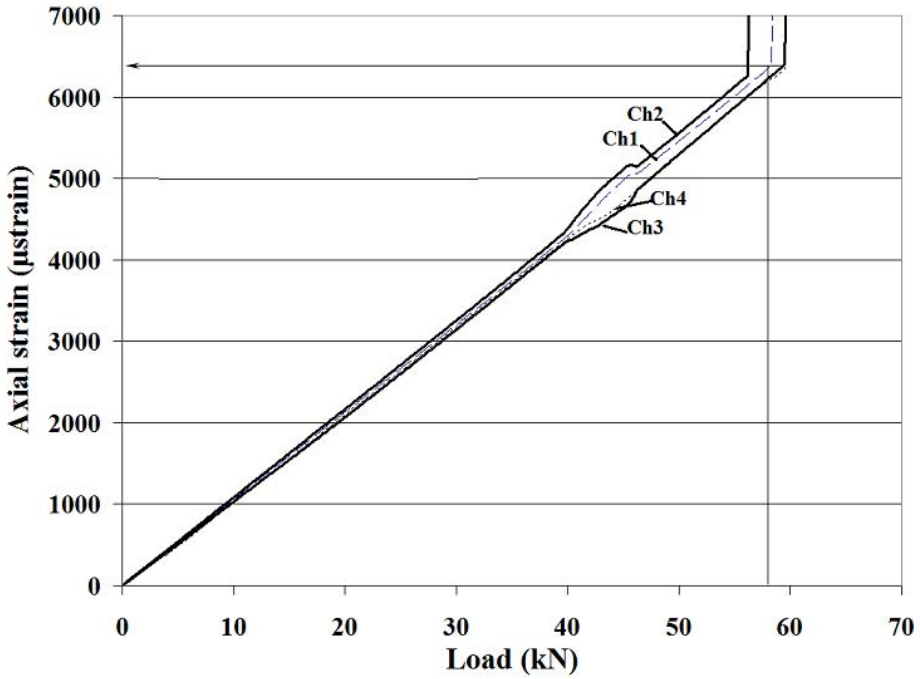

Figure 2.26: Load vs strain for sandwich specimen with $[(\mp 45_C)_2,(90_C,90_G)_4,(\mp 45_C)_2]$ face laminate.

For the rest of the static and fatigue test programme, specimens with $[(\pm 45_C)_2,(0_C,0_G)_4,(\pm 45_C)_2]$ and $[(\mp 45_C)_2,(90_C,90_G)_4,(\mp 45_C)_2]$ face laminates and different core thickness would be further investigated to establish a suitable test setup.

2.3.12 Test-8: Static test of sandwich specimen with 25 mm foam core and $[(\pm 45_C)_2,(0_C,0_G)_4,(\pm 45_C)_2]$ face laminate

After overcoming the problem found during the testing of specimens with 8 mm core, a new production batch was manufactured by the manufacturing team at

the Agusta-Westland facility, Yeovil. The new specimens were 210×100×29 mm dimensions. The core thickness was chosen to be 25 mm to avoid face buckling and to minimise the use of supporting plates.

The first specimen with $[(\pm 45_C)_2,(0_C,0_G)_4,(\pm 45_C)_2]$ face laminates was tested under static compression. The back face was fully supported by a 4 mm thick carbon composite plate, while the impact face had an unsupported length of 60 mm. Figure 2.27 shows a view for the specimen setup. Although the unsupported specimen length was less than recommended by the ASTM standard sheet, [84], impact face buckling was observed during the test at a load level of 58 kN. The experimental load was lower than the predicted value, 189 kN, calculated by Equation 2.2. The graph in Figure 2.28 shows the face buckling affects the strain trends of both faces. After the test, the specimen was inspected and excessive shear was observed within the foam core and the edges were severely crushed and broomed. There was no propagation of the face damage up until average strain level of 5300 μstrain, measured at the impact face, and corresponding to an applied axial load of around 93 kN. After finishing the test, ultrasonic C-Scan images taken for the impact face showed no damage growth.

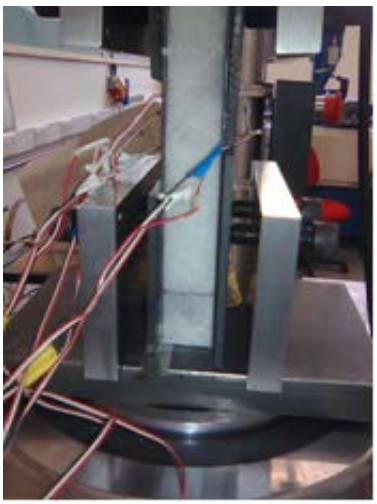

Figure 2.27: Test setup for a sandwich specimen with 25 mm foam core and $[(\pm 45_C)_2,(0_C,0_G)_4,(\pm 45_C)_2]$ face laminate, Test-8.

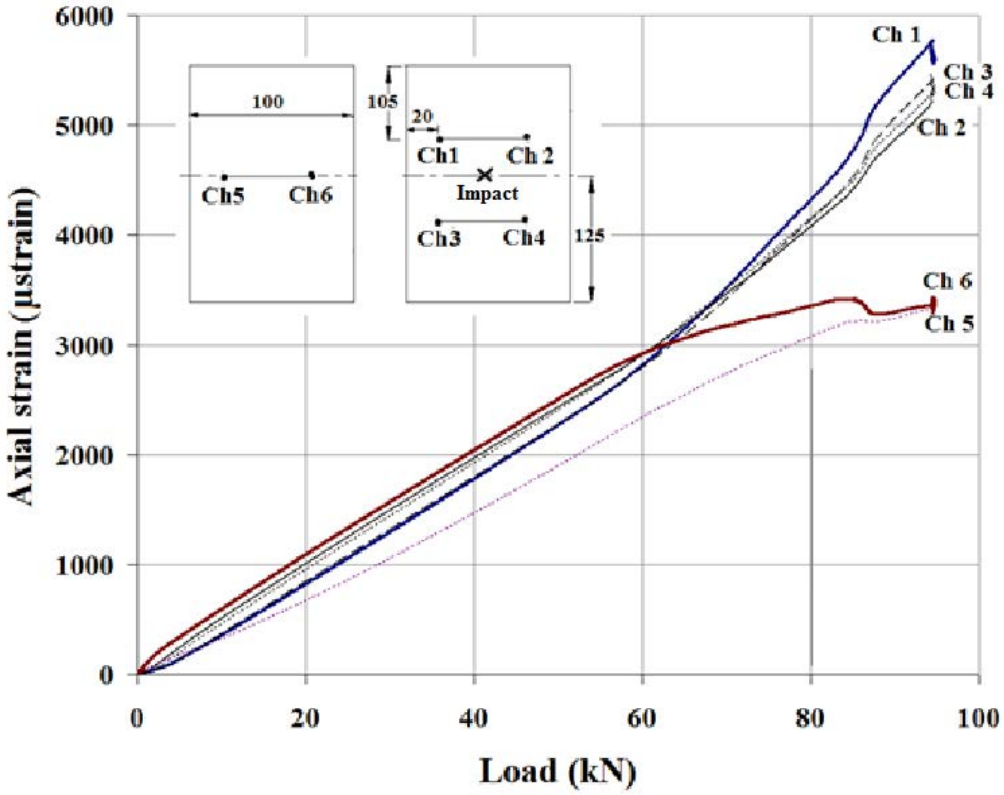

Figure 2.28: Load vs strain for sandwich specimen with $[(\mp 45_C)_2,(90_C,90_G)_4,(\mp 45_C)_2]$ face laminate, Test-8.

2.3.13 Test-9: Static test of sandwich specimen with 25 mm foam core and $[(\pm 45_C)_2,(0_C,0_G)_4,(\pm 45_C)_2]$ face laminate

A second test was repeated on a similar specimen. The new specimen dimensions were 210×75×29 mm. The reason for the shorter width was to attain a higher face strain level at a lower applied load. Both faces of the specimen were supported by 4 mm carbon composite plates while allowing an unsupported length of 60 mm. Such end conditions allowed for a load of 142 kN to be applied before face buckling occurred as predicted using Equation 2.2. From the graph in Figure 2.29 it can be concluded that strain gauge readings were fairly linear until a strain level of 3800 μstrain, at a load level of 68 kN, where the end parts of the specimen were locally buckled and bent under compression. As a result, the foam core failed by excessive shear. Although the faces were well supported, the failure

occurred due to local buckling of specimen ends near the compression plates, see Figure 2.30. No damage growth was predicted by the C-Scan technique, although the load reached was lower than the predicted buckling value.

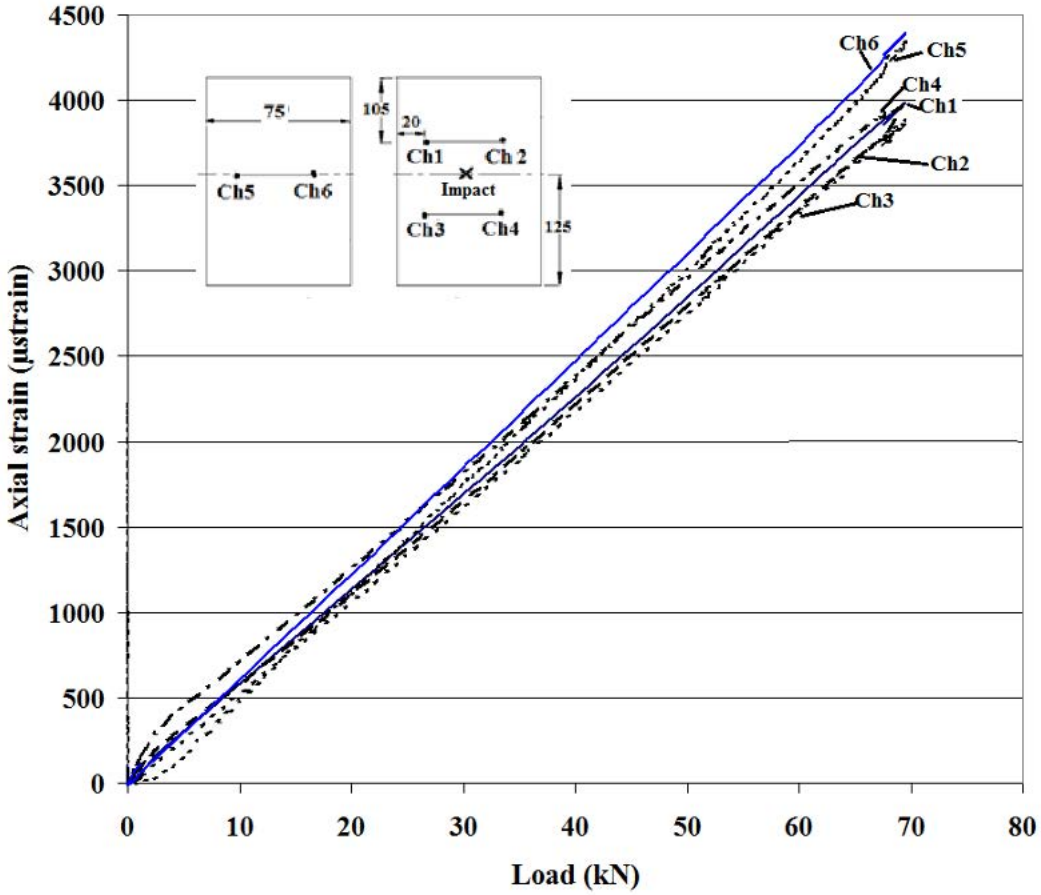

Figure 2.29: Load vs strain for sandwich specimen with $[(\pm 45_C)_2, (0_C, 0_G)_{4S}, (\pm 45_C)_2]$ face laminate, Test-9.

Figure 2.30: Failure pattern for Test-9 sandwich specimen from two opposite sides.

2.3.14 Test-10: Static test of sandwich specimen with 25 mm foam core and $[(\pm 45_C)_2,(0_C,0_G)_4,(\pm 45_C)_2]$ face laminate

In order to avoid local buckling of the face sheets observed in the previous tested specimens with 25 mm thickness foam core, new steel plates were manufactured to fit the new specimen dimensions. They were further utilised to support the sandwich faces as shown in Figure 2.31. The strain measurements were monitored as an indicator of uniform load distribution through the faces until a reasonable deviation was observed. The strain distributions were fairly linear through the test until a failure occurred at an average strain level of 5250 μstrain, which corresponds to a load level of 122 kN which is greater than the load approached in the previous two tests for similar configuration specimens, see Figure 2.32. The final failure was characterised by severe brooming at the edges. C-Scan images taken for the specimen damage after the test showed no evidence of damage growth. Although face buckling was avoided using the new setup, a better support method was further sought to induce the face damage propagation without causing failure at the edges.

Figure 2.31: Test setup for a sandwich specimen with 25 mm foam core and $[(\pm 45_C)_2,(0_C,0_G)_4,(\pm 45_C)_2]$ face laminate, Test-10.

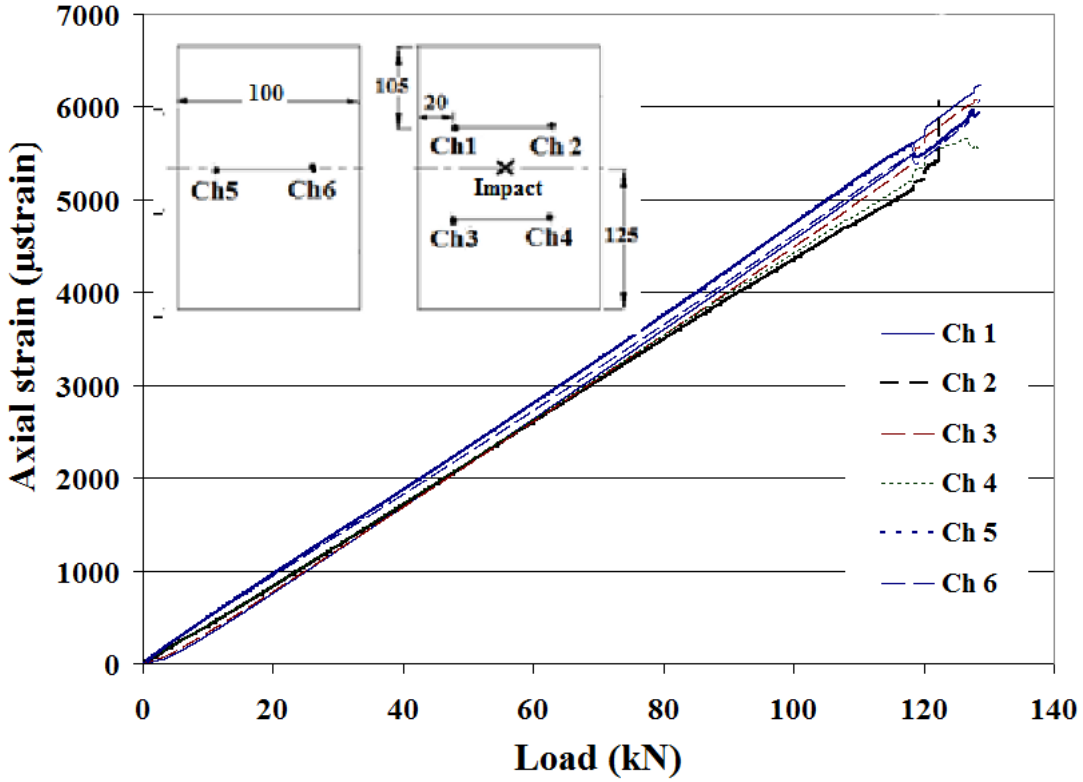

Figure 2.32: Load vs strain for sandwich specimen with $[(\pm 45_C)_2, (0_C, 0_G)_{4S}, (\pm 45_C)_2]$ face laminate, Test-10.

2.3.15 Discussion and conclusions of the preliminary testing programme

An experimental study was carried out on sandwich specimens with two different laminate faces under static and fatigue compression loading. The study aimed to examine the buckling-driven delamination of impact damage sandwich structures. The analytical model assumed uniform compression strain field applied through both the base laminate and thin sub-laminate. The experimental procedures were developed to ensure such condition; at the same time avoiding any other effects which could arise from experiments.

Although the final testing trial showed a maximum average strain of 5250 μstrain was reached before buckling, the face damage for the $[(\pm 45_C)_2,(0_C,0_G)_4,(\pm 45_C)_2]$ laminate seemed not to grow at this strain rather than resulting in crushing of face edges. This suggested that a better method to support the faces against

buckling should have the ability to avoid brooming or crushing of the face ends. At the same time they should allow a uniform applied strain through the faces. For this purpose, the specimens were cut into shorter lengths that allowed enough face support against buckling. The specimens with $[(\pm 45_C)_2,(0_C,0_G)_4,(\pm 45_C)_2]$ face laminates were potted in the epoxy resin specified in Chapter A. The new specimen length was enough to be submersed to the epoxy resin by 40 mm at both sides, and allowed a 100 mm unsupported length for a non-restrained damage propagation in the load direction. The new specimen dimensions were 180×100×29 mm. The face ends were potted in the resin containers shown in Figure 2.33 below. The resin helped to apply uniform axial strain on both faces with minimal use of metallic shims which considerably reduced the setup time of the test experienced in the pilot testing. A gap of 2 mm between the foam end and the resin surface was ensured at each specimen side to avoid any compression of the foam. The epoxy resin was prepared by mixing up equal volumes of the two epoxies. The mix was then poured into one container, filling up to 40 mm depth. The specimen was initially inserted into the filled container then left for 24 hours for the resin to set. The procedure was repeated and the other end was then put in the second resin container. The arrangement was finally left for another 24 hours to set.

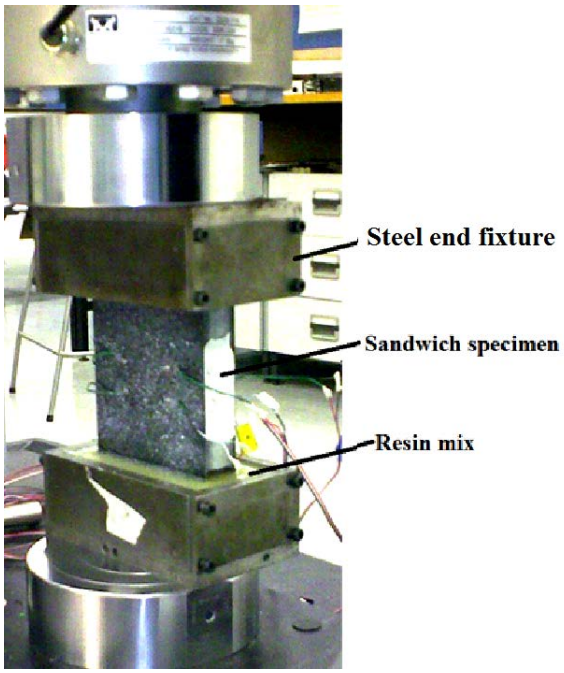

Figure 2.33: Sandwich specimen potted in epoxy resin.

As concluded from testing the specimen with $[(\mp 45_C)_2,(90_C,90_G)_4,(\mp 45_C)_2]$ face laminate, in Test-7, the faces had a lower failure strain that induced damage propagation during the experiment. The new specimens dimensions of 100×100×29 mm were utilised for the rest of the testing programme for this laminate type. The new specimen configuration is shown in Figure 2.34. The foam core length was reduced by 5 mm at each face end to avoid any compression of the foam that may induce excessive shear failure.

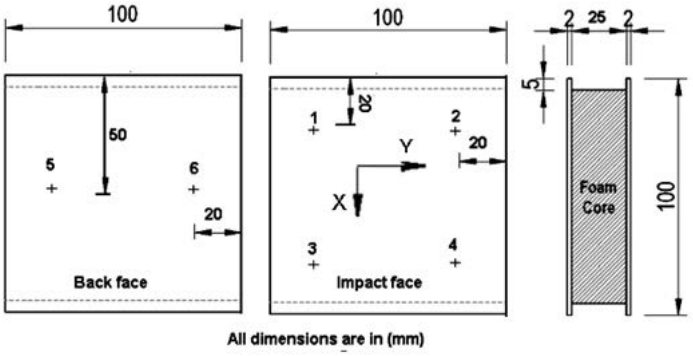

Figure 2.34: Schematic drawing for the sandwich specimen with $[(\mp 45_C)_2,(90_C,90_G)_4,(\mp 45_C)_2]$ face laminate dimensions. The numbered positions show the strain gauges.

The DIC showed a promising in-situ methodology to monitor the buckling behaviour of the specimen. It could also show evidence of any local damage growth under load application. The comparison between the acquired strains from the DIC and the strain gauges showed perfect correlation.

2.4 Experimental results of the main test programme

2.4.1 Specimen details

Sandwich specimens were tested under static and fatigue loading. The core material was 25 mm thick Rohacell Polymethacrylamide Foam (110 kg/m^3). The

face materials were a mixture of unidirectional glass and carbon fibre prepreg with material properties shown in Table 2.4.

Table 2.4: Material properties of Sandwich unidirectional prepreges

Material	E_{11} (GPa)	E_{22} (GPa)	G_{12} (GPa)	ϵ_{12}	G_{IC} (J/m^2)	Cured Ply thickness (mm)
Fibredux 913 GE5 Glass	43.9	15.4	4.29	0.28	225	0.142
Hexply 913C HTA Carbon	135	18.5	4.97	0.29	225	0.134

Both types of specimens had an initial length of 220 mm, width 100mm and thickness 29.35 mm. The specimens were impacted by 8J using an Instron/Dynatup impact machine. They were held by a fixture which has an unsupported window (75×125 mm) directly beneath the impactor, and the impactor head was semi-spherical of 16 mm diameter. The (0°) fibre direction was aligned along the length of the window.

The impact-damaged specimens were scanned by an ultrasonic C-Scan system to visualise the through-thickness damage morphology within the face laminate, see Figure 2.35, before compression testing. The damage shape had two distinctive morphologies; one was of elliptic shape near the impact surface while the other was of circular shape near the foam side.

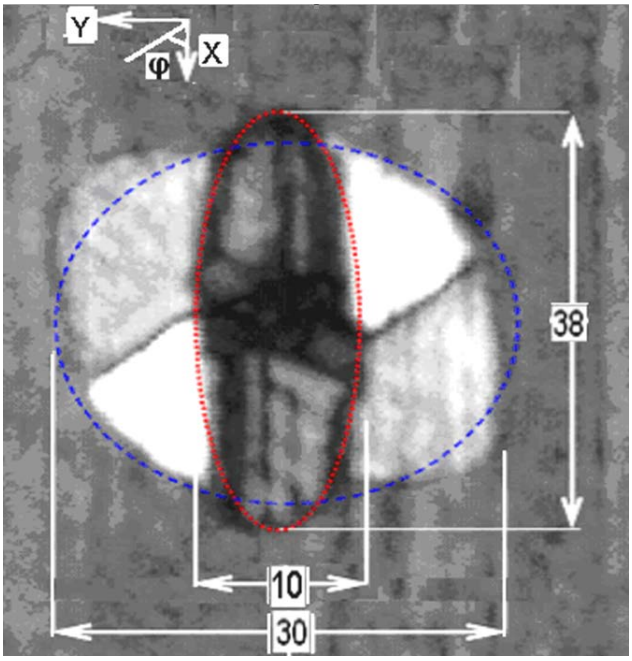

Figure 2.35: C-Scan image of the damage in a $[(\pm 45_C)_2,(0_C,0_G)_4,(\pm 45_C)_2]$ face laminate specimen. (Dimensions are in mm and 0° plies are parallel to the x-axis).

According to the sectioning investigation on a 20 mm presented in Section 2.3.3, it was shown that the elliptic shape appearing in the C-Scan image in Figure 2.35 was related to the damage near the impact face as visualised by the sectioning technique, despite the slight difference in dimensions. While the circular damage was near the back interface with the foam core.

2.4.2 Static Test Results

Static tests were performed on two samples to investigate the influence of impact on the static strength. The first sample was aligned along the loading axis (x-axis) so that it had $[(\mp 45_C)_2,(90_C,90_G)_4,(\mp 45_C)_2]$ face layup while the second was aligned perpendicular to this with $[(\pm 45_C)_2,(0_C,0_G)_4,(\pm 45_C)_2]$ faces. In order to ensure uniform axial loading on both sandwich faces, six strain gauges were attached on the impact and back face for each specimen. Figures 2.34 and 2.36 show gauge lengths and strain gauge positions for both laminates. Gauges 1, 2, 3 and 4 were attached on the impact face while gauges 5 and 6 were on the back face to ensure equal loads were applied on both faces. The widths W for the

$[(\pm 45_C)_2,(0_C,0_G)_4,(\pm 45_C)_2]$ and $[(\mp 45_C)_2,(90_C,90_G)_4,(\mp 45_C)_2]$ laminates were 75 mm and 100 mm respectively. The dotted lines show the resin ends in which the specimens with $[(\pm 45_C)_2,(0_C,0_G)_4,(\pm 45_C)_2]$ face laminate were potted to prevent any brooming at the ends. Potting was not necessary for the other specimen configuration with more compliant faces. In both cases, the foam core length was slightly shortened to ensure the axial loading was only carried by the faces.

In the case of the $[(\mp 45_C)_2,(90_C,90_G)_4,(\mp 45_C)_2]$ specimen, the loading behaviour was linear up to failure at a load level of 65 kN as shown in Figure 2.37.

The DIC system was used to monitor the impacted face deformation and strain under loading. The system consists of two high speed cameras set at equal angles from the specimen axis. The speckle pattern was applied to the specimen face using white paint and the system software from LIMESS uses this speckle pattern to calculate the local deformation, strain and curvature of the loaded face with respect to the initial undeformed state. A sub-laminate within the damaged face buckled away from the foam core (outwards) as the load increased. Figure 2.38 shows out-of-plane displacements of the damage face at different load levels, 50, 55, 56 ,57 and 65 kN.

The out-of-plane displacements were extracted and plotted along two cut sections in Figures 2.39 and 2.40. The results show that a significant buckling displacement occurred above a load level of 50 kN and that it increased as the load increased. They also show that propagation occurred above 55 kN corresponding to an applied nominal strain level of approximately 5820 μstrain. In order to extract the approximate dimensions of the damage upon buckling and propagation, the displacement curves exhibited earlier were vertically separated for clarity as shown in Figures 2.41 and 2.42. The nodes highlighted in both figures were approximately placed at the buckled sub-laminate boundaries. It can be seen from Figures 2.41 and 2.42 that at the start of buckling, the damage had an elliptical base of 18×30 mm dimensions. The major axis of the base was perpendicular to the loading direction.

The maximum out-of-plane displacement was 0.7 mm measured at 65 kN (last image taken before failure) corresponding to a nominal strain level of approximately 6880 μstrain. After the test was performed, a section was cut through the first specimen perpendicular to the load direction (i.e along the x-axis) in order

to visualise the damage propagation. The specimen had through-width separations at the fourth and twelfth ply levels from the impact side i.e. between the $[(\mp 45_C)_2]$ and $[(90_C,90_G)_4]$ layer bands.

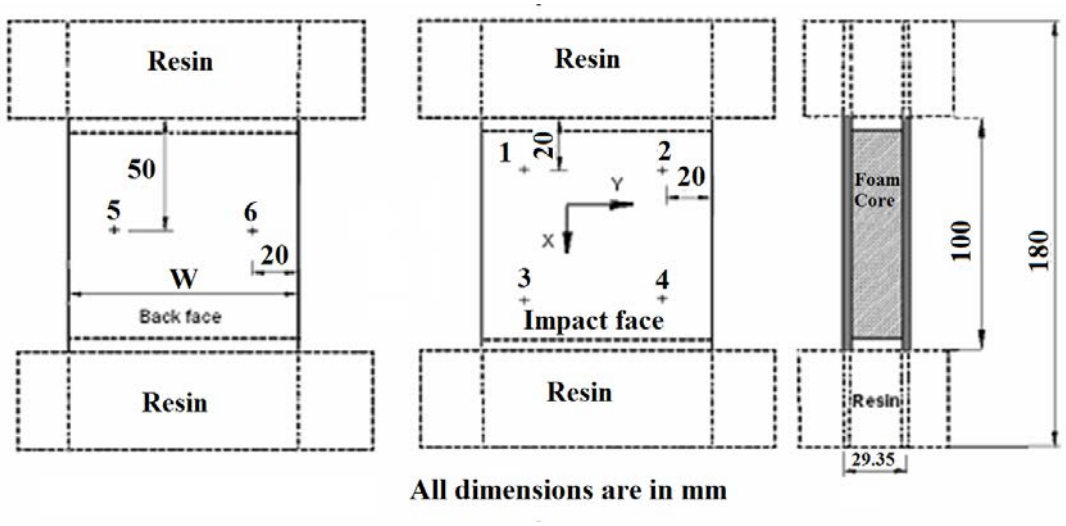

Figure 2.36: Sandwich specimen gauge length dimensions and strain gauge locations. Resin blocks were used for the$[(\pm 45_C)_2,(0_C,0_G)_4,(\pm 45_C)_2]$ face specimens.

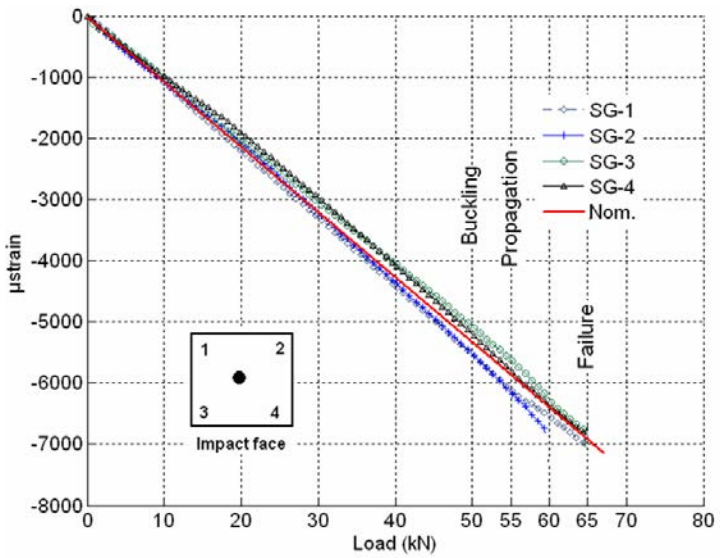

Figure 2.37: Strain measurements for impact face of the specimen with $[(\mp 45_C)_2,(90_C,90_G)_4,(\mp 45_C)_2]$ faces.

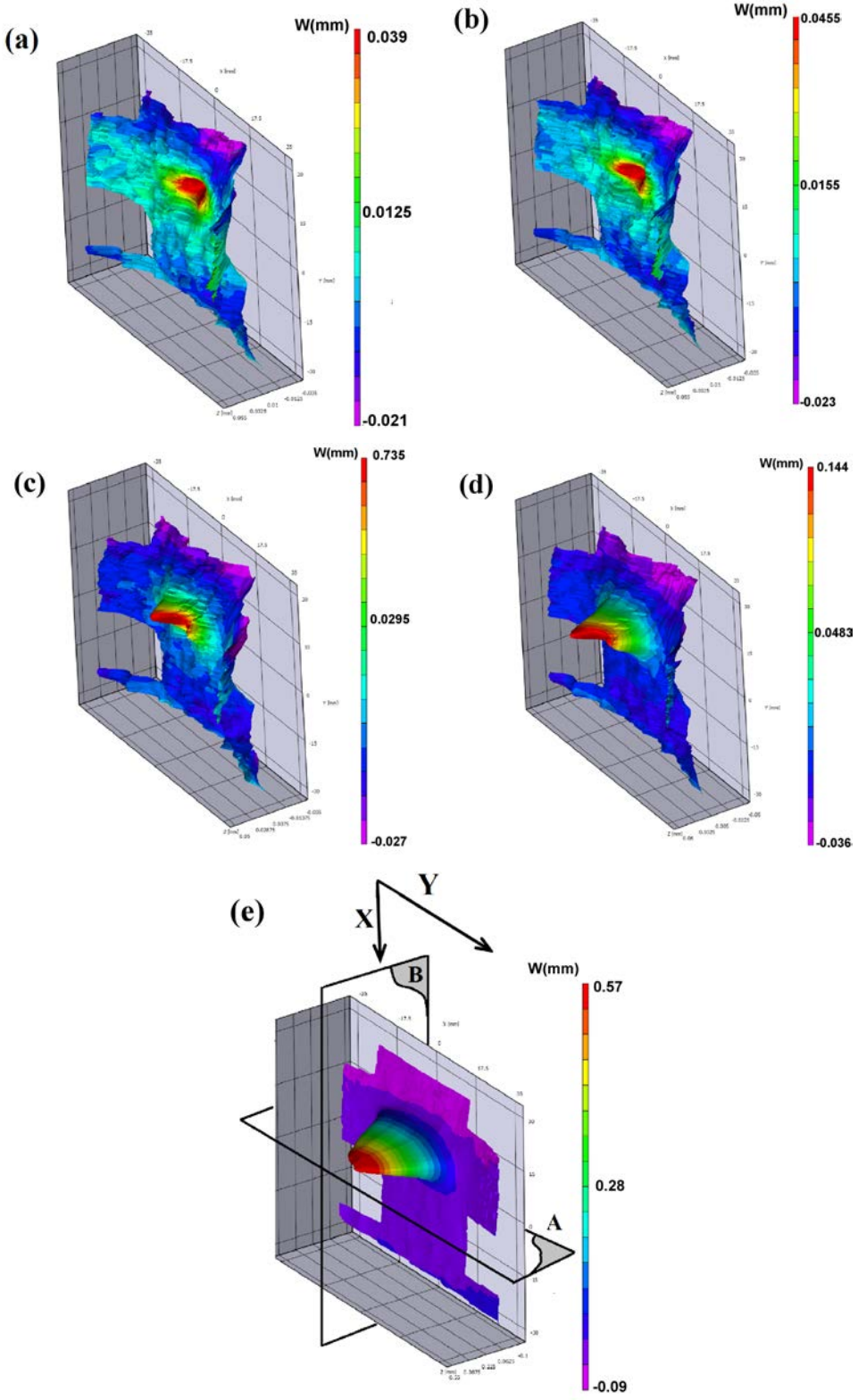

Figure 2.38: Out-of-plane displacements for specimen with $[(\mp 45_C)_2,(90_C,90_G)_4,(\mp 45_C)_2]$ faces recorded at (a) 50 kN, (b) 55 kN, (c) 56 kN, (d) 57 kN and (e) 65 kN.

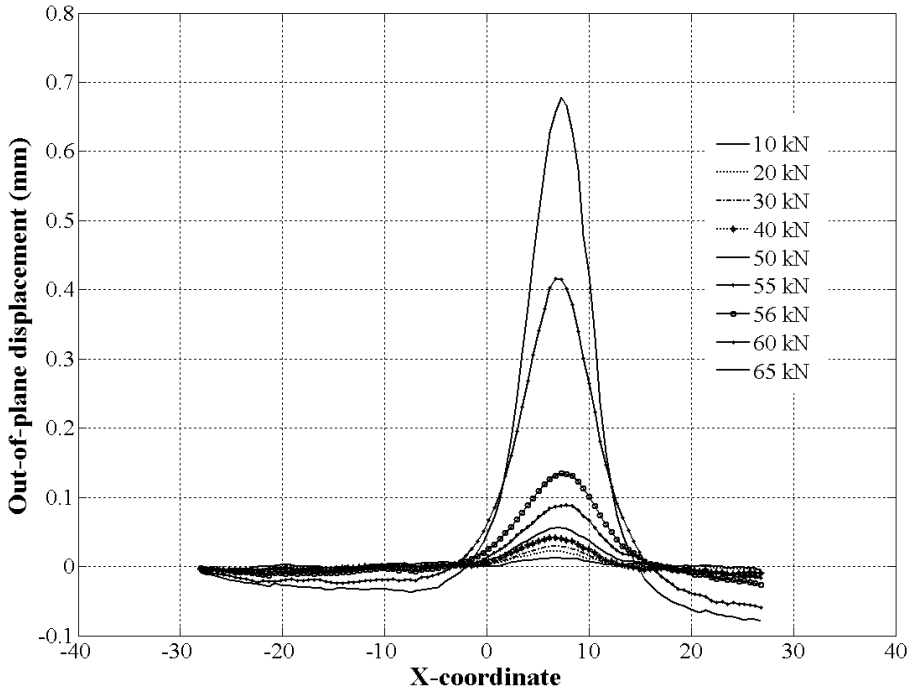

Figure 2.39: Displacement distribution over vertical cut plane (B) in Figure 2.38 at different compression load levels.

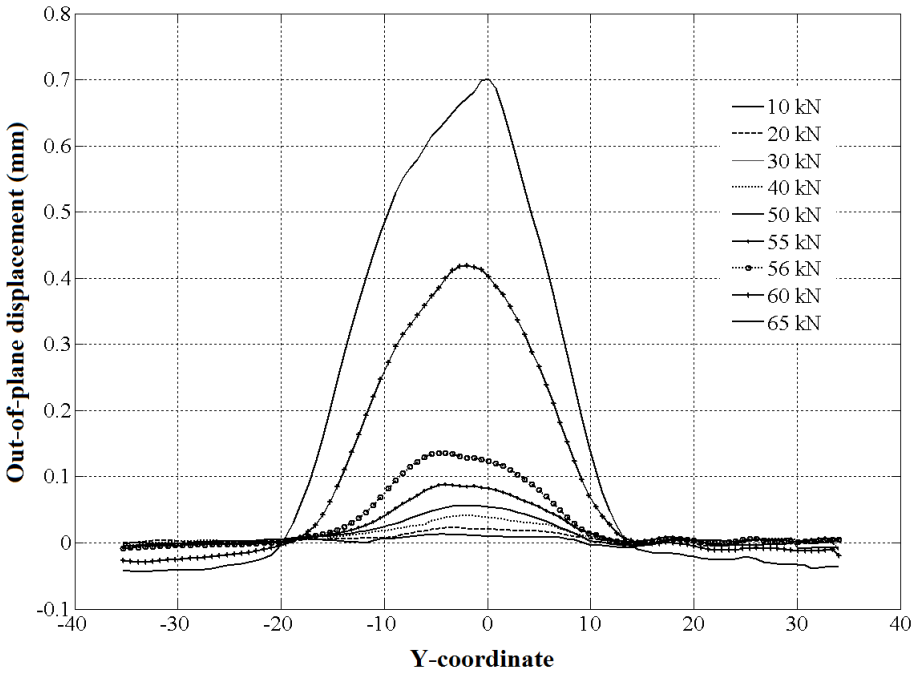

Figure 2.40: Displacement distribution over horizontal cut plane (A) in Figure 2.38 at different compression load levels.

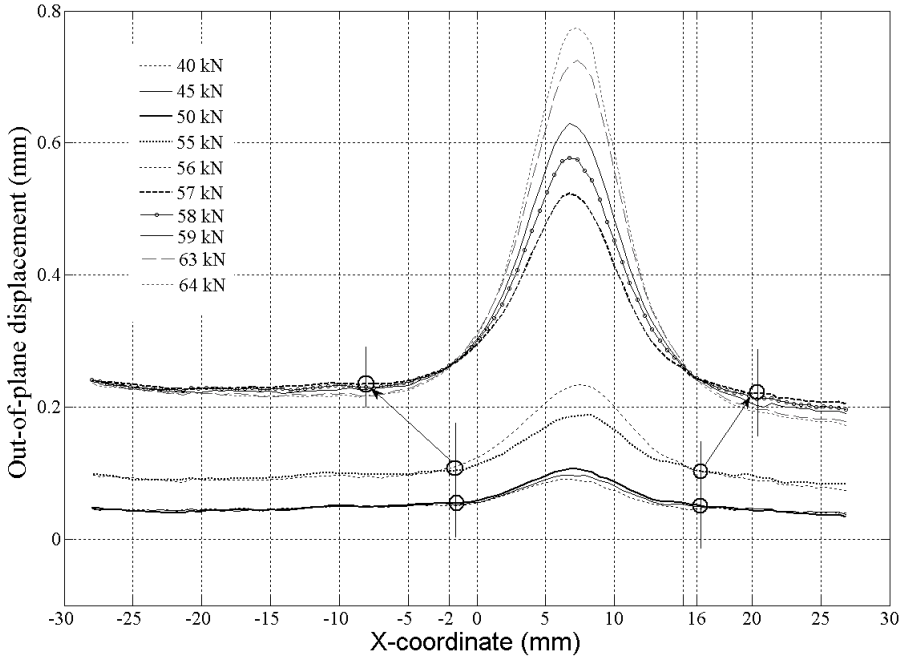

Figure 2.41: Extraction of damage buckling and propagation dimensions for the $[(\mp 45_C)_2,(90_C,90_G)_4,(\mp 45_C)_2]$ specimen in plane (B).

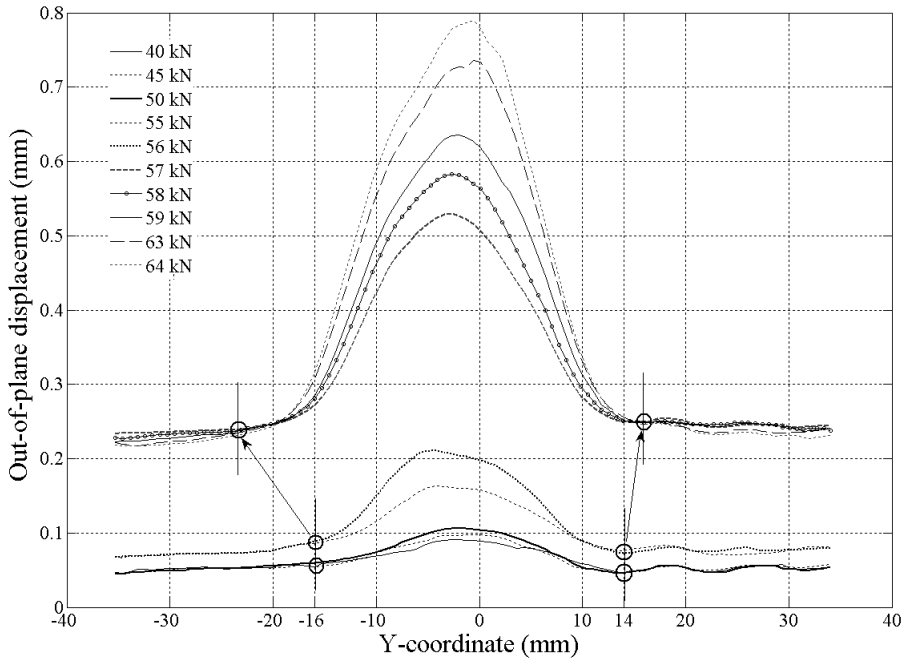

Figure 2.42: Extraction of damage buckling and propagation dimensions for the $[(\mp 45_C)_2,(90_C,90_G)_4,(\mp 45_C)_2]$ specimen in plane (A).

In the case of the specimen with $[(\pm 45_C)_2,(0_C,0_G)_4,(\pm 45_C)_2]$ face laminates, propagation was captured using the DIC to occur at a nominal strain level of 6950 μstrain followed by failure which occurred at 151 kN corresponding to a nominal strain of approximately 7300 μstrain. In contrast to the previous specimen, buckling was observed to occur towards the foam side (inwards). The strain measurements for the test are shown in Figure 2.43 while Figures 2.44, 2.45 and 2.46 show out-of-plane displacement distributions. The displacement distribution had a cone shape with a circular base. The maximum out-of-plane displacement was 1.2 mm with a base diameter of approximately 60 mm and face buckling of the whole specimen was observed after 116 kN. The specimen failure was sudden and cracks appeared on the surface through the whole width. After the test, sectional examination of the laminate showed the laminate separation was dominant between the 4^{th} and the 5^{th} layers.

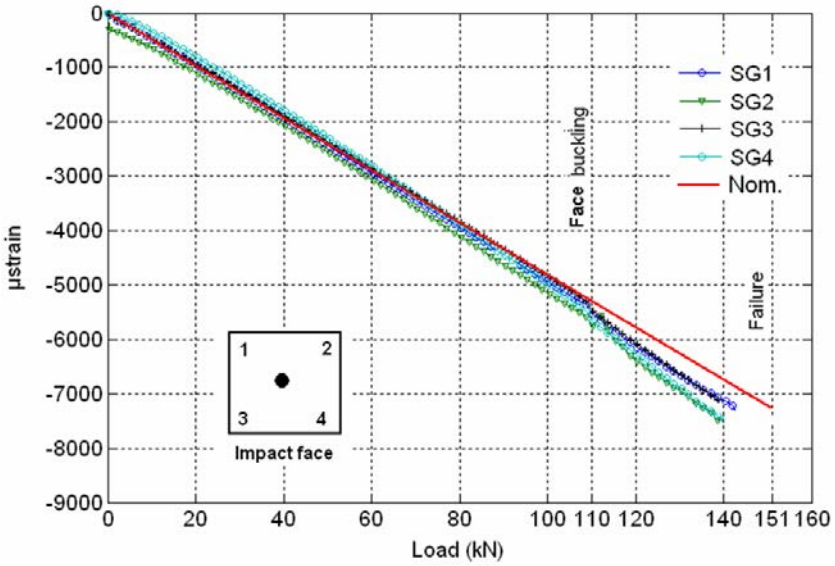

Figure 2.43: Strain measurements for impact face of the specimen with $[(\pm 45_C)_2,(0_C,0_G)_4,(\pm 45_C)_2]$ faces.

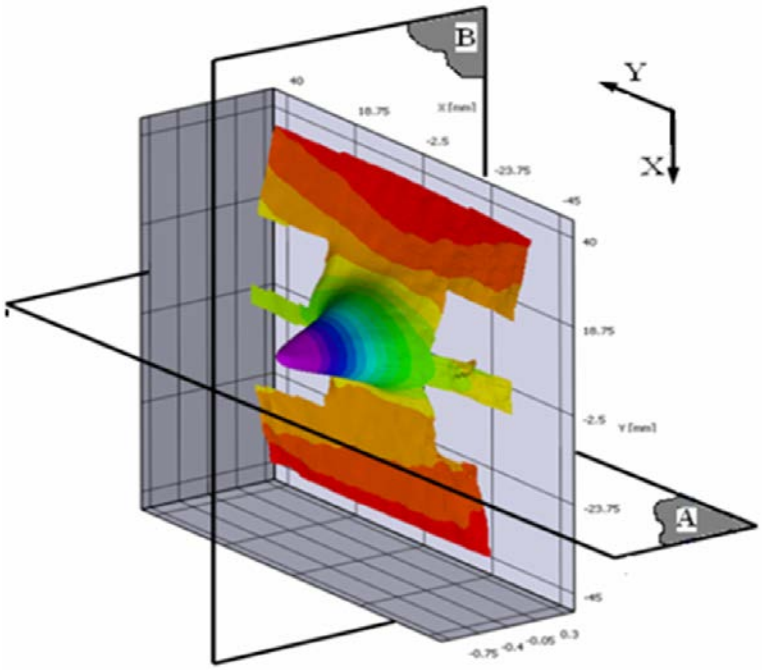

Figure 2.44: Out-of-plane displacements for specimen with [($\pm$ 45$_C$)$_2$,(0$_C$,0$_G$)$_4$,($\pm$ 45$_C$)$_2$] faces at 151 kN.

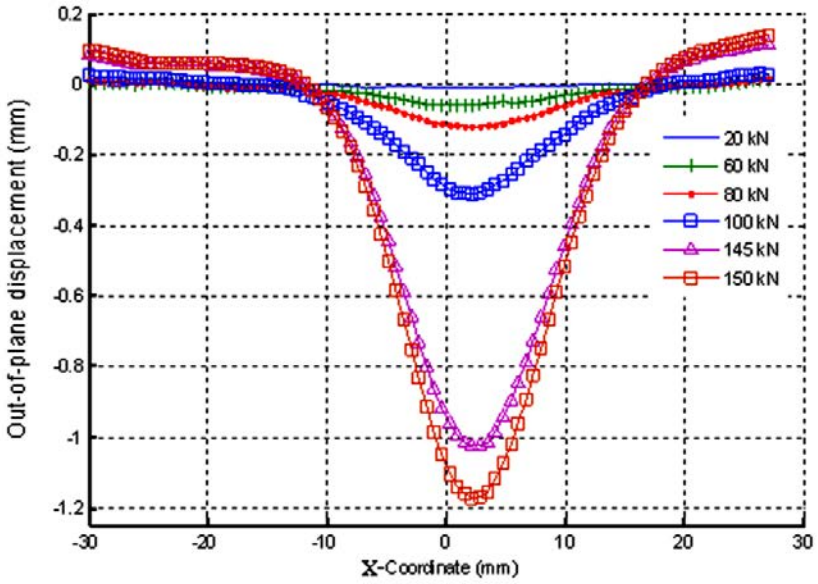

Figure 2.45: Displacement distribution over vertical cut plane (B) in Figure 2.44 at different compression load levels.

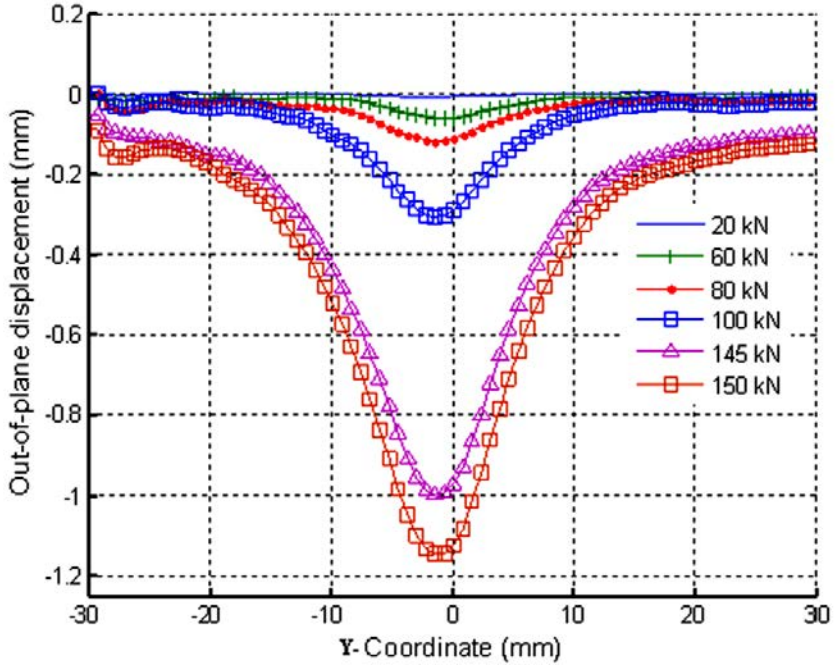

Figure 2.46: Displacement distribution over horizontal cut plane (A) in Figure 2.44 at different compression load levels.

(Note that, with the exceptions of Figures 2.37 and 2.43 and the calculation of R ratio in the fatigue testing, all compressive strains were referred to as positive).

2.4.3 Fatigue Test Results

In order to understand the effect of the difference between delamination modes on fatigue strength, specimens with the impact damage and the two different laminates described above were loaded in compression fatigue. Loading severity, defined as the value of applied strain normalised with respect to nominal static strain at failure, was varied and the number of load cycles required to produce failure of the specimen or significant damage growth within the impact face was recorded . The machine was set to stop when a significant change in face stiffness occurred. For both types of specimens, tests were performed using loading control with a strain ratio R=10, which is defined as the ratio between the minimum and maximum load limits applied within the sinusoidal load cycle. Specimens with $[(\mp 45_C)_2,(90_C,90_G)_4,(\mp 45_C)_2]$ laminates of 100 x 100 mm dimensions were tested using a frequency level of 4 Hz through direct edge loading. The values of loading

severity (ϵ/ϵ_{ult}) used were 0.80, 0.71, 0.58 and 0.54. Outwards delamination buckling on the impact face was observed. Sectioning of the specimens after these tests showed that delamination was at the interface between the ($\pm 45_C$) and (90^o) layer bands, i.e. after the fourth level. Specimens with the [($\pm$ 45_C)$_2$,(0_C,0_G)$_4$,($\pm$ 45_C)$_2$] laminate were initially potted into resin ends to eliminate edge brooming and then tested at a frequency of 3 Hz using loading severity of 0.86, 0.82 and 0.68. Failed specimens had inter-layer separation on the impact face upon failure below the front and rear ($\pm 45_C$) layer bands without any evidence of delamination buckling. This face failure was accompanied by a longitudinal cracking through the foam core.

Figure 2.47 shows the fatigue behaviour for both specimen types. Note that critical growth is defined above. When compared with static strength, the first specimen type showed lower fatigue strength than the second one due to the opening delamination mode. The horizontal dotted line is the predicted fatigue strain limit derived in the following section.

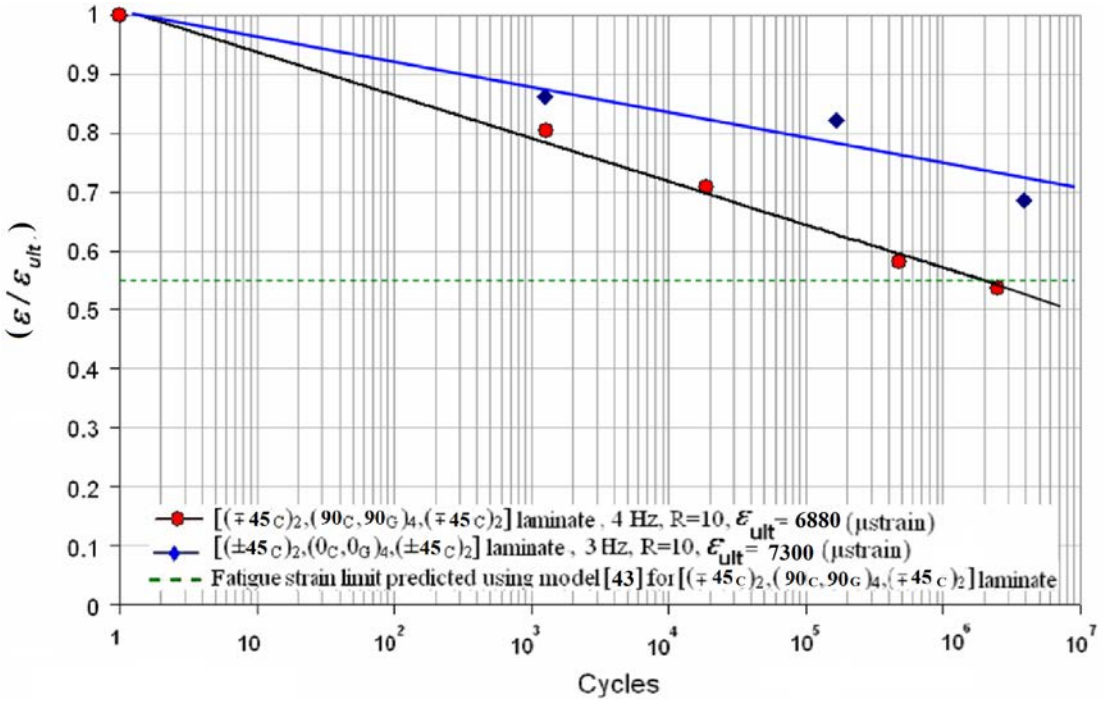

Figure 2.47: Fatigue life plot for sandwich specimens with two different face laminates where ϵ is the maximum applied strain and ϵ_{ult} is the nominal failure strain under static loading.

2.5 Analytical model results

2.5.1 Static model results

The analytical model presented previously assumes that propagation is caused by Mode-I opening of a delamination at a critical interface within the laminate. Hence the model was used to predict the buckling and threshold strain for the face laminate in which such opening occurred. The scanned image showed damage morphology through the face thickness while the sectioning technique showed that the maximum delamination was between the fourth and fifth layers. DIC results taken for the $[(\mp 45_C)_2,(90_C,90_G)_4,(\mp 45_C)_2]$ specimen showed that the buckled damage area had an elliptic base of dimensions a=18 mm and b=30 mm at a load level of 50 kN after which propagation took place. This size of delamination between fourth and fifth layers was used in the model as it resembled the clamped-clamped boundary condition before propagation (see plots in Figures 2.41 and 2.42).

2.5.2 Switching between closing and opening modes

The analytical model assumed opening of the delamination. Since this did not occur for the $[(\pm 45_C)_2,(0_C,0_G)_4,(\pm 45_C)_2]$ laminate specimens, the propagation model was not applicable. However, such conclusion could be reached using the finite strip program, VICONOPT [35]. The two distinctive buckled shapes observed in both experiments were incorporated into VICONOPT: the elliptical buckled area of $a \times b = 18 \times 30$ mm confirmed from DIC results of the $[(\mp 45_C)_2,(90_C,90_G)_4,(\mp 45_C)_2]$ specimen and the buckled circular area of a diameter 60 mm, observed from the$[(\pm 45_C)_2,(0_C,0_G)_4,(\pm 45_C)_2]$ specimen. The VICONOPT was then used to calculate the buckling strains for a clamped elliptical sub-laminate of dimensions $a \times b = 18 \times 30$ mm at the 4^{th} level and a circular sub-laminate of a diameter 60 mm at the 16^{th} level (whole face laminate). The analysis was repeated while noting the axes orientation for both laminates. For the first laminate, $[(\mp 45_C)_2,(90_C,90_G)_4,(\mp 45_C)_2]$, the predicted buckling strains for the elliptical and circular sub-laminates were 5310 and 25,670 μstrain, respectively, which suggested the earlier buckling of the elliptical damage. The

buckling strains calculated for the second specimen, $[(\pm 45_C)_2,(0_C,0_G)_4,(\pm 45_C)_2]$, were 13,300 and 12,350 μstrain for the elliptical and circular sub-laminates, respectively. As a result, the overall face buckling in the latter specimen occurred earlier and no damage opening took place.

2.5.3 Sensitivity analysis of the static model results for $[(\mp 45_C)_2,(90_C,90_G)_4,(\mp 45_C)_2]$ specimen

As the load increased, out-of-plane displacement increased as shown in Figures 2.39 and 2.40. A significant buckling displacement recorded after 50 kN was characterised by a greater level when compared to those recorded at lower levels. Propagation was observed to occur after 55 kN as shown in the plots where the curve nodes positions moved away. Distances between nodes were taken for the 50 kN curve as enclosing dimensions for modelling the damage at buckling. Propagation as shown in Figures 2.41 and 2.42, can be identified by node displacement between load levels 55 and 57 kN. The predicted strain values were compared against nominal strain which was taken as a tangent to the initial linear part of the experimental load-strain curve in Figure 2.39.

In order to investigate the effect of damage dimensions obtained from the DIC plot results, a sensitivity study was performed. The buckling and threshold strain values for a variety of damage dimensions were calculated using the aforementioned analytical methodology. The strain results shown in Table 2.5 show the deviation from nominal buckling and threshold strain values was within 10%. Another significant outcome was that the change in the minor axis dimension, (in the load direction), resulted in a higher strain deviation than the major axis of the elliptical damage.

Table 2.5: Sensitivity analysis of changing damage dimensions on predicted buckling and threshold strains

$a \times b$ (mm)	Buckling strain (10^6)	Error from Nominal	Error from Average	Threshold strain (10^6)	Error from Nominal	Error from Average
18×30	5310	0.47%	-0.75%	6130	5.44%	3.55%
18.5×30	5110	-3.32%	-4.49%	5960	2.51%	0.68%
18×31	5210	-1.43%	-2.62%	6050	4.06%	2.20%
19×30	4925	-6.82%	-7.94%	5800	-0.24%	-2.03%
19×31	4825	-8.71%	-9.81%	5720	-1.62%	-3.38%
18×34	4960	-6.16%	-7.29%	5830	0.28%	-1.52%
Nominal	5285			5820		
Average	5350			5920		

2.5.4 Fatigue model results

Under fatigue loading, the damage was assumed to have grown to fill a circular area of 38 mm diameter. In order to calculate the fatigue threshold strain for a buckled sub-laminate as assumed previously in [43], the damage delamination was modelled as a clamped sub-laminate of 38 mm diameter which encompassed the average damage size obtained from the C-Scan images. The sub-laminate propagation strain was obtained for different levels, presented in Table 2.6. The minimum calculated strain was for the sub-laminate after level four, i.e. after the $[\mp 45_C]_2$ block.

A summary of the analytical results for the specimen configuration with $[(\mp 45_C)_2,(90_C,90_G)_4,(\mp 45_C)_2]$ face laminate under static and fatigue loading is presented in Table 2.7.

Table 2.6: Buckling and threshold strain values for sandwich specimen with $[(\mp 45_C)_2,(90_C,90_G)_4,(\mp 45_C)_2]$ face laminate

Sub-lamiante	Buckling strain (10^6)	Threshold strain (10^6)
$[-45_C/45_C]$	303	5752
$[-45_C/45_C/-45_C]$	1020	4293
$[-45_C/45_C/-45_C/45_C]$	1950	3813
$[-45_C/45_C/-45_C/45_C/90_C]$	3380	4517
$[-45_C/45_C/-45_C/45_C/90_C/90_G]$	4360	5189

Table 2.7: Summary of analytical and experimental results for buckling and threshold strains for specimens with $[(\mp 45_C)_2,(90_C,90_G)_4,(\mp 45_C)_2]$ face laminates, assuming that the delamination is after the fourth ply.

	Sub-laminate dimensions axb (mm)	Analytical		Experimental	
		ϵ^c (10^6)	ϵ_{th} (10^6)	ϵ^c (10^6)	ϵ_{prop} (10^6)
Static	18x30	5310	6130	5050	5820
Fatigue	38x38	1950	3800	-	3700

2.6 Discussion of results

In order to determine the damage morphology through the face thickness, C-Scan and sectioning techniques were used. The C-Scan image for the damage showed that the nearest delamination to the face had an elliptical shape with dimensions 38×10 mm, while a deeper delamination existed near the back surface with a circular shape of a 30 mm diameter, see Figure 2.35. By sectioning an impact-damaged sample, the elliptical delamination was shown to exist between the fourth and fifth layers from the impact side.

From the static test results for the sample with the $[(\mp 45_C)_2,(90_C,90_G)_4,(\mp 45_C)_2]$ laminate, the buckling mode of the damaged area on the impact surface was of elliptic shape similar to the C-Scan image shown in Figure 2.35. The out-of-plane displacement graphs in Figures 2.41 and 2.42 showed the buckled sub-laminate had an elliptical shape with base dimensions of a=18 mm and b=30 mm. These dimensions were incorporated in the model to predict the propagation strain under static load. The sectioning technique and post-test failure pattern suggested that the maximum damage existed after level four, i.e. after$[(\mp 45_C)_2]$. Propagation, which was predicted to occur at 6130 μstrain, was observed in the experiment at a nominal strain of approximately 5820 μstrain. Failure did not occur until a nominal strain of 6880 μstrain. This additional capacity is thought to be due to the high residual bending stiffness of the sandwich system following propagation.

The specimen with $[(\pm 45_C)_2,(0_C,0_G)_4,(\pm 45_C)_2]$ faces had a high value of Poisson's ratio (ν_{xy}=0.6) for the full laminate. This resulted in a lower value of lateral compressive stress induced in the delaminated $[(\pm 45_C)_2]$ sub-laminate which delayed buckling compared with the equivalent stress for the $[(\mp 45_C)_2,(90_C,90_G)_4,(\mp 45_C)_2]$ laminate. (Note that the laminate Poisson's ratio of the latter is 0.3). Although the experimental end conditions for the $[(\mp 45_C)_2,(90_C,90_G)_4,(\mp 45_C)_2]$ specimens and the $[(\pm 45_C)_2,(0_C,0_G)_4,(\pm 45_C)_2]$ specimens were different, failure occurred at the centrally located site of impact damage, where the measured strains were consistent with the assumption of uni-axial load.

Hunt et al [30] showed that the occurrence of an opening or closing mode depends on the position and length of the delamination; long, near surface delaminations are more likely to produce an opening mode because local sub-laminate buckle occurs before overall buckling of the full structure. Their model assumed that the laminates were made of isotropic material and that delaminations were full width. The present study showed that a delamination depth to total face thickness ratio of 0.246 in the $[(\mp 45_C)_2,(90_C,90_G)_4,(\mp 45_C)_2]$ laminate resulted in an opening mode, while the same ratio in the $[(\pm 45_C)_2,(0_C,0_G)_4,(\pm 45_C)_2]$ laminate produced a closing mode. Here the difference in modes was due to the difference in (1) the alignment of the elliptical delamination (2) the material anisotropy, and (3) the face-foam interaction, which affects the boundary conditions of the damaged area. Although the level of nominal strain at which failure occurred was similar for both

laminates, the failure load of the stiff $[(\pm 45_C)_2,(0_C,0_G)_4,(\pm 45_C)_2]$ laminate was 132% higher than that of the compliant $[(\mp 45_C)_2,(90_C,90_G)_4,(\mp 45_C)_2]$ laminate.

Due to the small number of specimens used in the fatigue tests, single specimens were tested at different severity levels. This led to an approximate fatigue trend for each specimen type.

In the case of the $[(\mp 45_C)_2,(90_C,90_G)_4,(\mp 45_C)_2]$ face specimen, the damage grew in dimensions (a) and (b) in a stable manner similar to that observed from the DIC images in the static test results presented in Figures 2.39 and 2.40. The damage initially had an elliptical shape until it grew longitudinally towards a circular shape before extending in the transverse direction. Similar combinations of growth direction were observed by Rhead et al [43] for artificially embedded delaminations within highly anisotropic thin sub-laminates. C-scan images were taken for a specimen tested in fatigue at 0.82 severity. A continuous through-width damage of 28 mm length (in loading direction) was observed after the test. Assuming the damage had fixed dimensions of a=28 and a=38 mm in the load direction, the graph shown in Figure 2.48 was created using Equation 2.1 for the variable transverse dimension, b. From the analysis, it was shown that as dimension, b, approached 50 mm for a=38 mm or 80 mm for a=28 mm, the fatigue propagation threshold strain approached a minimum value of 3670 μstrain. This value corresponds to the strain level for slightly above $2.5\text{x}10^6$ cycles of fatigue life in the experimental fatigue life plot shown in Figure 2.47.

The reason that the analytical method did not appear to predict the precise value of the experimental fatigue limit for infinite life may have been because the experiments were conducted under load control whereas the analysis assumed displacement (strain) control. The reduced flexibility of the damaged face, caused by delamination propagation, resulted in an increased experimental value of applied strain. Hence the values of experimental strain recorded in Figure 2.47 calculated from the nominal experimental strain, were actually higher as the test progressed.

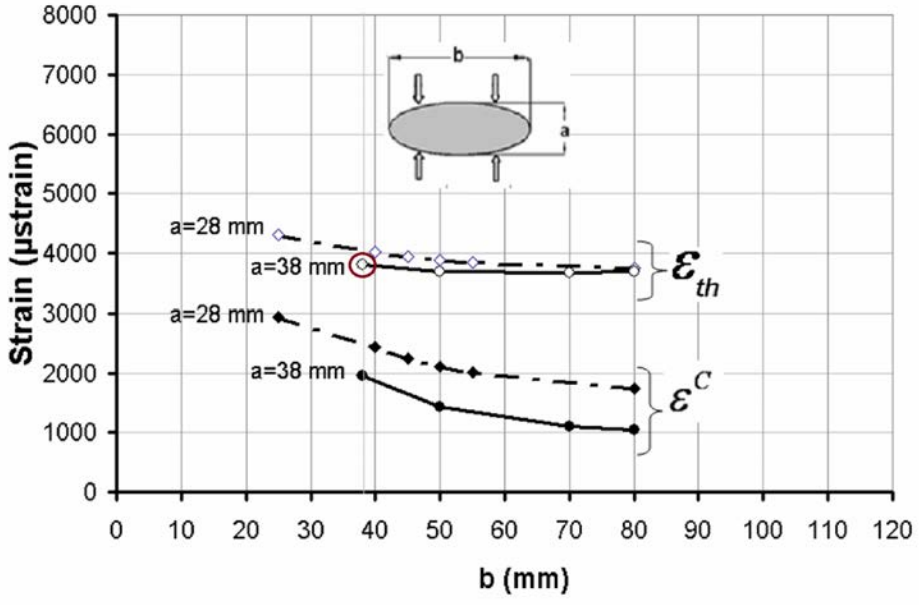

Figure 2.48: Effect of damage dimensions on theoretical buckling and threshold strains, ϵ_C and ϵ_{th}, respectively) for a delamination placed between the 4^{th} and 5^{th} layers in the $[(\mp 45_C)_2,(90_C,90_G)_4,(\mp 45_C)_2]$ laminate. The encircled point is the solution for a $\phi 38$ damage,represented the dotted line in Figure 2.47.

2.7 Conclusions

Sandwich specimens with $[(\mp 45_C)_2,(90_C,90_G)_4,(\mp 45_C)_2]$ and $[(\pm 45_C)_2,(0_C,0_G)_4,(\pm 45_C)_2]$ face laminates were tested under compression after impact. Failure was shown to be dependent on the orientation of fibres at the centre of the laminates. When these fibres were at 90° to the loading direction, an opening of the delamination was observed giving rise to bucked-driven propagation which has been successfully predicted using a semi-analytical technique. However, when these fibres were parallel to the direction of load, the opening of delamination was not observed and the fibres buckled into a core depression arising from the impact. It has been shown that the propensity of this latter mode can be predicted because of the high initial buckling strain of the thin sub-laminate produced by the delamination compared with full face laminate buckling. Experiments showed that when loading was normalised with respect to static strength, specimens with Mode-I opening had a lower fatigue life compared to those with Mode-II closing behaviour.

An analytical model [43] gave an approximate prediction of the fatigue strain limit for Mode-I opening when the delamination area was assumed to be a circle encompassing the whole damage on the impact face. The model also indicated the direction of growth beyond this circle. Modelling the damage using the dimensions of the buckled shape taken from the DIC images gave a value close to static test results for the Mode-I opening case.

Chapter 3

Buckling of Through-width Delaminated Beams in Bending

3.1 Summary and objectives

The work presented in this Chapter investigates the behaviour of through-width delaminated beams under pure compression. A pre-developed low dimensional analytical model was presented to predict snap-buckling and post-buckling behaviour of the thin sub-laminate in the composite beam. The model examined the bifurcation behaviour of the sub-laminate, which switched from a closing to an opening mode. A further fracture model was incorporated to predict the moment level at which propagation of such opened sub-laminate would take place. Static tests were performed on three sets of specimens to validate the combined analytical technique. Finally, fatigue tests on similar specimen sets were performed to study the influence of an opening buckling mode of the sub-laminate on the fatigue behaviour of the whole laminate.

3.2 Analytical Modelling

3.2.1 Snap-buckling and post-buckling analysis

A pre-developed mathematical model by Hunt et al [30], which employed a four degree of freedom Rayleigh-Ritz approach to analyse the nonlinear buckling and post-buckling of a delaminated composite strut under axial compression, was adapted in order to account for the application of pure bending.

The model assumed that the strut is isotropic and the undelaminated end laminates are ignored in the prediction of the snap-buckling (or opening) moment, while the delaminated parts are modelled with bending and in-plane stiffness EI and EA, respectively. Further assumptions were that the rotation of the undelaminated region and each delaminated part were the same at their intersection, and that there was no friction between laminates at the interface. The end rotation provided one of the degrees of freedom Q_2. A second degree of freedom represented the end-shortening of the sub-laminates over the delaminated region, (Δ). A further degree of freedom was used to describe the buckling displacement of the delaminated parts, Q_1. Figure 3.1 shows a schematic of the delaminated beam and the applied moment. Note that positive Q_1 and negative Q_2 produce opening.

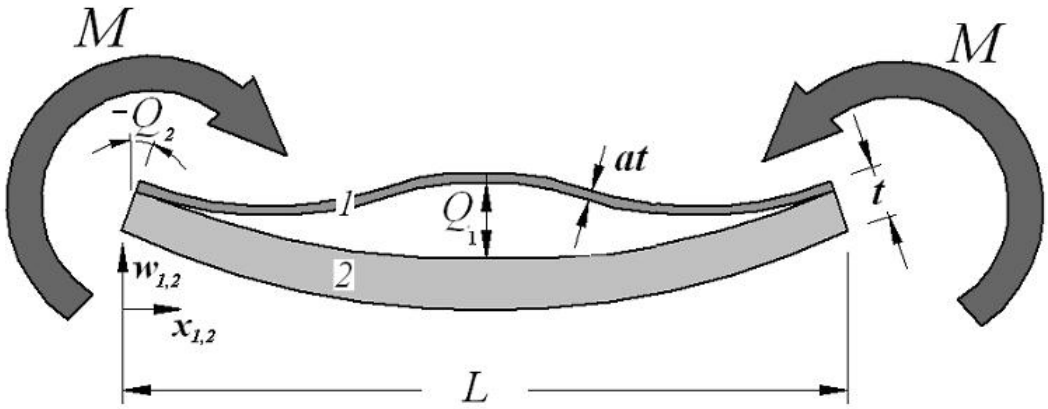

Figure 3.1: Delaminated beam coordinates and variables

The displacement functions for the delaminated and base parts are given as follows:

$$w_1(x) = Q_1 sin^2\big(\frac{\pi x_1}{L}\big) + Q_2\, x_1\big(\frac{L - x_1}{L}\big) \tag{3.2.1}$$

$$w_2(x) = Q_2 x_2\big(\frac{L - x_2}{L}\big) \tag{3.2.2}$$

where x_1 and x_2 are measured from the geometrical mid-plane of the beam at the left end.

The effect of initial imperfection was introduced to the model to investigate how the inclusion of an idealised PTFE layer, used to create a delamination within the composite layers, would affect snap-buckling. The imperfection was assumed to have a sine-squared function of the form:

$$w_0(x) = Q_0 sin^2\big(\frac{\pi x_1}{L}\big) \tag{3.2.3}$$

In order to calculate the stretching energies in the system, the axial end shortening for the thin and thick sub-laminates is as follows:

$$\delta_1 = \Delta - \frac{1}{2}\int_0^L \left(\frac{d(w_1 - w_o)}{dx_1}\right)^2 dx_1 - Q_2(1-a)t \tag{3.2.4}$$

$$\delta_2 = \Delta - \frac{1}{2}\int_0^L \left(\frac{dw_2}{dx_2}\right)^2 dx_2 + Q_2 at \tag{3.2.5}$$

The strain energy of the system is obtained in terms of bending (U_B) and stretching (U_S) energy as follows:

$$U_B = \frac{EI_1}{2}\int_0^L \left(\frac{d^2(w_1 - w_o)}{dx_1^2}\right)^2 dx_1 + \frac{EI_2}{2}\int_0^L \left(\frac{d^2 w_2}{dx_2^2}\right)^2 dx_2 \tag{3.2.6}$$

$$U_S = \frac{t}{2L}\big(Ea\delta_1^2 + E(1-a)\delta_2^2\big) \tag{3.2.7}$$

where the bending rigidities (EI_1) and (EI_2) are obtained at the neutral axes of laminates 1 and 2, respectively.

The total energy of the system is:

$$V = U_B + U_S - 2MQ_2 \tag{3.2.8}$$

Substituting the displacement equations into the former equation leads to a potential function including three degrees of freedom in addition to the loading moment, $V(Q_1, Q_2, \Delta, M)$. By solving the partial equilibrium equation with respect to Δ, i.e:

$$\partial V(Q_1, Q_2, \Delta, M)/\partial\Delta = 0 \tag{3.2.9}$$

Substituting the resulting term into V, we obtain a two-degree of freedom term $V^{'}(Q_1, Q_2, M)$, i.e: $\partial V/\partial Q_1 = 0$, $\partial V/\partial Q_2 = 0$.

Solving the adapted system of equations as reported previously by Hunt et al [30], the buckling displacement and rotation (Q_1, Q_2) were evaluated as functions of applied bending moment(M). The derivation process was carried out with a mathematical manipulation software.

3.2.2 Propagation prediction using thin film analysis

Various models to predict propagation of delaminated composite plates under compressive loads were studied and introduced as previously discussed in the literature section in Chapter 1. An initial approximation to investigate the delaminated composite beams under bending is to incorporate a delamination model for compression in order to calculate the strain energy release rate of the system.

As the sub-laminate length to thickness ratio was approximately equal to 80 for the example considered here, it can be approximated as an Euler strut which is compressed under bending. For predicting the propagation moment of the sub-laminate, a one dimensional mode by Chai et al [21] was initially used. This model assumed that the ends of the thin sub-laminate do not rotate and calculates the critical strain energy release rate for the propagation of a compressed sub-laminate as follows:

$$G = \frac{Eat}{2}(\varepsilon - \varepsilon^C)(\varepsilon + 3\varepsilon^C) \tag{3.2.10}$$

Furthermore, the model ignores any bending energy that is released from the thick lower sub-laminate or from the end laminates. The buckling strain ε^C for the sub-laminate was calculated using the Euler formula for buckling of a strut fixed at each end, Equation (3.2.11), while the applied strain ε was formulated using Equation (3.2.12).

$$\varepsilon^C = \frac{\pi^2 a^2 t^2}{3L^2} \tag{3.2.11}$$

$$\varepsilon = \frac{6M(1-a)}{Et^2} \tag{3.2.12}$$

3.2.3 Mixed mode propagation

Existence of curvature at the sub-laminate ends indicates that both Mode-I and Mode-II effects should be taken into consideration. A selection of the analytical method was based on separating both fracture modes, i.e. obtaining strain energy release rates G_I and G_{II} separately. For this purpose, the fracture model by Hutchinson & Suo [77] was used to calculate both release rates based on the stress intensities factors K_I and K_{II} near the delamination tips. Their approach assumed homogeneous isotropic layers and that the force and moment components are per unit width. Assuming a plane stress state at a plane tangent to the interface, the stress intensity factors can be obtained as follows:

$$K_I = \frac{P}{\sqrt{2atU}} cos\omega + \frac{M^*}{\sqrt{2a^3t^3V}} sin(\omega + \gamma) \tag{3.2.13}$$

$$K_{II} = \frac{P}{\sqrt{2atU}} sin\omega - \frac{M^*}{\sqrt{2a^3t^3V}} cos(\omega + \gamma) \tag{3.2.14}$$

where P and M^* are the linear combinations of the applied force P_1 and moments M and M_1 at the delamination edges shown in Figure 3.2.

$$P = P_1 - \frac{CM}{at} \quad , \qquad M^* = M_1 - C^* M$$

The geometric factors were obtained in terms of the thickness ratio as follows:

$$C = \frac{6/\eta}{(1/\eta + 1)^3} \quad , \quad C^* = \frac{1}{(1/\eta + 1)^3} \quad , \quad \eta = \frac{a}{1-a}$$

$$\frac{1}{U} = 1 + 4\eta + 6\eta^2 + 3\eta^3 \quad , \quad \frac{1}{V} = 12(1 + \eta^3)$$

γ and ω were obtained through:

$$\omega = 52.1^o - 3^o\eta \qquad , \qquad sin\gamma = 6\eta^2(1+\eta)\sqrt{UV}$$

From which the following strain energy release rates could be obtained:

$$G_I = \frac{K_I^2}{2E} \qquad , \qquad G_{II} = \frac{K_{II}^2}{2E} \tag{3.2.15}$$

where E is the effective longitudinal modulus for the layer material. The division by two in Equation (3.2.15) is added assuming that propagation occurs at both delamination fronts simultaneously as a result of symmetry.

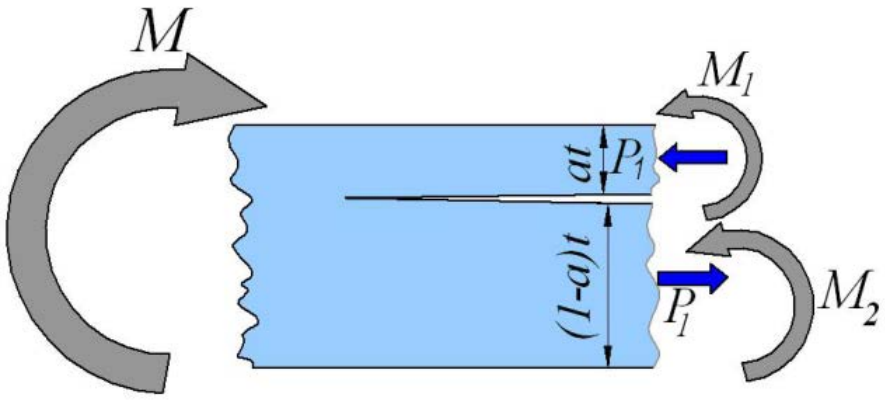

Figure 3.2: Force and moment components at delamination edges.

In order to obtain the strain energy release rates in Equation (3.2.14) the force P_1 and moment M_1 at the left end of the thin sub-laminate are required. The thin sub-laminate is assumed to only carry the critical buckling load, i.e:

$$P_1 = \varepsilon^C Eat \tag{3.2.16}$$

Where ε^C is derived using Equation (3.2.11). M_1 is calculated from the curvature of the thin sub-laminate, obtained by evaluating the second derivative of Equation (3.2.1) at $x_1 = 0$.

3.3 Experimental Setup and Procedures

Static tests were performed on three sets of specimens made of two different materials to understand their buckling and propagation behaviour.

The first specimen type was made of 16 layers of unidirectional T800/M21, $[0]_{16}$ carbon fibre prepreg while the second and the third were made of IM7/8552 carbon prepreg with laminate definitions of $[0]_{32}$ and $[45/90/-45/0]_{4S}$, respectively. In order to form a through width delamination, a polytetrafluoroethylene, PTFE, layer of 0.02 mm thickness was placed at the mid length of each plate at a depth of thickness ratio $a = 0.125$, i.e. between the second and third ply for the M21/T800 plate and between the fourth and fifth ply for the IM7/8552 plates, respectively. The delamination length in all arrangements was 40 mm. The plates were laid up, bagged and then cured inside an autoclave according to the manufacturer curing cycle prescribed in Chapter A.

The cured plates were cut into specimens with dimensions of ($220 \times W \times t$ mm) where W and t are given in Tables 3.1, 3.2 and 3.3. In order to measure the strain at which buckling of the sub-laminate would occur, each specimen had two strain gauges positioned on the centre of the top and bottom surfaces. An INSTRON-1332 servo-hydraulic machine with a 10 kN load cell was used for loading application. The strain gauges and the loading channel from the servo-hydraulic machine were connected to a SPIDER-8 data acquisition system which was attached to a PC. The specimens were then loaded through the four point bending fixture shown in Figure 3.3 under displacement control. The fixture

had movable supports to adjust the inter distances and a pivot to ensure a uniform bending load application. The centre of the delamination was positioned at middle span of both upper and lower parts.

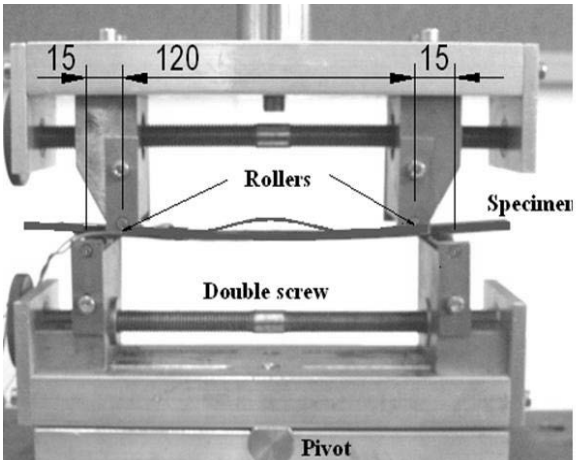

Figure 3.3: Four point bending test fixture showing specimen with delamination open (loaded above snap-buckling moment). Dimensions in mm.

3.4 Experimental Results

3.4.1 Pilot testing

An initial study was performed to select suitable delamination length, depth and testing parameters, such as test speed and roller spans. For this purpose, through-width delaminated specimens were manufactured from unidirectional T800/M21-0_{16} carbon prepreg material. Delamination lengths were 20 mm and 40 mm situated at thickness ratios of $a = 1/8$ and $a = 3/16$. Tests were performed under displacement control using four point bending. It was shown that changing the testing speed between 50 N/min and 100 N/min had no influence on the final failure moment. Another observation was that the buckling of the sub-laminate only occurred in those specimens with 40 mm length situated at a thickness ratio of $a = 1/8$. Such specimen configuration was decided to be used for the testing programme in this Chapter.

3.4.2 Main test programme, snap-buckling moment results

Strain gauges of 350 Ω and a gauge factor 2.1 were used to observe the change in strain value on top and bottom surfaces of the specimen, where a sudden change of the top strain gauge indicated the buckling of the sub-laminate. The slopes of both gauge lines were shown to be linear up to snap-buckling. The change in strain was found to suddenly occur in some specimens and with small smooth transition in others through a range of the applied moment.
Snap-buckling moment values were obtained from acquired data corresponding to the change of strain on the outer surface of the sub-laminate. Figure 3.4 shows strain versus applied moment plot for Test 2, 3 and 4 mentioned in Table 3.1. The snap-buckling moment for the rest of all specimen sets was obtained through the comparison of load-vs-time and strain-vs-time data, due to the fact that it was not possible to acquire the load feed-back signal through the data acquisition system (SPIDER-8). The last three T800/M21 specimens were initially tested statically up to a moment level below failure to investigate their snap-buckling moment, then they were further tested in fatigue loading as discussed in the following sub-section. Tables 3.1, 3.2 and 3.3 show snap buckling moment values for different tested specimens manufactured from the two materials. In Table 3.1, it was shown that the moment values for the snap-buckling had an average value of 270 Nm/m for T800/M21 specimens, while one test showed a higher moment value of 706 Nm/m with a corresponding bigger drop in applied load (presented in Table 3.1). Table 3.2 presents an average snap buckling moment of 223 Nm/m for IM7/8552 specimens. The IM7/8552 $[45/90/-45/0]_{4s}$ specimens did not show any snap-buckling as opening occurred as soon as the load was applied. The sub-laminate buckling mode in all specimen sets tended to have a form of a clamped-clamped buckling mode supported by the curved base laminate.

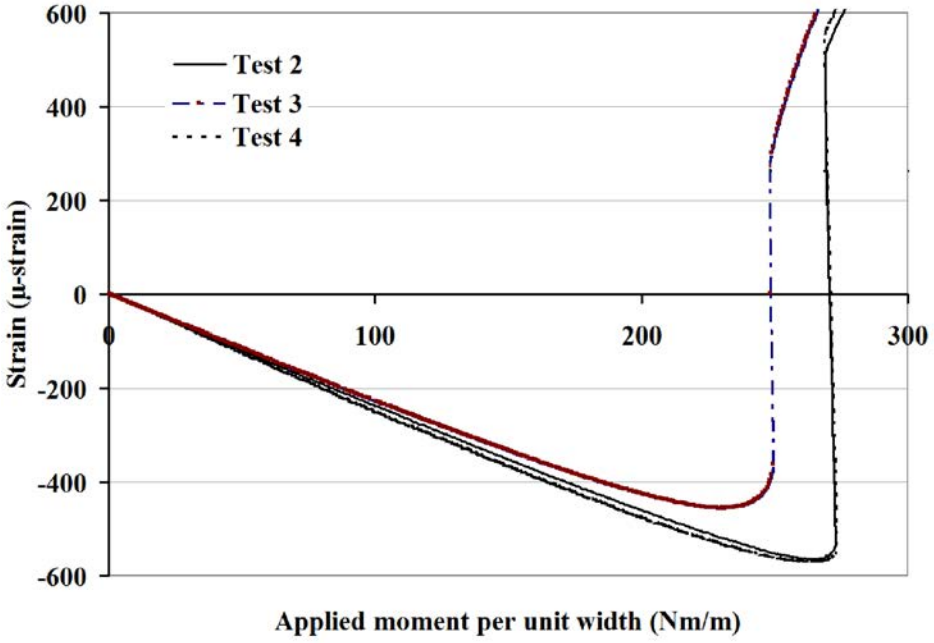

Figure 3.4: Applied Moment versus strain measured at the upper surface centred on the delamination position for T800/M21 specimen

3.4.3 Propagation moment results

In order to predict the propagation of delaminated beams under bending, the specimens were tested under static loading using displacement control until reaching failure. It was shown in all tested specimens that whilst increasing the load, the strain gauges failed to give any reading above a strain level of about 6000 μstrain. Hence, in order to observe the moment value at which propagation occurred, the load versus cross-head displacement measurements were recorded for all specimen sets. Figures 3.5, 3.6 and 3.7 show plots for T800/M21-$[0]_{16}$, IM7/8552-$[0]_{32}$ and IM7/8552-$[45/90/-45/0]_{4s}$ specimens, respectively. Propagation occurred as displacement increased at a constant load. Simultaneous delamination growth at both ends was observed during this region until the specimen reached its full failure. The propagation moment values for the three specimens sets are shown in Tables 3.1, 3.2 and 3.3. The average propagation moment values were 2725 Nm/m, 2268 Nm/m and 1629 Nm/m for T800/M21, IM7/8552 $[0]_{32}$ and IM7/8552 $[45/90/-45/0]_{4s}$ specimens, respectively. From the plots, it is shown that propagation occurred in a step-wise manner in the T800/M21 material while it suddenly occurred in both IM7/8552-$[0]_{16}$ material sets. It was

observed that during testing of the quasi-isotropic, $[45/90/-45/0]_{4s}$ specimen set, the thin sub-laminate was twist-opened at the two sides of the delamination whilst the actuator displacement was applied resulting in a skewed delamination front at both ends. This was due to the bending-twist coupling of the quasi-isotropic sub-laminate, $[45/90/-45/0]_{4s}$.

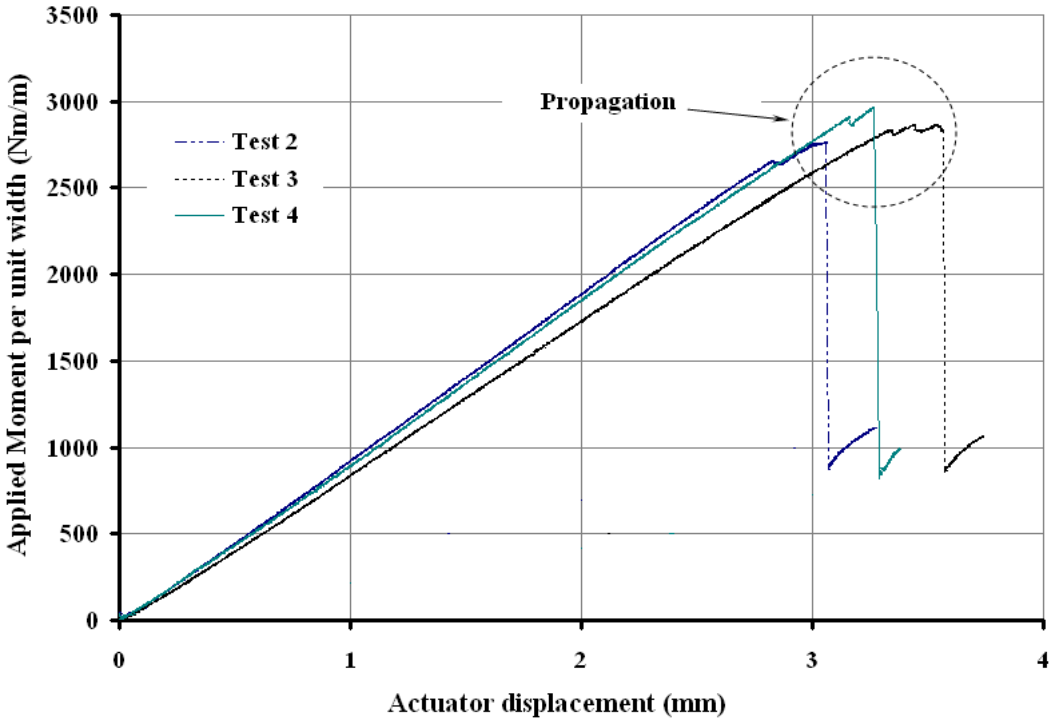

Figure 3.5: Applied Moment versus actuator displacement for T800/M21 $[0]_{16}$ specimen

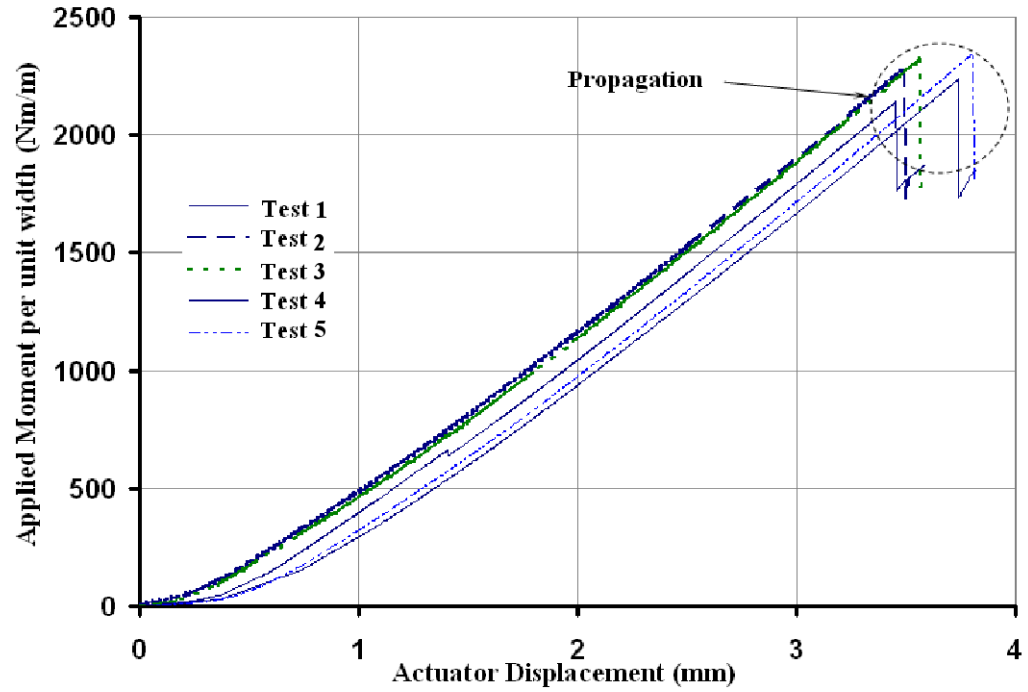

Figure 3.6: Applied Moment versus actuator displacement for IM7/8552 $[0]_{32}$ specimen

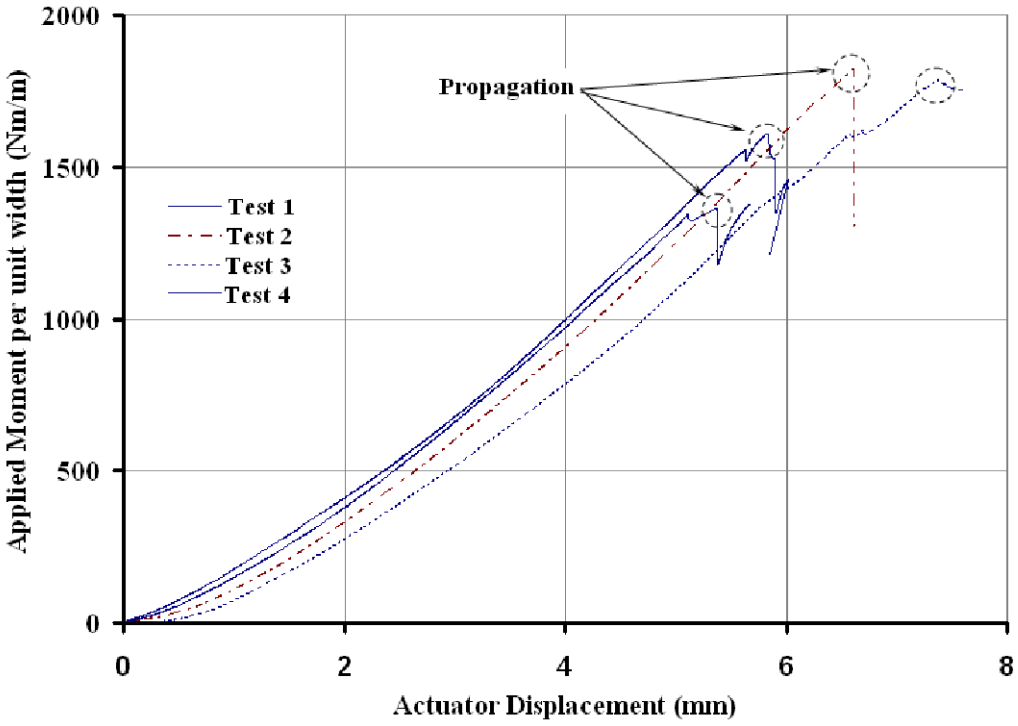

Figure 3.7: Applied Moment versus actuator displacement for IM7/8552 $[45/90/-45/0]_{4S}$ specimen

Table 3.1: Test results for T800/M21 $[0]_{16}$ specimens

Test No.	Width W(mm)	thickness t(mm)	Snap-buckling moment(Nm/m)	Propagation moment(Nm/m)
1	8.38	4.22	706	2779
2	8.41	4.31	273	2645
3	8.14	4.17	249	2824
4	9.15	4.22	273	2573
5	10.98	4.27	267	2675
6	10.78	4.30	320	2853
7	10.95	4.24	298	-
8	10.94	4.33	261	-
9	11.00	4.22	221	-
Avg.	10.27	4.25	270	2725
C.V.%	1	1	12	4

Table 3.2: Test results for IM7/8552 $[0]_{32}$ specimens

Test No.	Width W(mm)	thickness t(mm)	Snap-buckling moment (Nm/m)	Propagation moment (Nm/m)
1	10.34	3.97	221	2238
2	10.18	3.99	287	2291
3	10.25	3.97	283	2321
4	10.24	3.96	184	2141
5	10.20	3.95	142	2347
Avg.	10.27	3.97	223	2268
C.V.%	1	1	28	4

Table 3.3: Test results for IM7/8552 $[45/90/-45/0]_{4s}$ specimens

Test No.	Width W(mm)	thickness t(mm)	Snap-buckling moment (Nm/m)	Propagation moment (Nm/m)
1	9.95	4.04	-	1355
2	10.35	4.01	-	1825
3	10.40	4.00	-	1771
4	10.35	4.02	-	1565
Avg.	10.26	4.02	-	1629
C.V.%	2	0.4	-	13

3.4.4 Fatigue test results

In order to identify the effect of opened delaminations on the fatigue life of composite beams, a series of fatigue tests were performed under four point bending on through-width delamination specimens. A varying pure bending moment was applied while monitoring the growth of the through-width opened delamination. The loading moment was applied so that the thin sub-laminate was kept opened under compression throughout the fatigue cycle. The loading ratio, R, is defined as the ratio between the maximum to minimum applied moment within the cycle. All tests were performed using a loading ratio $R = 10$ and a test frequency of 4 Hz. The severity is calculated as the ratio between the maximum applied moment during the cycle to the average propagation moment from the static tests for both material specimens. Specimens were tested under load control. The loading severity ranged from 0.85 to 0.17 so that a part of the loading cycle always passed through the average critical snap-buckling moment value observed in static tests. The tested specimens had similar dimensions to those tested under static loading with their sides marked with 1 mm gratings around the delamination ends in order to monitor the delamination extension during testing. They were loaded by the four point bend fixture shown in Figure 3.3. The tests were stopped after 10^6 cycles or if specimen failure occurred. For each loading severity, a number of specimens was used to establish the delamination extension curves. For all specimens, the applied moment was normalised by the width of the specimen. During each test, the machine was stopped in order to measure the delamination extension on the grated sides of the specimen. Figures 3.8, 3.9 and 3.10 represent the delamination extension versus number of cycles for different severities of load applied to the three sets of specimens made from the two materials. A high scatter in delamination extension values was observed during high loading severities for the T800/M21 unidirectional plates and the IM7/8552 laminates configurations. The delamination growth decreased with the severity level until reaching a threshold growth at a severity level of 0.1725 and 0.175 after 10^6 cycles for the T800/M21 and IM7/8552 unidirectional configurations, respectively. While fatigue testing of the IM7/8552 $[45/90/-45/0]_{4s}$ specimens showed the threshold was below a severity level equal to 0.3.

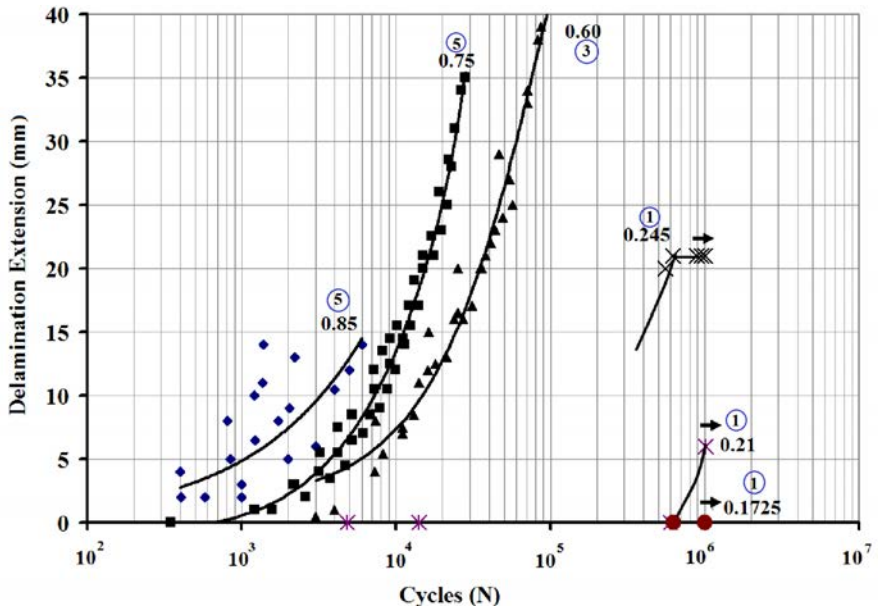

Figure 3.8: Delamination extension versus number of cycles for T800/M21 $[0]_{16}$ specimens at a range of severities. (Note, severity level of 1.0 indicates maximum value of moment =2725 Nm/m. The number of specimens used to establish each load severity curve is encircled)

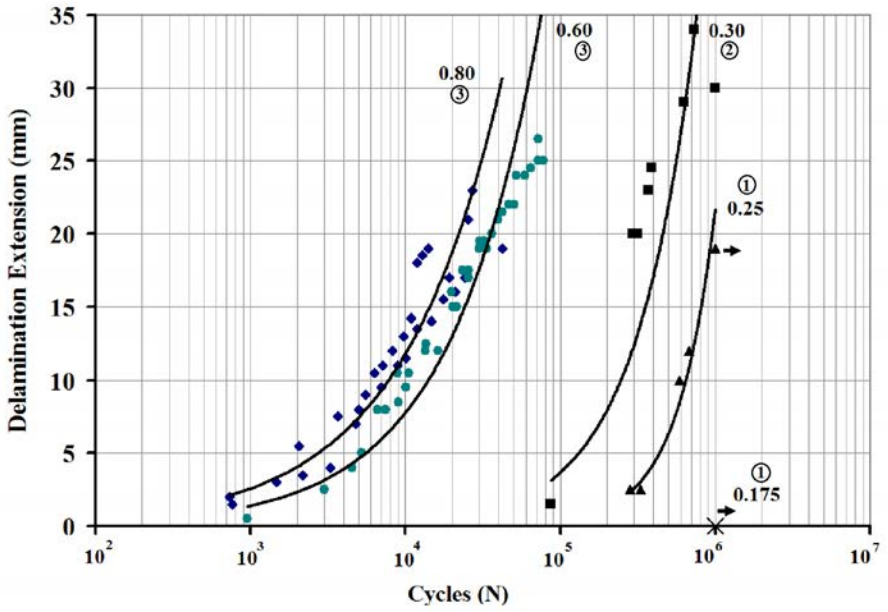

Figure 3.9: Delamination extension versus number of cycles for IM7/8552 specimens at a range of severities. (Note, severity level of 1.0 indicates maximum value of moment =2268 Nm/m. The number of specimens used to establish each load severity curve is encircled.)

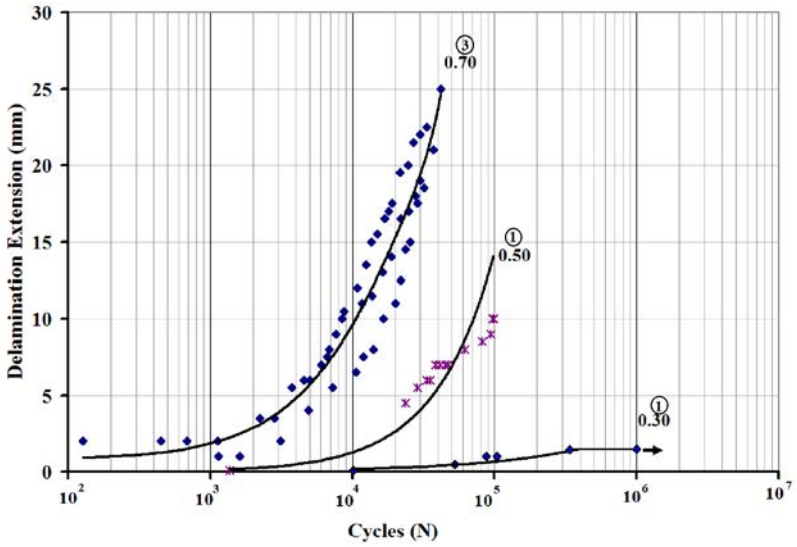

Figure 3.10: Delamination extension versus number of cycles for IM7/8552 $[45/90/-45/0]_{4S}$ specimens at a range of severities. (Note, severity level of 1.0 indicates maximum value of moment =1629 Nm/m. The number of specimens used to establish each load severity curve is encircled.)

3.4.4.1 Effect of delamination opening on fatigue crack extension

A comparative experimental study was performed to investigate the effect of the buckled layer opening on the crack growth behaviour of the through-width delaminated specimens at a low severity level. In order to do that, the out-of-plane displacement was measured for one T800/M21 specimen under static and fatigue loading. It was initially tested under static loading up to a moment level of 470 Nm/m. The opening displacement was then monitored throughout a fatigue cycle at a severity level of 0.1725, i.e. between 47 and 470 Nm/m. Such loading cycle passed through the snap-buckling level, 270 Nm/m recorded in static tests. The maximum displacement measured through the fatigue cycle was compared to the displacement acquired under static loading and the delamination was found to almost exhibit a closing mode through the whole loading cycle.

3.4.5 Fractography Analysis

Amongst the different failure mechanisms in tough epoxy composites, delamination failure is mostly characterised by resin failure. According the ESM images, the corresponding mode and cause of failure could be identified for such materials. Three distinct modes of failures are of concern, Mode-I (peel), Mode-II (shear) and Mode-III (tear). While the third one is not of a major significance in structural damage investigation, the first two modes exist either isolated or in a combined form (mixed mode). Mode-I and Mode-II failures could be observed in resin areas or through fibre-rich regions. From the failure pattern, the corresponding mode of failure could be concluded [85]. For tough resin systems, Mode-I failure (peel mode) is generally observed as a failure in the resin rich areas. The tensile loading energy applied to the system transforms initial small discontinuities within the resin into irregular escalating voids which finally results in an irregular texture, known as "Matrix Cleavage", through the resin. Another characterising failure observation for Mode-I is fibre bridging, i.e. separation of fibres from the interface layer. Fibre bridging may be an evidence of moisture or manufacturing defects. Mode-II failure is characterised by shear cusps, which are small tilted protrusions in the resin tracks with arc-shaped tips. The formation of cusps is responsible for the higher toughness value for Mode-II than Mode-I. The direction of the cusps tilting angles with respect to third layer plane can be used to deduce the direction of crack growth. The characterising fracture images for mixed mode failure is a combination of the aforementioned pure Mode-I and Mode-II fracture patterns, according to the percentage of the loading of each mode [85].

In order to investigate the different fracture modes associated with bending of the tested delaminated specimens in this study, the fracture surfaces resulted by the delamination extension were scanned using an ESM technique. The fracture morphology would be then compared with a similar fracture surfaces taken from a failed DCB specimen. The latter was thought to have a pure Mode-I (peel) fractured surface. The sixth specimen mentioned in Table 3.1 was chosen to be scanned following failure under static test. The surface of the thin sub-laminate was cut from one side and then separated from the specimen. The cut surface and the thin sub-laminate were then cleaned using a gauze-sponge swab slightly-impregnated by a solvent to remove any debris or grease. Such contamination might decrease the resolution of the obtained ESM scan images.

The images in Figures 3.11 and 3.12 show ESM scans of two specimens made of the T800/M21 material system. Images in Figures 3.11-a and 3.11-b are for a specimen tested in pure Mode-I conditions using the Double Cantilever Beam (DCB) test, according to ASTM D-5528 [86]. The images show the damage propagated in the resin rich areas and as the distance from the crack edges increases, the proportion of resin damage decreases and the damage was dominated by fibre bridging [85]. Figures 3.12-a and 3.12-b show images obtained for one of the through-width centred-delamination specimens tested under four point bending as described above. Such loading allowed the top delaminated layer to buckle and then to propagate as the load advanced. The image in Figure 3.12-a shows that the damage was dominated by the shear cusps which characterise the Mode-II failure [85]. The cusps were distributed within the resin area with valleys perpendicular to the fibre direction. Figure 3.12-b, taken around 20 mm away from the delamination front, shows that the proportion of fractured zones is similar to that near the delamination front. This suggests that the propagation is still dominated by Mode-II fracture even away from the delamination front due to the large contact area at this front.

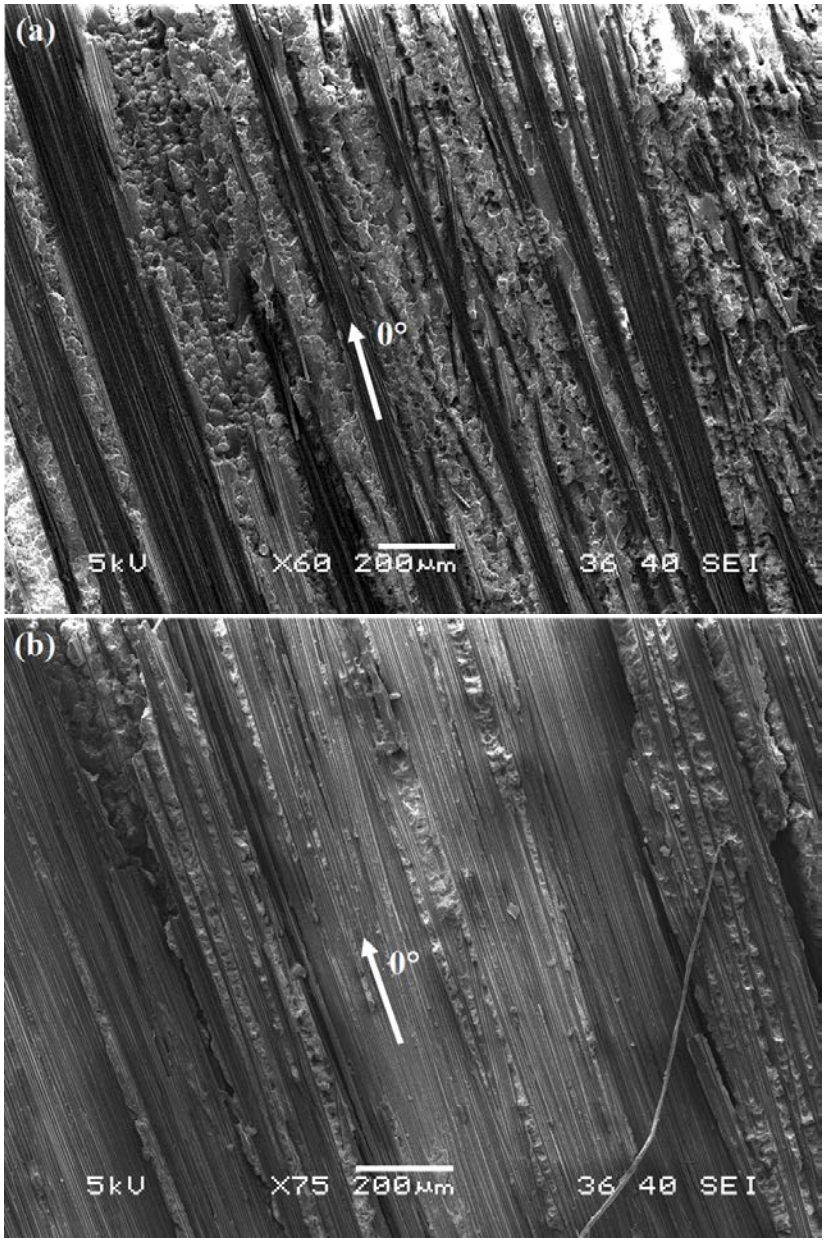

Figure 3.11: ESM images for a DCB test specimen, T800/M21 material. a) Near delamination front. b) 20 mm away from delamination front. In both cases, the fibre direction is shown

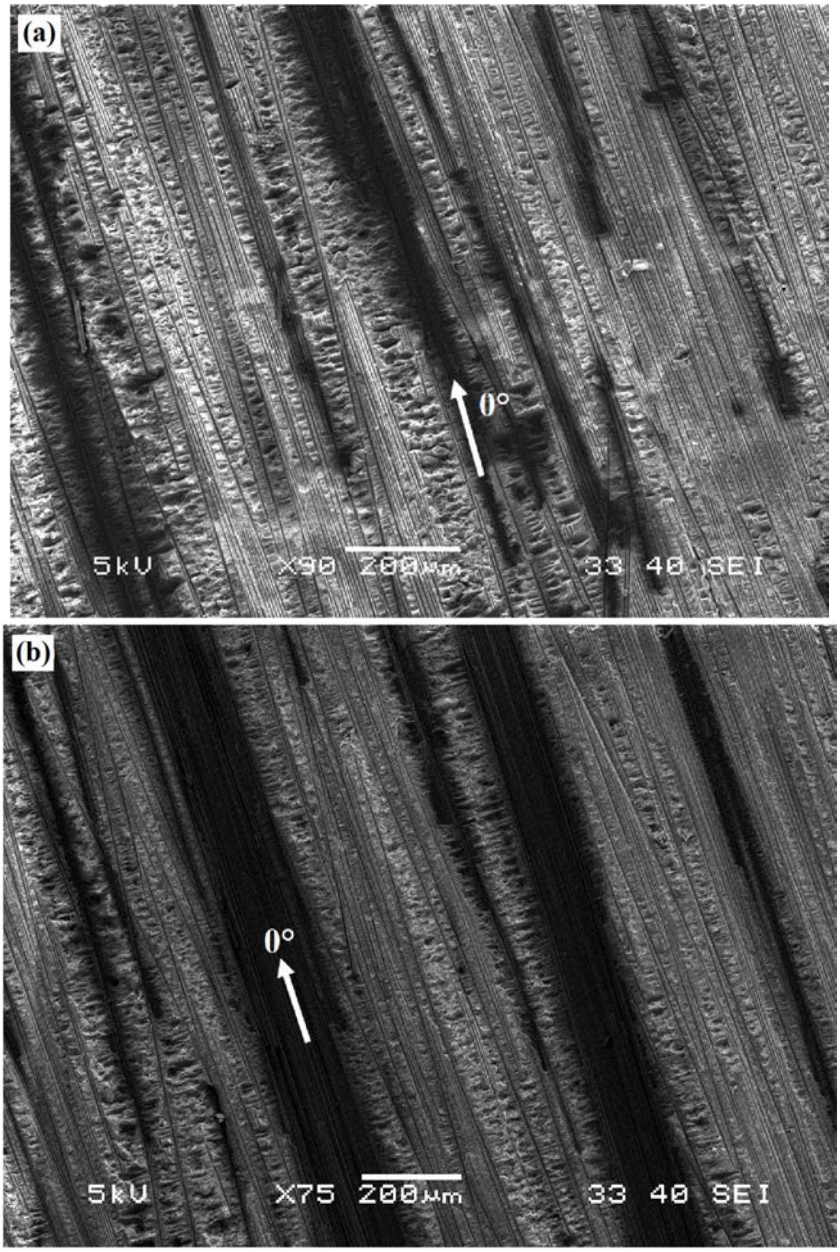

Figure 3.12: ESM images for a four-point bending delaminated specimen, T800/M21 material. a) Near delamination front b)20 mm away from delamination front. In both cases, the fibre direction is shown

3.5 Analytical model results

The model was verified through three steps: first to check the snap-buckling moment level, second to check the kinematics during the post-buckling process and the last step was to check the propagation moment values. The experimental results obtained in the previous section were employed in the model verification process. The mechanical properties for the material systems are included in Table 3.4. The cured ply thickness values shown in the table are obtained by dividing the average cured thickness of the whole laminate by number of layers. The model was used to predict the snap-buckling moment for the three delaminated beam configurations.

Table 3.4: Mechanical properties used in the model for the T800/M21 and IM7/8552 specimen sets

Material	E_{11} (GPa)	G_{IC} (J/m^2)	G_{IIC} (J/m^2)	Cured Ply thickness (mm)
T800/M21-$[0]_{16}$	139	550	1400	0.260
IM7/8552-$[0]_{32}$	161	210	1000	0.123
IM7/8552-$[45/90/-45/0]_{4s}$	161	210	1000	0.126

The solution of the differential equation (3.2.9) resulted in three real roots and two imaginary ones. The real roots for both Q_1 and Q_2 were plotted versus applied moment for the three sets of specimens as shown in Figures 3.13 - 3.18. According to the system of coordinates in Figure 3.1, a negative value of Q_1 corresponds to an infeasible solution, physically explained as both laminates pass through each other. Whilst the branches in the feasible side of Q_1 are for the stable and unstable behaviour of the thin sub-laminate buckling, see Figures 3.13, 3.15 and 3.17. Such bifurcation behaviour is a characteristic of buckled struts with an initial imperfection and results in two feasible solutions. The unstable branch is physically described as a state of the sub-laminate to have a small opening displacement from which the strut is more likely to snap towards the stable state. The corresponding solutions of Q_2 for the three sets of specimens are plotted in the right-hand graphs in Figures 3.14, 3.16 and 3.18, respectively.

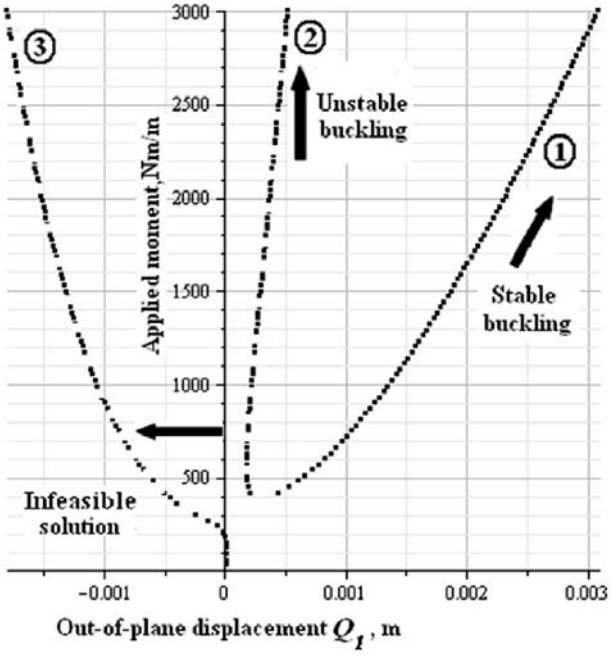

Figure 3.13: Analytical displacement Q_1 against applied moment per unit width M for a T800/M21 $[0]_{16}$ configuration. The circled numbers identify 1) Stable 2) Unstable 3) Infeasible solutions.

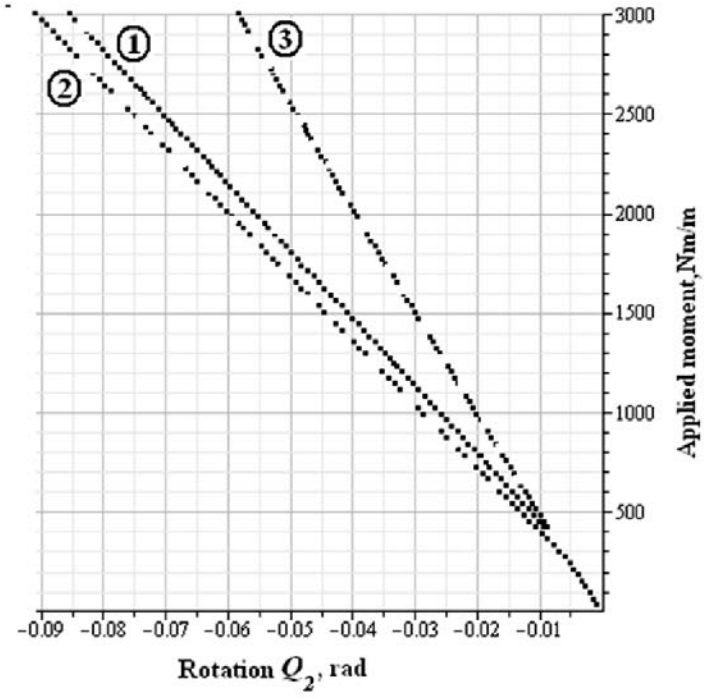

Figure 3.14: Analytical rotational displacement Q_2 against applied moment per unit width M for a T800/M21 $[0]_{16}$ configuration. The circled numbers identify 1) Stable 2) Unstable 3) Infeasible solutions.

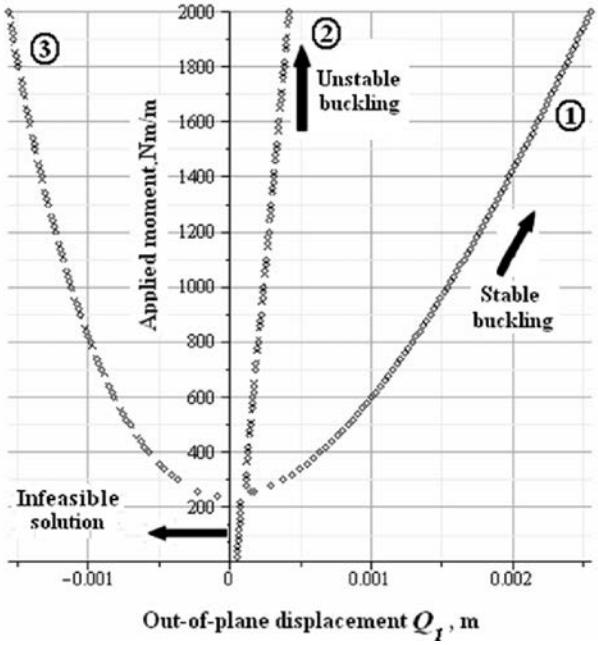

Figure 3.15: Analytical displacement Q_1 against applied moment per unit width M for a IM7/8552 $[0]_{32}$ configuration. The circled numbers identify 1) Stable 2) Unstable 3) Infeasible solutions.

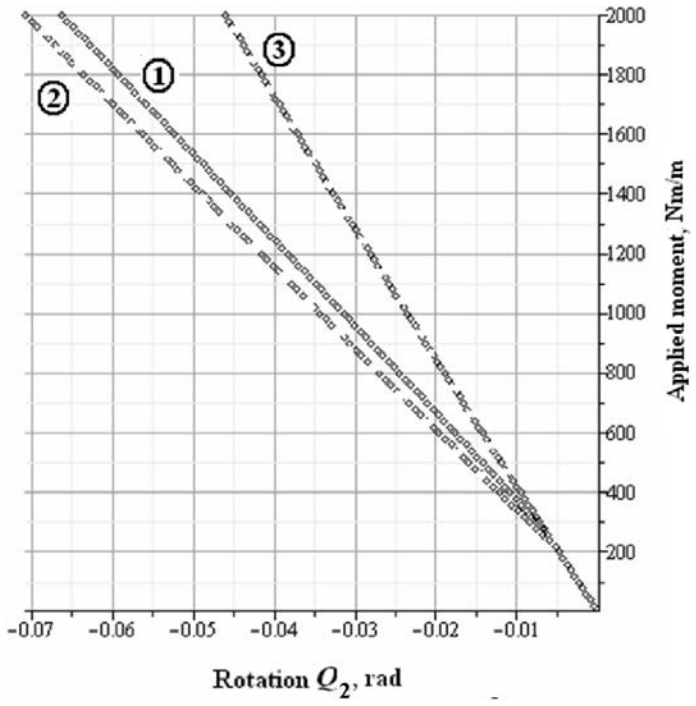

Figure 3.16: Analytical rotational displacement Q_2 against applied moment per unit width M for a IM7/8552 $[0]_{32}$ configuration. The circled numbers identify 1) Stable 2) Unstable 3) Infeasible solutions.

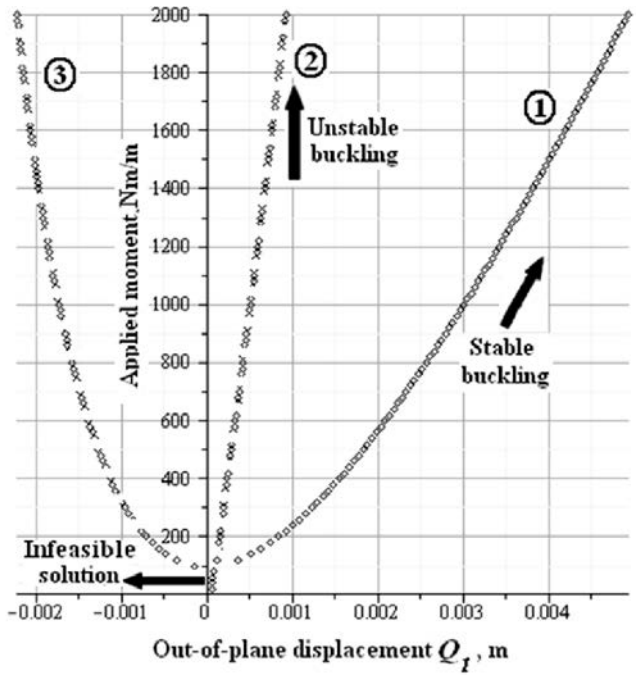

Figure 3.17: Analytical displacement Q_1 against applied moment per unit width M for a IM7/8552 $[45/90/-45/0]_{4s}$ configuration.The circled numbers identify 1) Stable 2) Unstable 3) Infeasible solutions.

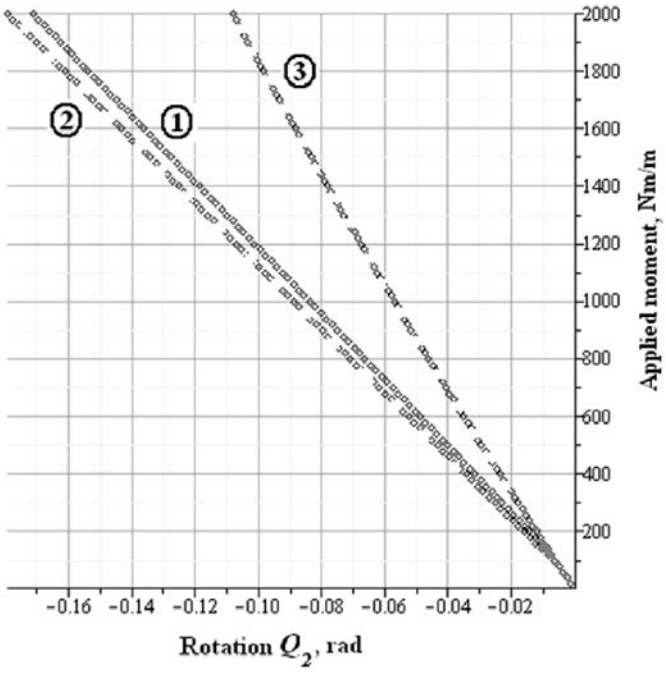

Figure 3.18: Analytical rotational displacement Q_2 against applied moment per unit width M for a IM7/8552 $[45/90/-45/0]_{4s}$ configuration. The circled numbers identify 1) Stable 2) Unstable 3) Infeasible solutions.

3.5.1 Snap-buckling moment

By minimising the energy Equation (3.2.9) with respect to Q_1 and Q_2, the snap-buckling amplitude Q_1 and end rotation Q_2 were obtained in terms of the applied bending moment M. The system of equations was solved for the three material systems assuming an initial imperfection value Q_o=0.02 mm in Equation (3.2.3). This value was to represent the real PTFE layer within the laminate. Average moduli and cured ply thicknesses, presented in Tables 3.1, 3.2 and 3.3, were used as the model assumed the material to be isotropic. The resulting solution of Q_1 for the T800/M21 beam configuration is shown in Figure 3.19. Note that the infeasible solution (negative side) corresponds to the thin and thick sub-laminates passing through each other.

As seen in Figure 3.19, the critical moment for the equilibrium solution does not appear as a distinct point on the moment vs. Q_1 plot. The critical moment for an unstable system is characterised by more rapid growth of the deflections as the critical moment of the perfect system is approached [87]. In order to obtain this point, a parametric study was carried out on the system of equations by changing the initial imperfection value (Q_o) to produce the convergence trend of the resulting (Q_1) plots (see Figure 3.19). For the aforementioned delaminated beam system, the imperfection was changed from 0.02 mm to 0.07 mm which showed that the critical moment level converged around a value of 300 Nm/m for T800/M21 specimen configuration. After running similar analysis, a value of 210 Nm/m and 64 Nm/m was obtained for snap-buckling of the IM7/8552 unidirectional and quasi-isotropic specimen configurations, respectively.

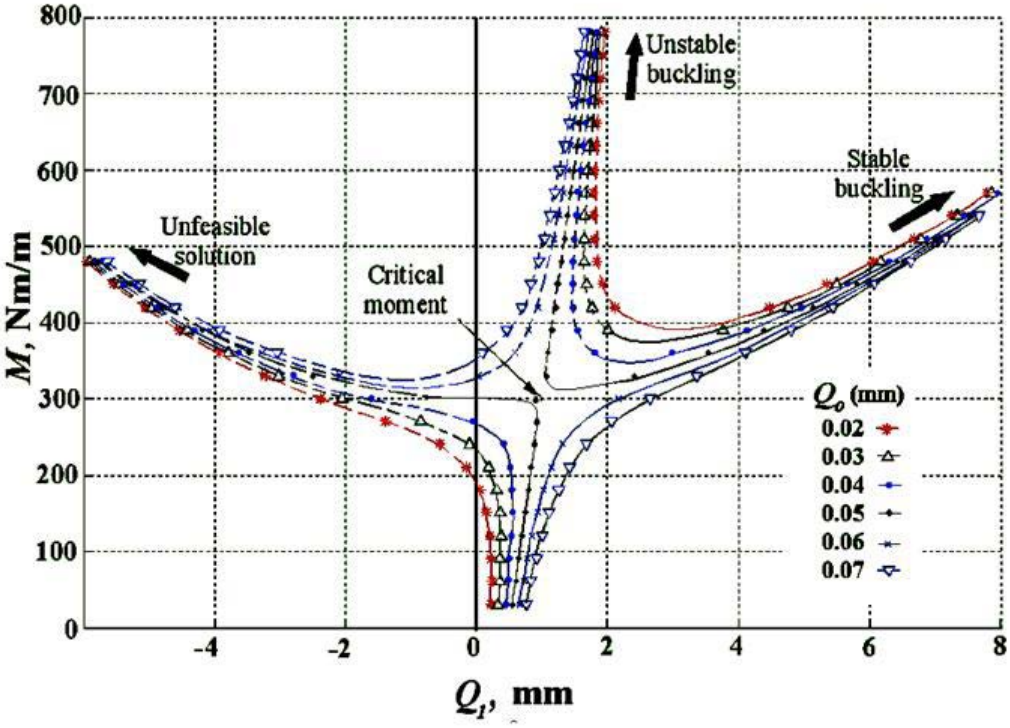

Figure 3.19: Equilibrium solutions showing analytical displacement Q_1 against applied moment per unit width M for a range of imperfections Q_o (T800/M21 specimen).

3.5.2 Kinematics solution for unidirectional laminates

The kinematics investigation of the model was important to obtain the force and moment components at the delaminated fronts. Such components were used to calculate the strain energy release rate at propagation. This was performed by measuring the out-of-plane displacement, Q_1, experimentally and comparing it against the analytically obtained value. A high resolution camera was used to take snap-shots centred and focused on one side of the specimen at different loads. Each image was then enlarged to its maximum resolution capacity to reduce the measuring error. Finally, a vector image manipulation software was used to measure the required value. The opening displacement, Q_1, was measured between the innermost edges of the upper and lower sub-laminates and then compared to the total thickness of the specimen at a marked place, initially measured using a digital vernier. Figures 3.20, 3.21 and 3.23 show graphical comparisons between experimentally acquired values for opening displacement,

Q_1, and the predicted values by the model obtained for the stable branch of the solution for Q_1. The three figures show a good match between the experiment and model for the T800/M21-$[0]_{16}$, IM7/8552 $[45/90/-45/0]_{4s}$ and the IM7/8552-$[0]_{32}$ material specimens, respectively. In all figures, the dashed lines represent quadratic fit for the measured Q_1 data.

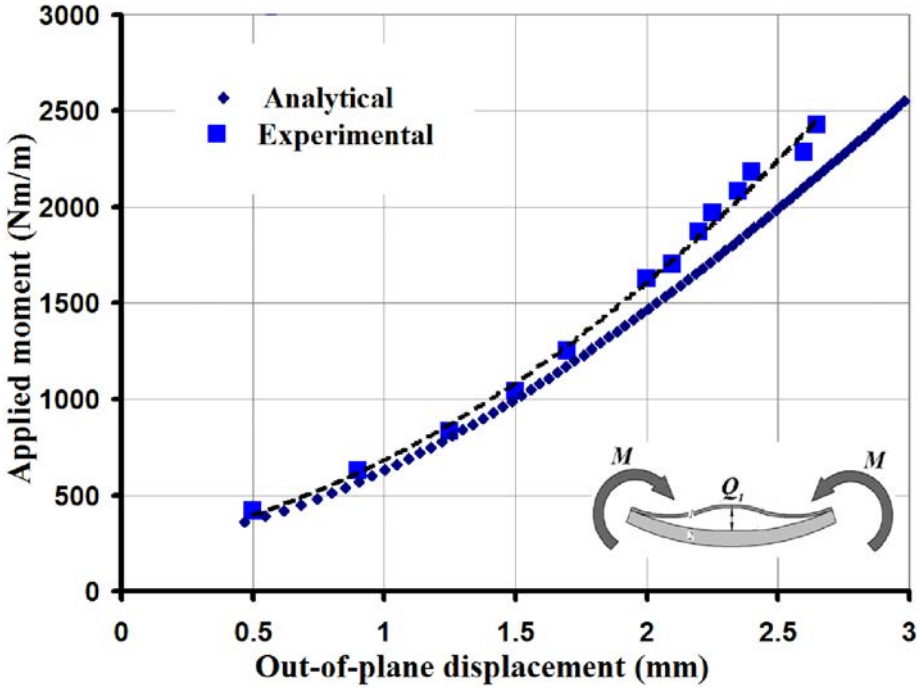

Figure 3.20: Out-of-plane displacement Q_1 comparison for T800/M21 material specimen, Q_o=0.02 mm.

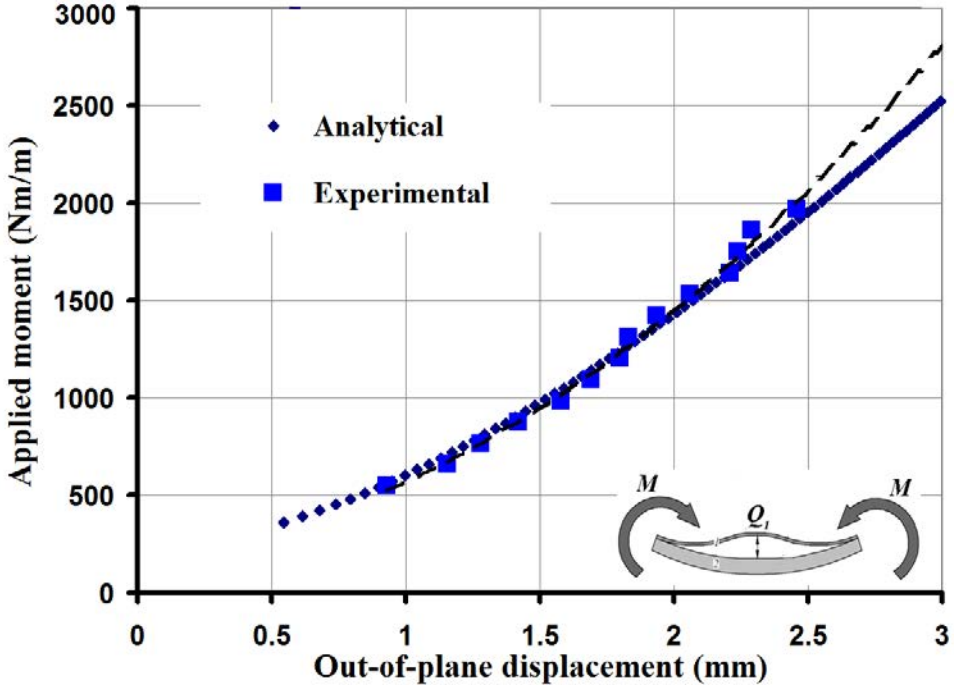

Figure 3.21: Out-of-plane displacement Q_1 comparison for IM7/8552 $[0]_{32}$ material specimen, Q_o=0.02 mm.

3.5.3 Kinematics solution for quasi-isotropic laminates

The analytical method was then extended to fit the quasi-isotropic laminate assumption. As the sub-laminate and the base laminate had non-symmetric arrangements of carbon layers, the neutral axis was re-established for each sub-laminate and then the modified bending rigidities were obtained with respect to the new neutral axis for each sub-laminate. It was clear that the neutral axis of the thin sub-laminate was shifted away from the mid-plane towards the [0] layer (bottom of the laminate). While the neutral axis of the base laminate was slightly shifted from its mid-plane. The scheme in Figure 3.22 shows the neutral axis shift for the quasi-isotropic laminate.

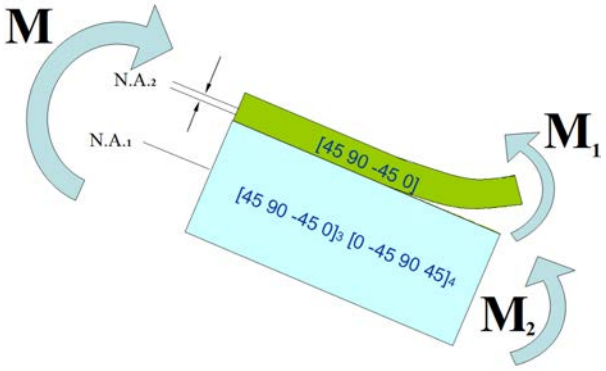

Figure 3.22: Neutral axis shift for the quasi-isotropic IM7/8552 $[45/90/-45/0]_{4s}$ material specimen.

The new modified values of neutral axes shift were introduced in the stretching displacement terms in Equations (3.2.4) and (3.2.5), respectively. The bending rigidities EI_1 and EI_2 were also changed in Equations (3.2.6) and (3.2.7), respectively.

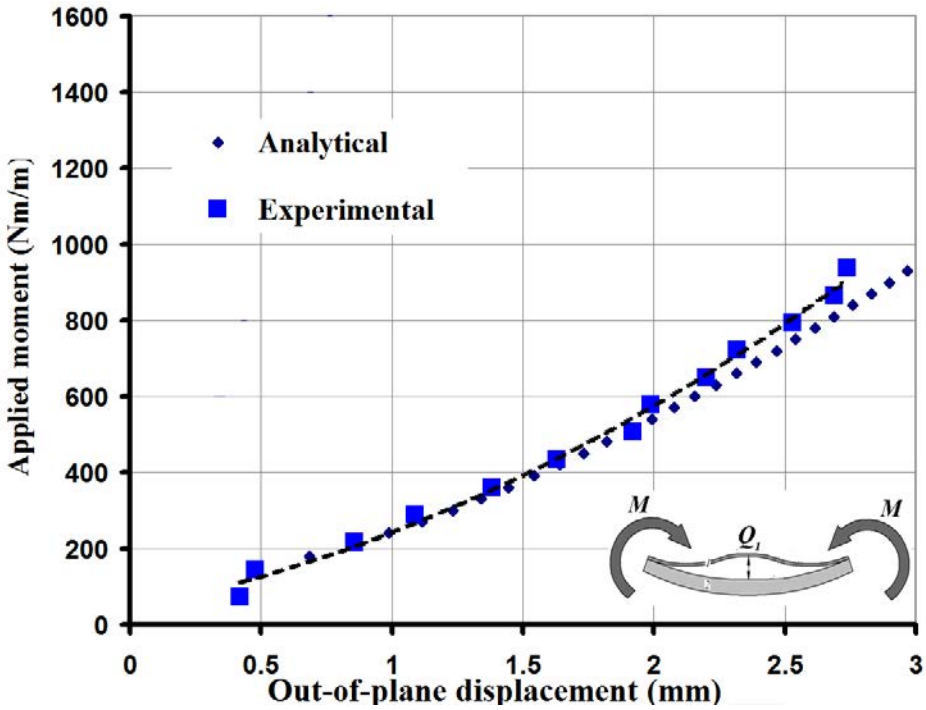

Figure 3.23: Out-of-plane displacement Q_1 comparison for IM7/8552 $[45/90/-45/0]_{4s}$ material specimen, Q_o=0.02 mm.

A similar verification check of the rotation displacement Q_2 was not possible using the aforementioned technique used to obtain the opening displacement Q_1. An unsuccessful trial to employ the DIC system was performed to measure the rotation, Q_2, values at the delamination edges. The measurements were recorded on the specimen sides which were too shallow to spread a proper speckle pattern distribution across. The obtained DIC images had poor accuracy.

3.5.4 Propagation moment results

After investigating the model kinematics, the post-buckling results of the analytical model were further employed to predict the propagation moment using two analytical methods. As the tested specimen configurations had a delamination of length-to-thickness ratio 80, the delaminated sub-laminated could be approximated as a fixed-fixed strut under compression and hence the thin film analysis [21] was utilised to predict the propagation moment. As an initial approximation, Mode-I critical values of G_{IC} for T800/M21 and IM7/8552 configurations were substituted in Equation (3.2.10), then equations (3.2.11) and (3.2.12) were used to calculate moment levels for propagation. They were found to be 1430 Nm/m, 850 Nm/m and 560 Nm/m for the T800/M21-$[0]_{16}$, IM7/8552 $[45/90/-45/0]_{4s}$ and the IM7/8552-$[0]_{32}$ material specimens, respectively, which are significantly less than the average value from static tests results. Such an outcome suggested that Mode-II has more influence upon propagation than Mode-I, and so two mixed mode analysis is considered next.

The second analytical method based on isotropic material assumption, assumed a planar crack propagation and that the thickness ratio between the thin sub-laminate and the base laminate is small. The fracture was assumed to occur through a plane stress condition at both delamination edges simultaneously.

The key material properties for predicting the propagation using the latter method were axial modulus, critical fracture toughness components for Mode-I and Mode-II. The model calculates the Mode-I and Mode-II energy components using the moment and force values at the delaminated edge as described through equations (3.2.13)-(3.2.15). Such values were calculated from the post-buckling analysis. The values of Q_1 and Q_2 were extracted for the stable branch of the equilibrium diagrams in Figures 3.13 - 3.18 by minimising the energy term in

Equation (3.2.9). Strain energy release rate components for Mode-I and Mode-II, G_I and G_{II}, were evaluated using Equation (3.2.15).

It was concluded in different literature that the critical Mode-II toughness value G_{IIC} is generally an unrepeatable material property. Therefore, it was checked against results obtained elsewhere for the M21 resin and found to range from 1200 J/m^2 [88] to 1600 J/m^2 [89]. For analysis of T800/M21 specimens, the critical value for G_{IIC} was taken as 1400 J/m^2 taken from a characterisation test by Ilyas [90]. Fracture toughness values, G_{IC} and G_{IIC}, for IM7/8552 material were taken as 210 J/m^2 and 1000 J/m^2, respectively [91]. The failure index (G_I/G_{IC}+G_{II}/G_{IIC}) was calculated for specimens made from the three specimen configurations.

Figure 3.24 shows a plot for the strain rate release rate for the T800/M21 specimen configuration. Using the material properties stated in Table 3.4, a failure index of 1.0 corresponds to a moment value of 2627 Nm/m which is 3.6% below the average propagation moment recorded in experiments. It is observed that, by increasing the applied moment, the curvature increased and the Mode-I component approached zero while Mode-II was dominant for inducing propagation. A similar conclusion was reached by Shan & Pelgeri [70], who noted that Mode-II fracture was dominant when the contact zone of delaminated beams increased due to beam curvature. For the IM7/8552-$[0]_{32}$ specimen configuration, Figure 3.25 shows the predicted propagation moment when is predicted at 2150 Nm/m which is 5% less than the observed propagation moment in experiments.

The propagation moment solution was repeated for the IM7/8552 $[45/90/-45/0]_{4s}$ specimen configuration. The predicted moment value was 19% less than the average value observed in experiments. The solution for the latter laminate configuration is presented in Figure 3.26. A summary of results of both analytical methods for all specimen configurations are exhibited in Table 3.5.

Table 3.5: Propagation moment results summary

	Thin-Film Analysis (Nm/m)	Mixed-Mode Analysis (Nm/m)	Experimental Propagation (Nm/m)
T800/M21-$[0]_{16}$	1830	2627	2725
IM7/8552-$[0]_{32}$	955	2150	2268
IM7/8552-$[45/90/-45/0]_{4S}$	560	1300	1600

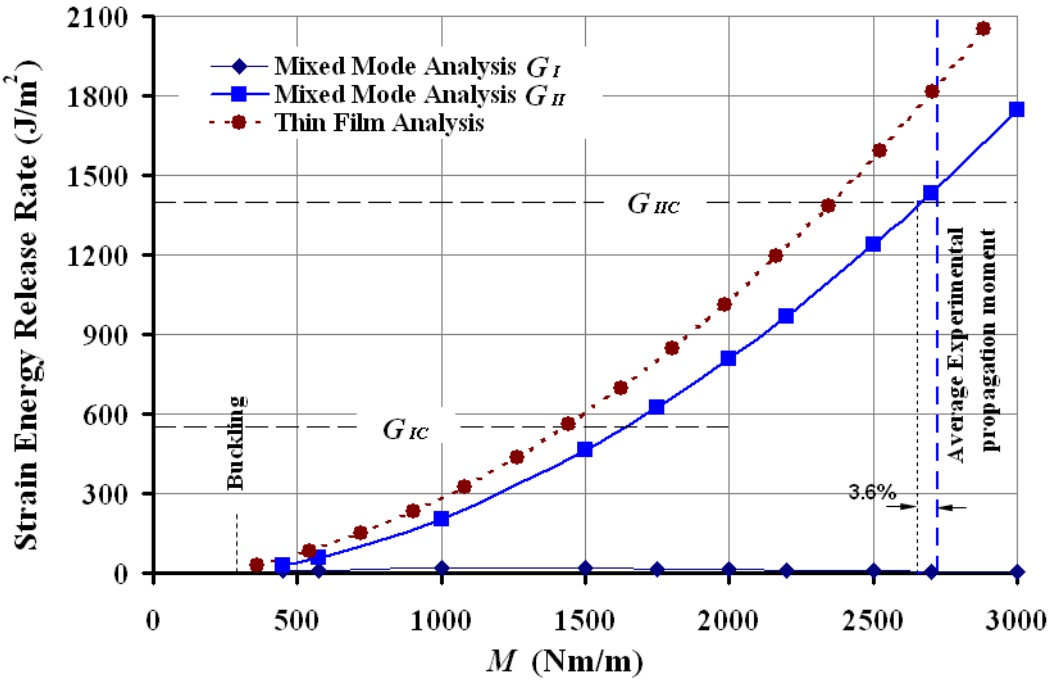

Figure 3.24: Strain energy release rate using the thin film and mixed-mode analysis for the delaminated, post-buckled beam - T800/M21 $[0]_{16}$ specimens. G_{IIC}=1400 J/m^2

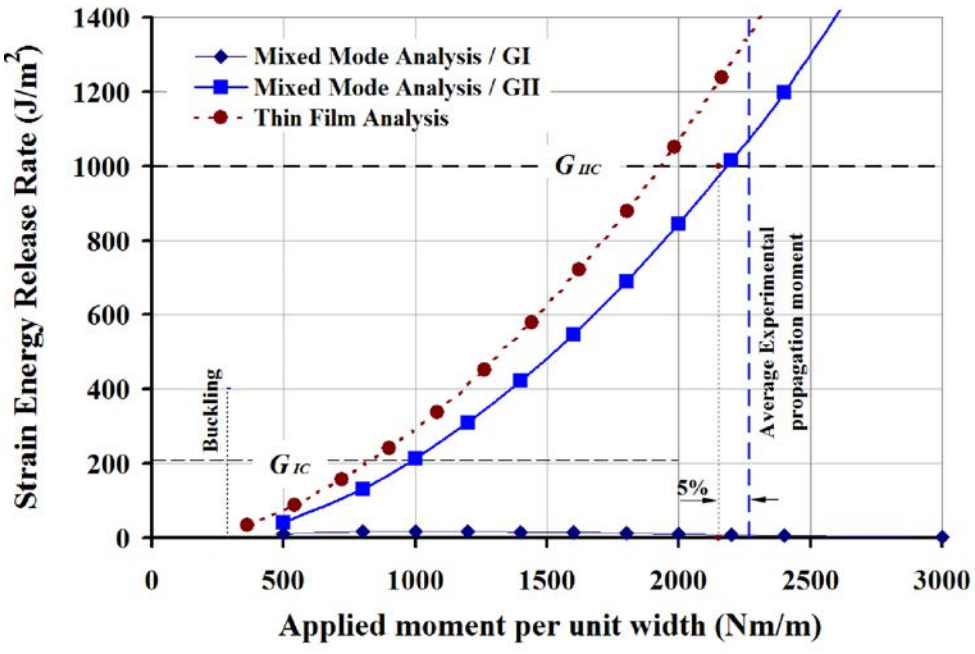

Figure 3.25: Strain energy release rate using the thin film and mixed-mode analysis for the delaminated, post-buckled beam - IM7/8552 $[0]_{32}$ specimens. G_{IIC}=1000 J/m^2.

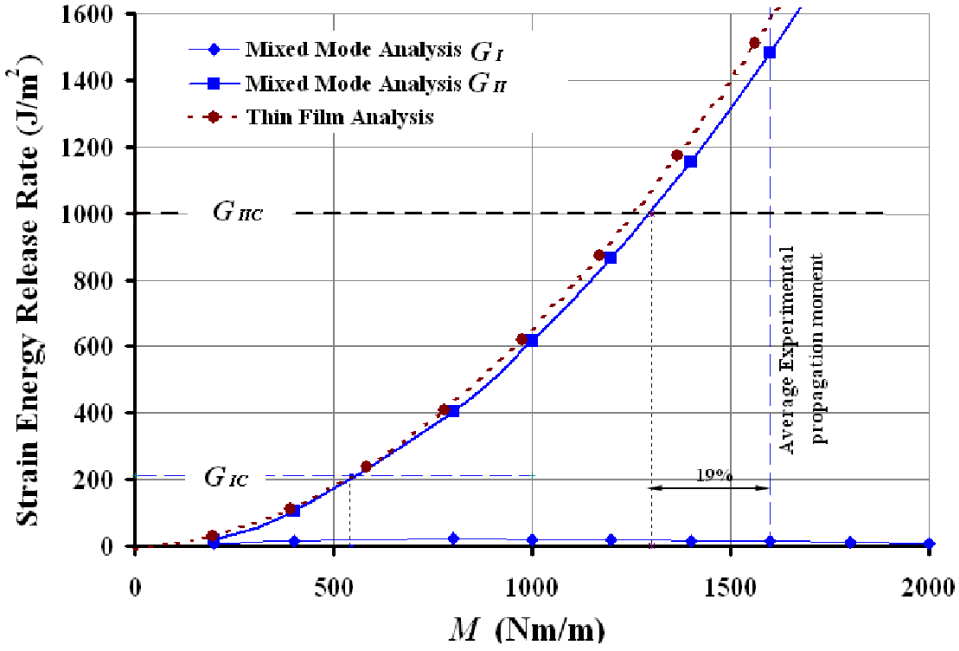

Figure 3.26: Strain energy release rate indices for Mode-I and Mode-II contributions to the delaminated, post-buckled beam - IM7/8552-$[45/90/-45/0]_{4s}$ specimens. G_{IIC}=1000 J/m^2.

3.6 Discussion of Results

3.6.1 Predicted snap-buckling moment values

Based on the initial pilot testing, suitable specimen geometry and testing parameters were decided for the main testing programme. As a result, all tests were performed under displacement control to obtain the snap-buckling and propagation moment levels under pure bending moment.

Static test experiments performed on T800/M21 $[0]_{16}$ specimens showed an average snap-buckling moment value of 270 Nm/m which is 11% less than the value obtained using *Rayleigh-Ritz* methodology. While experiments on a IM7/8552 $[0]_{32}$ specimen showed a value of 223 Nm/m which is 5% above the predicted value. The snap-buckling value for the IM7/8552 $[45/90/-45/0]_{4s}$ was 64 Nm/m. It was not possible for the latter laminate to establish a comparison with experimental values as the tested beams exhibited opening from the start of loading. The analysis included the effect of an initial imperfection on the buckling moment value. The solution of the system revealed three equilibrium branches, see Figures 3.13-3.18, : infeasible, unstable and stable, where the infeasible branch means the sub-laminates pass through one another. One tested T800/M21 $[0]_{16}$ specimen with a snap-buckling moment value of 706 Nm/m seemed to follow the unstable branch until it snapped up to the stable (opening) branch of the plot. Other T800/M21 $[0]_{16}$ specimens followed the stable branch of the plot throughout.

3.6.2 Kinematics results

The kinematic analysis showed good agreement with the experimentally acquired Q_1 values for the three specimen sets, shown in Figures 3.20, 3.21 and 3.23. Such verification was a substantial step to further predict the propagation moment levels for the three studied sets. The cured thickness of the manufactured laminate was used in the model to eliminate any error by using the raw material thickness. The measuring technique was thought to reduce the visual error by pin-pointing the sub-laminate edges on a high resolution image via a vector manipulation soft-

ware. The verification for the T800/M21 unidirectional configuration showed a good match for half of the tested range and then a slight divergence between the experimentally measured values from the predicted ones. Excellent agreement for measured and predicted Q_1 displacement was shown for the IM7/8552 $[0]_{32}$ and $[45/90/-45/0]_{4s}$, respectively.

3.6.3 Fractography analysis

Electron scanning microscopy for a failed T800/M21 specimen tested under bending showed a repeated pattern of shear cusps. The axes along the cusps valleys were perpendicular to fibre direction. The cusps were filling a similar area when the scan was repeated at 20 mm away from the delamination front. Such observation suggests that Mode-II failure dominated as the delamination propagated at the bent fronts of the delamination. Scanning images for a failed DCB specimen made of the same material showed a typical textured area caused by plastic tearing of resin reach areas, which characterises pure Mode-I failure of tough resin material. The dominating effect of Mode-II over Mode-I at delamination front for bent beams under compression was pointed towards by Rothschilds et al [69], who studied thin film delamination under compression. They suggested that the delamination geometry is not symmetric about the delamination front; hence the opening moment for the top delaminated layer gives rise to interlaminar shear stresses at the delamination tip which increased Mode-II significantly more than Mode-I. Such an effect may be similar to the case presented in this study as the bending of the beam induces opening of the top delaminated layer.

3.6.4 Propagation moment results

The prediction of propagation moment levels was carried out using two analytical methods, thin-film analysis and the mixed-mode method. The earlier one was used based on the assumption that the delamination could be approximated as a strut under compression. The mixed-mode method has the advantage of separating both mode energy release rates and hence each mode contribution could be obtained. The thin-film analysis showed a significant deviation from experimentally acquired propagation moment in T800/M21 and IM7/8552 configurations,

respectively when only incorporating Mode-I fracture toughness value as assumed within the model.

The mixed mode analysis was investigated. It included two different expressions for Mode-I and Mode-II strain energy release rates G_I and G_{II}. Both energy terms depend on the force and moment components at the delamination edge. A linear failure index ($G_I/G_{IC} + G_{II}/G_{IIC}$) was used to obtain the propagation moment level. The estimation of G_{IC} and G_{IIC} values is essential to the analysis accuracy. While Mode-I Fracture toughness G_{IC} was of small influence, G_{IIC} was a key parameter in the analysis and the predicted propagation moment value. Consequently, utilising power-based failure indices such as $(G_I/G_{IC})^2 + (G_{II}/G_{IIC})^2$, the propagation results will not significantly differ from the results obtained using the linear failure index.

The Mode-II fracture toughness values, G_{IIC}, were taken as 1400 Nm/m and 1000 Nm/m for T800/M21 and IM7/8552 material systems, respectively. After incorporating a mixed mode strategy developed by Hutchinson & Suo [77] for the example considered above, it was shown that Mode-I had a similar influence to Mode-II immediately after the snap-buckling moment level. The Mode-I contribution then diminishes as the load increased. Finally, the propagation failure was dominated by Mode-II due to the increase in curvature of the beam during bending, which gives rise to shear stress at the contact surface. The deviation between analytical prediction and experiments was 3.6% and 5% for T800/M21 and IM7/8552 unidirectional configurations, respectively. The mixed mode analysis for the IM7/8552 $[45/90/-45/0]_{4s}$ configuration resulted in a propagation moment value of 19% less than the average moment value obtained in experiments. Although the kinematic analysis for the laminate had good agreement with experiments, the isotropic material assumption used in the equation was not sufficiently representative for the whole quasi-isotropic laminate. A better approximation for the solution could be obtained using classical lamination plate theory to account for the bending-twist stiffness components, D_{13} and D_{33}.

3.6.5 Fatigue test results

Fatigue tests were performed on the three specimen sets using the same static test setup and configurations using a test frequency of 4 Hz and a loading ratio

of R=10. The testing programme was performed to study the effect of having an opening mode on fatigue life of the delaminated specimens. The tested T800/M21 $[0]_{16}$ specimens had a little growth in the tested specimen with 0.21 severity level, while no growth of delamination at a severity level of 0.1725. The maximum opening displacement Q_1 measured for the latter specimen under fatigue testing was much less than the corresponding displacement recorded at the maximum bending moment under static testing. It was apparent that by varying the fatigue load around the snap-buckling moment level forced the sub-laminate to nearly exhibit a closing mode through the whole loading cycle and never reach the maximum opening displacement attained during the corresponding static test. Therefore, it can be concluded that any loading cycles with both the maximum and minimum moments higher than snap-buckling moment, will have a higher deteriorating effect on the fatigue life of the delamination. Hence the prediction of such snap-buckling moment for delamination is significant in the study of fatigue of delaminated composites.

Specimens made from IM7/8552 $[0]_{32}$ showed no growth after 10^6 cycles at a severity level of 0.175. Compared to the latter configuration, the IM7/8552 $[45/90/-45/0]_{4s}$ specimens had less delamination growth at similar level of severities. In this case, a severity level of 0.3 produced 1 mm delamination extension after 10^6 cycles. Such outcome suggests the quasi-isotropic laminate to be a more fatigue tolerant than the unidirectional configuration.

No fatigue growth was observed when the applied moment was 80% below the static strength value in both unidirectional configurations. Fatigue growth of the delamination occurred after 10^6 cycles at a moment that was 75% above the snap-buckling moment. This is a lower moment than might be expected considering that static propagation did not occur until about 10 times the snap-buckling moment.

3.7 Conclusions

Delaminated beams made from unidirectional carbon fibre composites were studied under pure bending moment. A nonlinear mathematical model was used to predict the moment level for snap-buckling of the upper sub-laminate while

including the effect of the initial imperfection created by the PTFE used to delaminate the beam. The method showed two types of sub-laminate behaviour; opening (stable) and closing (unstable). The predicted moment levels for snap-buckling were deviated by 11% and 5% from the average experimental value for unidirectional T800/M21 $[0]_{16}$ and IM7/8552 $[0]_{32}$ beam configurations, respectively. Experiments performed on IM7/8552 $[45/90/-45/0]_{4s}$ configurations showed the sub-laminate opening started as soon as the load was applied, this was due to more flexibility of the sub-laminate compared to the unidirectional configuration. Prediction using the nonlinear method had a snap-buckling moment level of 64 Nm/m.

A mixed mode technique [77] was applied and the propagation moment was found to be approximately 3.6% and 5% compared to experimentally obtained values for the T800/M21 $[0]_{16}$ and IM7/8552 $[0]_{32}$ beams, respectively. A conservative prediction of 19% was obtained for the IM7/8552 $[45/90/-45/0]_{4s}$ specimen configuration following a modification provided to the analytical technique. The method initially assumed a homogenous, isotropic material. And hence some terms were modified in the equations to accommodate the shift of the neutral axis for latter configuration.

As observed by electron scanning microscopy, Mode-II failure characterised the bend T800/M21 beams in question compared with a previous DCB test specimen failure which is a pure Mode-I failure. A similar outcome was predicted by the model which suggested that Mode-II has more influence than Mode-I behaviour in static propagation.

One interesting outcome of the current work is that it represents a promising method to determine Mode-II fracture toughness, since tested specimens showed propagation in a repeatable manner for both types of material systems. Such repeatability is not the case for G_{IIC} values obtained by typical Mode-II characterising tests such as End Notched Flexure (ENF) and Four-Point Notched Flexure (4ENF). Consequently, by applying the mixed-mode methodology along with the obtained propagation moment results from experiments, G_{IIC} values of 1480 (J/m^2) and 1030 (J/m^2) would correspond to T800/M21 $[0]_{16}$ and IM7/8552 $[0]_{32}$ specimen configurations, respectively.

Fatigue tests showed that crack growth occurred at a comparatively low level of severity (around 20% of the static propagation moment) before one million cycles, which highlights the importance of predicting the likelihood of an opening mode for a near-surface delamination. Such a low growth level might be due to the geometry of the tested beam, i.e. it had a near-surface through-width delamination. The quasi-isotropic IM7/8552 $[45/90/-45/0]_{4s}$ configuration showed a better fatigue tolerant laminate than the unidirectional one made of the same material. In real applications, damage usually consists of enclosed delaminations distributed within the thickness of the laminate. However, the result underlines the weakness of composites when subject to moments causing delamination opening.

Chapter 4

Experimental Study of Two-dimensional Delaminated Specimens Under Bending

4.1 Scope

The current chapter investigates the propagation of two-dimensional damage within composite laminates under bending and exhibiting local surface bulging due to delamination buckling. The experimental study included testing of specimens with a barely visible impact damage (BVID) and circular-imbedded delaminations. The aim of this study was twofold: testing of BVID specimens to explore the behaviour of real impacted structures with buckled delamination under bending; testing of circular-imbedded delamination as a calibration methodology for future analytical models. Both experimental studies include static and fatigue testing.

4.2 Testing of BVID laminates

4.2.1 Introduction

Turning first to BVID laminates, so far there has been little discussion about delaminated composites subject to bending. The discussed through-width delamination specimens studied in the previous chapter was an initial step in understanding the real damaged structures under bending loading. Such damage has a complicated shape across the thickness of the laminate and hence the overall behaviour of the structure will vary considerably. The purpose of the following testing programme of BVID $[45/90/-45/0]_{4s}$ specimens was to study the effect of a locally-buckled sub-laminate on the strength of impacted composites under bending fatigue. The laminated plates were manufactured from IM7/8552 carbon prepreg. Static tests were initially carried out to obtain the snap-buckling and failure moment levels. Fatigue tests were then performed based on the obtained moment levels.

The steps to establish the BVID testing programme were as follows:

1. Establishing an impact threshold for the laminated plates;
2. Investigating the damage morphology;
3. Static testing of BVID specimens under bending;
4. Fatigue testing of BVID specimens under bending;

4.2.2 Establishing a damage threshold

Several impact tests were performed in order to establish threshold BVID damage, a damage that exists within the layers but not visibly seen from outside on the studied laminate. Impact levels were changed from 6 J to 10 J. Threshold damage was found to occur at an impact level of 8J, resulting in a damage enclosed within a circle of 32 mm diameter. Figure 4.1. shows force-time plots for different energy levels where the drop in force represents existence of damage. C-scan images were then taken using an ultrasonic C-Scan machine.

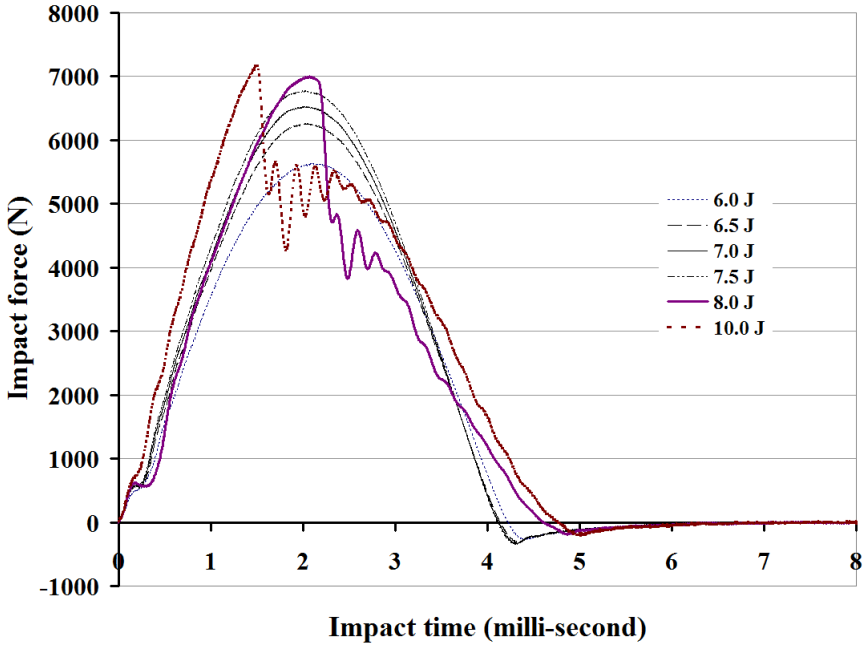

Figure 4.1: Impact response of BVID specimens under different energy levels.

4.2.3 Damage morphology

It is thought that impact damaged laminates have damage contained within three-dimensional conical boundary through the thickness, i.e. starting with a small damage below the impact site and increasing in radial-wise direction when moving towards the back side. Scans from both specimen sides were taken after impact in order to better describe the damage morphology. From the impact side, the following scan in Figure 4.2, taken within 1 mm depth, shows a damage confined within a 20 mm circle. The scanning frequency used was between (32 and 35) MHz. Such frequency is recommended for small thickness epoxy resin composites. The difference of the colour pattern within the represented damage suggested it was spread across different layers.

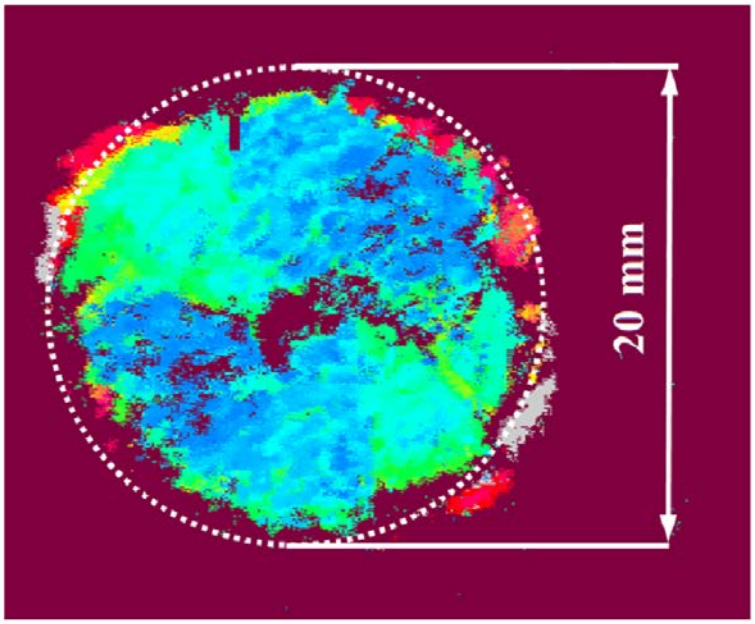

Figure 4.2: C-scan image taken from the impact side for a specimen impacted by 8J up to a scan depth of 1 mm.

A further investigation was performed on the back side, where maximum damage was expected to exist. Four subsequent scans were taken one after another within a thickness depth of 2 mm so that the signal through this half thickness was equally divided into four sections. The image in Figure 4.3-a shows that near the impact spot, the damage was shown as a bright area in the shape of triangle with a rounded corner. The subsequent scans in Figures 4.3-b, 4.3-c and 4.3-d show the size of the triangular shapes increases as the scan is taken away from the back surface. The darker straight lines separating the bright damaged areas suggest that each arc-shaped area existed per each scanned section and that they constructed a flower petal pattern or spiral-stepped shape. The scans also suggested that the damage morphology was not symmetric within each layer, i.e. not a mirrored peanut shape. The central void, around 7 mm diameter, appearing in the scanned images resulted from the compression exerted by the 16 mm impactor stub on the surface. Figure 4.4 shows an A-scan through the sectional horizontal plane at the impact spot. The brighter areas in the sectional view indicate that the damage lateral dimension near the back surface is greater than near the impact side, i.e the damage was confined within conical boundary.

The 3-D image in Figure 4.5 shows a depiction representing the predicted damage morphology.

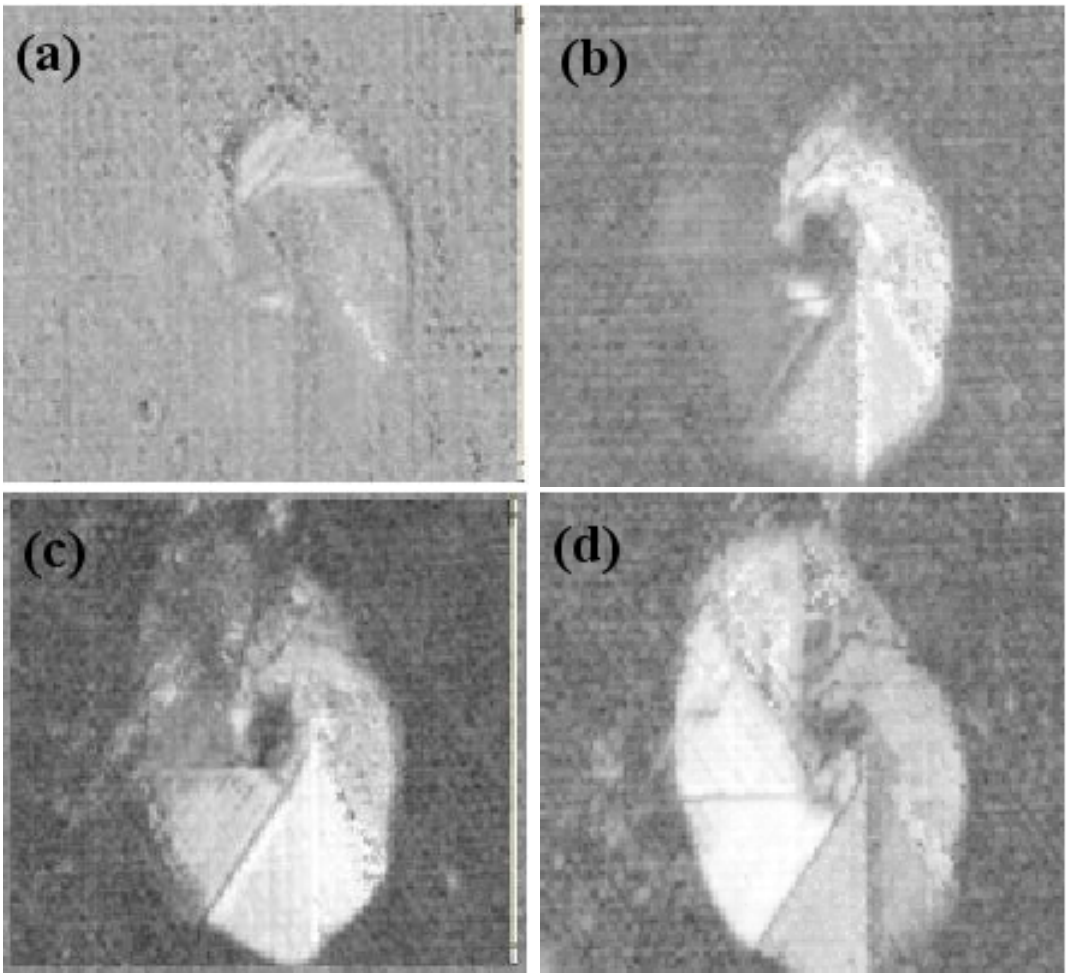

Figure 4.3: C-scan images taken at four equal steps through a thickness of 2 mm for a specimen impacted by 8J.

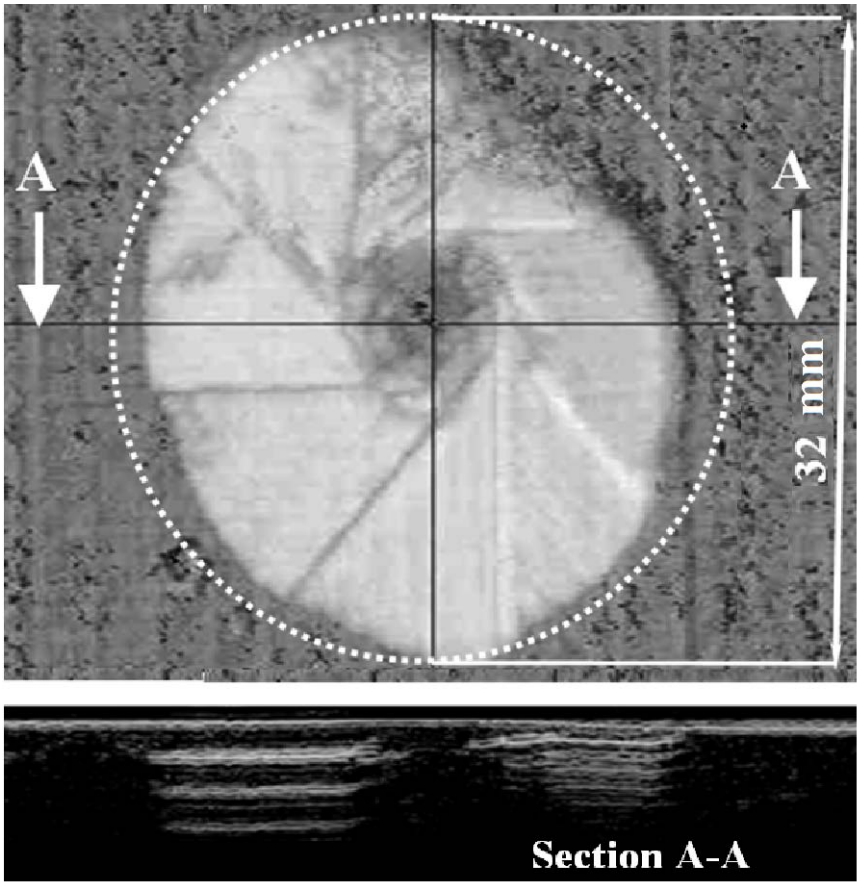

Figure 4.4: Sectional view represents A-Scan image through the thickness taken at the horizontal plane.

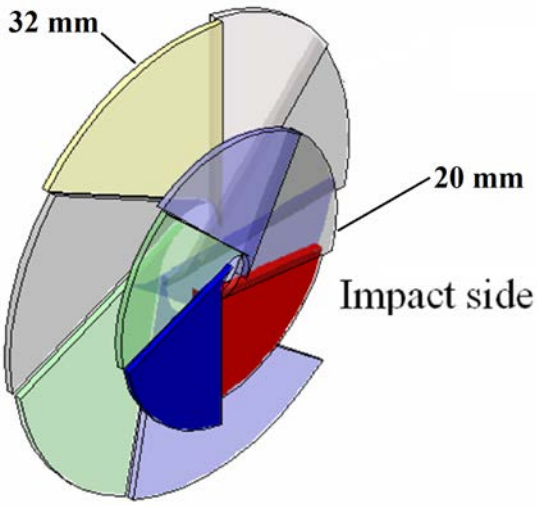

Figure 4.5: 3D representation of the damage elaborated from the previous stepped C-scan images.

4.2.4 Static and fatigue testing

Laminated plates of a $[45/90/-45/0]_{4s}$ layup were manufactured from the IM7/8552 carbon prepreg using the curing cycle described in Chapter A. The plates were then impacted by 8J in order to establish a damaged area as discussed in the previous sub-section. Impact force versus time curves are plotted in Figure 4.8

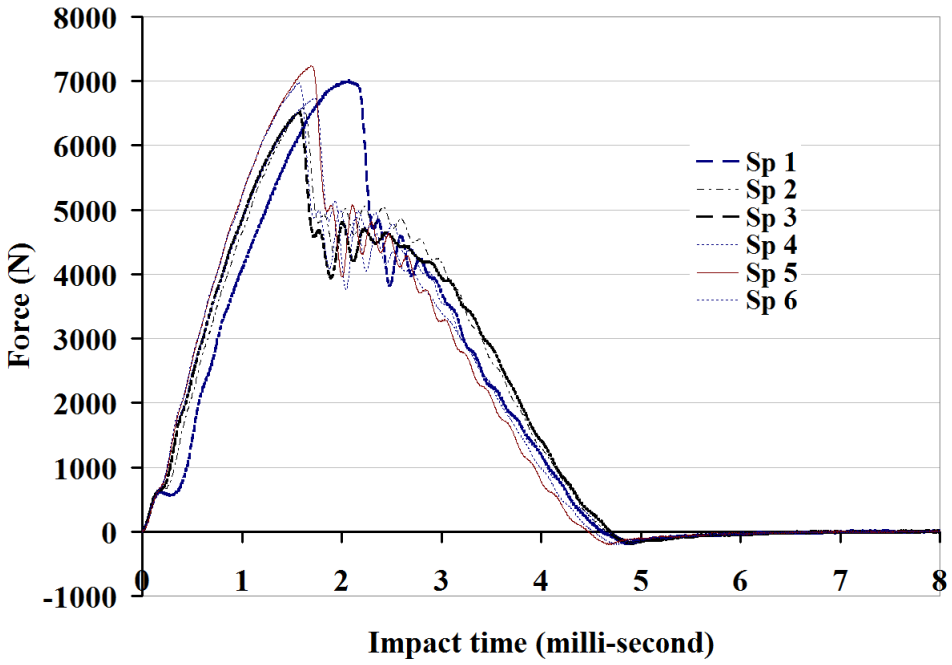

Figure 4.6: Impact response for six BVID specimens using an impact energy level of 8J.

Two plates were cut into six specimens of dimensions shown in Table 4.1 after being impacted and scanned using the Ultrasonic scanner. Two strain gauges were attached on those undergoing static testing. Each strain gauge was centred and placed as closer as possible above the damaged area of the specimen. The testing fixture in Figure 4.7 was used for both fatigue and static testing. The fixture consisted of upper and lower pieces, constructing four point bending setup. The rollers were 20 mm diameter and spans were adjusted manually and tightened at 65 and 185 mm. The static tests were performed using displacement control at a speed of 2.25 mm/min which corresponds to 300 N/min. Because delaminated composites are weaker under compression, the impact sides were placed downwards in order to apply a compression field on the side with maximum damage

size near the surface. Impact force values and the impact damage dimensions for the six specimens are included in Table 4.1.

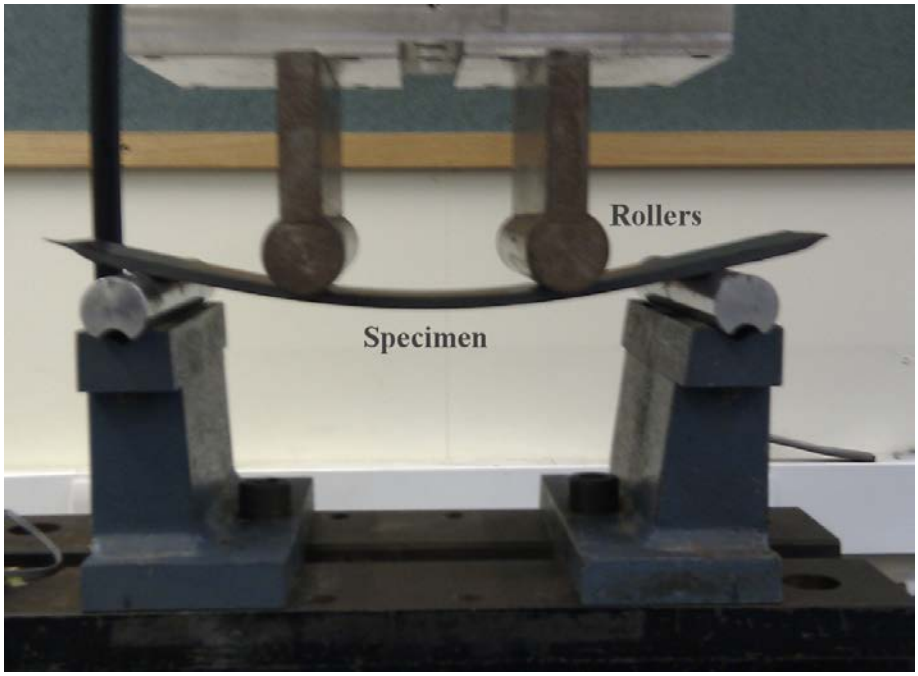

Figure 4.7: Four-point bending test setup for static and fatigue loading.

Table 4.1: BVID specimens size and impact damage dimensions for specimens tested under static and fatigue loading

	Loading	Width (mm)	Thickness (mm)	Impact peak force (N)	Damage longitudinal dimension (mm)	Damage lateral dimension (mm)
Sp1	Static	42.30	4.03	6790	32.00	30.00
Sp2	Static	45.40	4.03	6400	32.20	29.40
Sp3	Static	39.70	4.04	6450	25.60	25.00
Sp4	Fatigue	50.70	4.02	6729	32.50	27.50
Sp5	Fatigue	49.55	4.03	6846	31.80	27.40
Sp6	Fatigue	49.35	4.04	7134	32.00	30.50

4.2.5 Static tests results

For the first specimen, Sp1, a damage opening was observed to initiate at a central spot and then progressed towards one side at a moment level of 1080 Nm/m and finally extended back towards the other side. The opening was sighted after the 2^{nd} layer from one side while it appeared at the other side to exist after the 4^{th} layer. A final failure was recorded at a moment level of 1382 Nm/m. The second specimen, Sp2, possessed a similar damage progression. Its sub-laminate opening and failure were recorded at moment levels of 980 Nm/m and 1320 Nm/m respectively. The third specimen, Sp3, showed a different behaviour: opening did not occur until its final failure at 1612 Nm/m. Figure 4.8 shows moment versus displacement plots for the three tested specimens. Specimen dimensions and moment levels recorded from experiments are exhibited in Table 4.2.

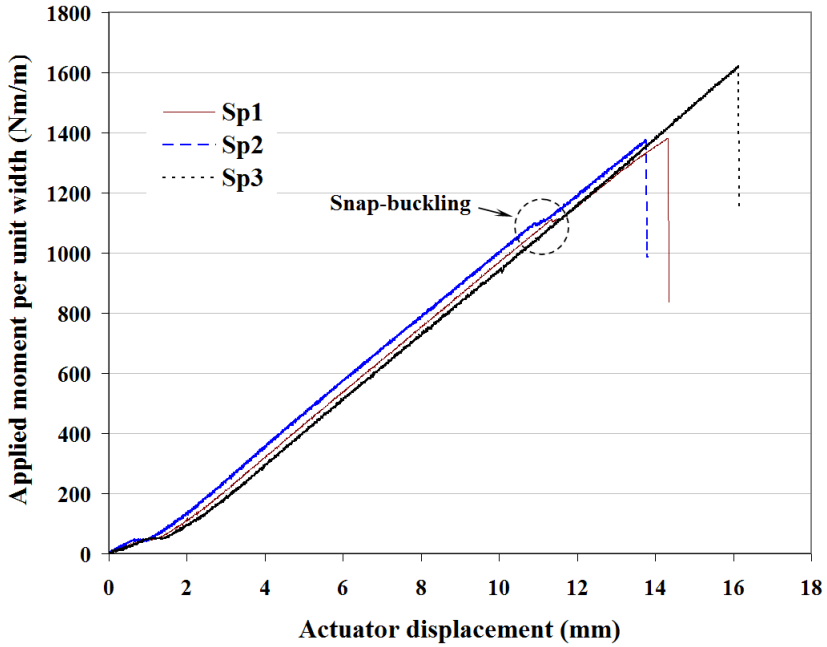

Figure 4.8: Applied moment versus actuator displacement for specimens tested under static bending

Table 4.2: Snap-buckling and failure moment levels for the tested specimens under static loading

	Width (mm)	Thickness (mm)	Snap-buckling moment (Nm/m)	Failure moment (Nm/m)
Sp1	42.30	4.03	1080	1382
Sp2	45.40	4.03	980	1372
Sp3	39.70	4.04	N/A	1612

4.2.6 Fatigue test results

Fatigue tests were performed using load control with a low loading ratio, R (maximum load/minimum load). The higher load ratios exceeded the capacity of the servohydraulic machine. The ratios for the following fatigue tests were 1.5, 1.3, 1.4 and 1.5, respectively. The load levels for all tests were performed with respect to the average snap buckling and failure moment levels obtained from the static tests. The inner and outer roller spans were 80 mm and 215 mm, respectively. All specimens were scanned using the Ultrasonic C-Scan machine after different subsequent number of loading cycles to check for any evidence of damage growth. The testing scheme for the four tested specimens is shown in Figure 4.9.

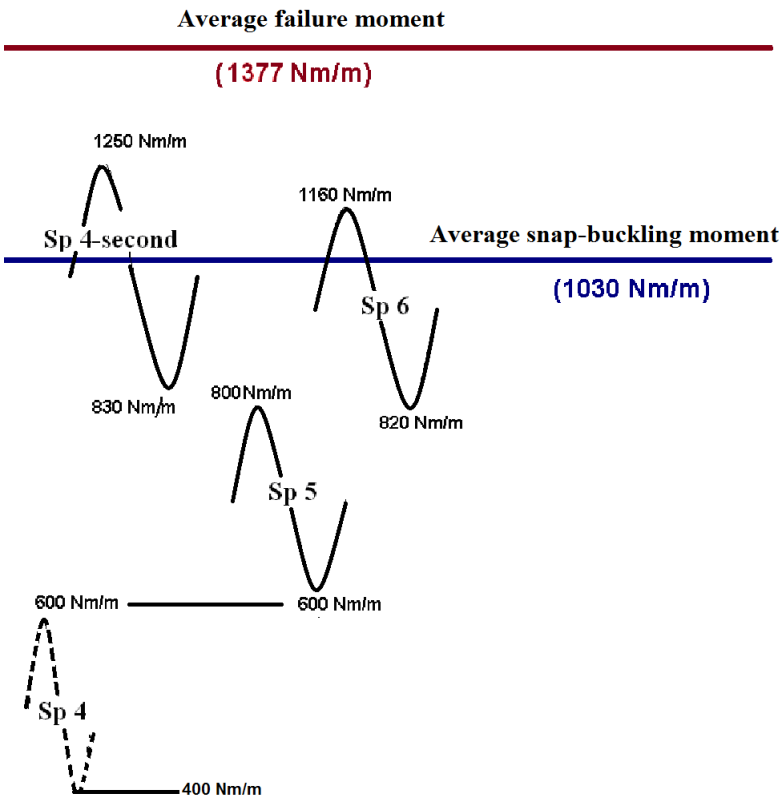

Figure 4.9: Fatigue testing scheme. The snap-buckling and failure moment were the averaged values calculated from static test results in Table 4.2.

Specimens Sp4 and Sp5 were tested below the average static snap-buckling moment level (1030 Nm/m) in order to investigate any likelihood for damage opening driven by the load fluctuation. No damage growth was recorded for these specimens at the mentioned number of cycles in the table below. The third test, Sp6, was carried out so that the maximum applied moment is above than the average static snap-buckling moment. This was performed by slowly increasing the load to the mean moment value and then applying the fatigue loading from this mean moment level. It was observed that as the load passed through the snap-buckling moment value during the initial loading step, a surface bulging, shown in Figure 4.10, appeared on the upper surface which extended to one side of the specimen with around 8 mm width while the thickness of the opened sub-laminate was 0.42 mm, i.e. four layers deep. The observed opening length on the specimen side did not grow during the whole test cycles. C-scan images shown in Figures 4.11 and 4.12 show the damage size before loading and after 116,000 cycles for specimen Sp6. No further growth was observed in the subsequent scans taken after the

number of cycles shown in Table 4.3.

After one million cycles, specimen, Sp4, was then tested with a higher loading ratio exhibited in Table 4.3. The load cycle passed through the snap-buckling moment value and ranged from 830 Nm/m to 1250 Nm/m. No visual opening was observed on the outer surface during the test. Ultrasonic C-scan images for the latter specimen, Sp4, were taken after the number of cycles displayed in the Table. These scans showed no further damage growth compared to pre-test scans of Sp4. The damage spread perpendicular to bending axis and towards one side as shown in Figure 4.10. In all tests, an anticlastic curvature clearly appeared on the lateral side of the specimen.

Table 4.3: Testing parameters and geometry for BVID specimens tested under fatigue loading

Specimen number	Width (mm)	Thickness (mm)	Max/min moment (Nm/m)	Cycles (1000)	Damage growth
Sp4	50.70	4.02	600/400	200 608 1000	No
Sp5	49.55	4.03	800/600	410 1000	No
Sp6	49.35	4.04	1160/820	116 374 658 1000	Yes
Sp4 second test	50.70	4.02	1250/830	337 684 1000	No

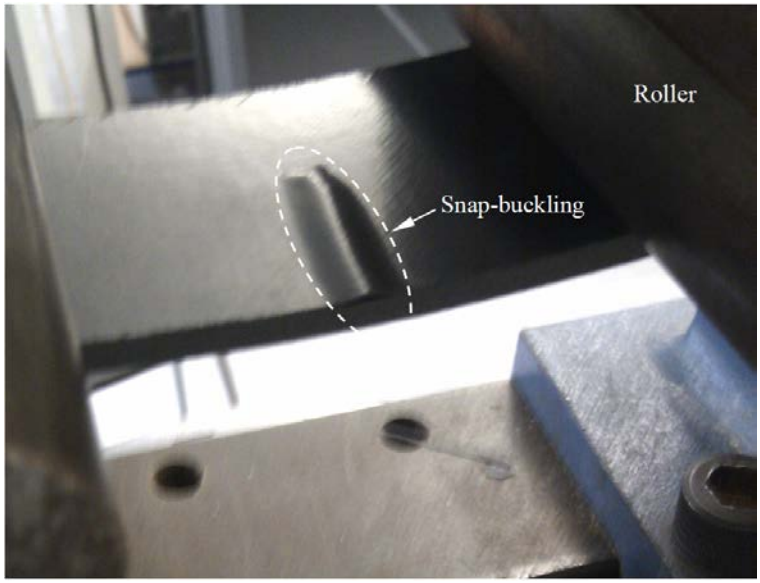

Figure 4.10: Delamination progress towards the specimen side during fatigue test of specimen.

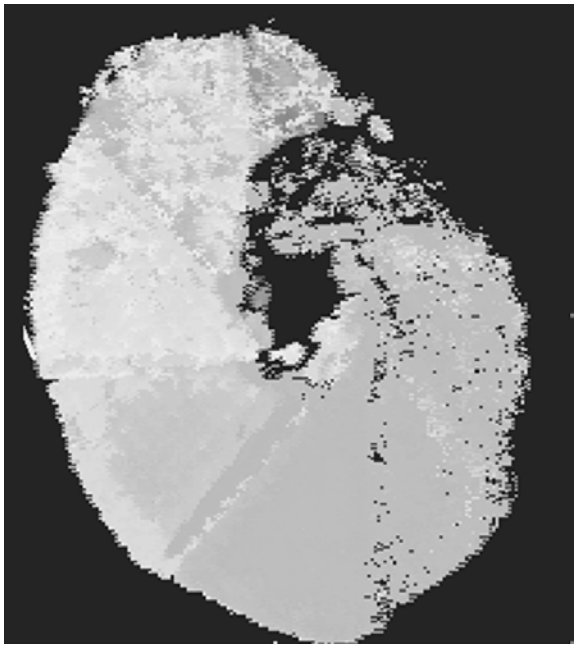

Figure 4.11: C-Scan image for Sp6 damage before fatigue testing.

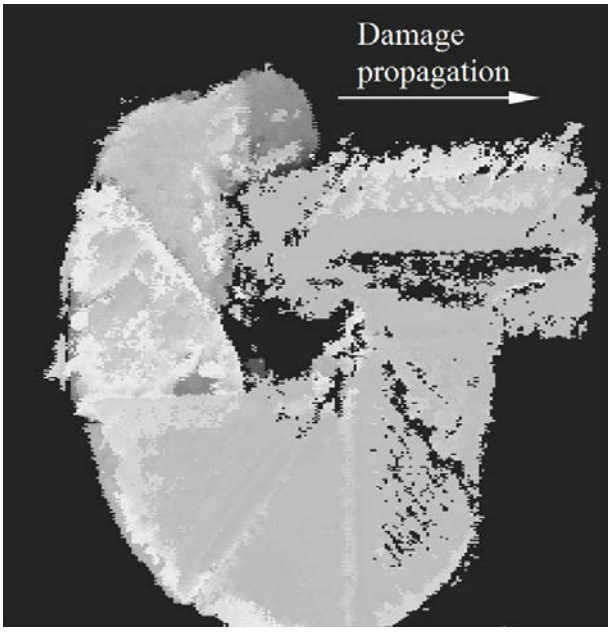

Figure 4.12: C-Scan image for Sp6 damage after 116,000 cycles.

4.2.7 Discussion and conclusions

Impact threshold levels to induce BVID were investigate through a preliminary testing programme for specimens made of $[45/90/-45/0]_{4s}$ laminates. For this purpose, the specimens were impacted by different energy levels. An energy level of 8J was found to be the threshold for the studied quasi-isotropic laminate. The Ultrasonic C-scan images showed a spiral shape damage morphology observed through thickness. Due to the limitation of the scanning technique, the through-thickness scanning was performed using a 35 MHz frequency probe in two steps, from the impact and back surfaces, respectively. Such high frequency allowed uniform reflected signals for small thicknesses. The images showed the damage to be non-symmetric in a form of spiral shape. Whilst specimens Sp1 and Sp2 had a similar damage size, Sp3 included smaller damage dimensions. The smaller damage size in Sp3 was not sufficient to induce a snap-buckling opening during the test. The spiral-stepped damage morphology through the thickness indicated that the snap-buckling initiated from the local area of the damage nearest to the surface under compression. The local damage then extended towards one side of the specimen before reaching the final failure which was characterised by layer separation after the fourth ply from the surface.

The snap-buckling and failure events in both specimens Sp1 and Sp2 took place at similar moment levels. The local separation of layers accompanied by snap-buckling in both specimens Sp1 and Sp2 resulted in 17% less moment at failure compared to the third specimen, Sp3, which exhibited no snap-buckling. The systematic layer separation between the fourth and the fifth layers, i.e. between [0°] and [45°], observed in all specimens, and suggested that such a level was critical under bending loading.

Specimens Sp4 and Sp5, tested under fatigue loading below snap-buckling and showed no evidence for snap-buckling or damage growth in the Ultrasonic C-scan. A visual opening was observed in the third tested specimen, Sp6, as the initial static load advanced above the average snap-buckling moment level. A second fatigue test was performed on Sp4 with a loading cycle passing through snap-buckling moment and ran for one million cycles. The tested specimen showed no evidence of surface opening or damage growth in C-Scan images after the test. Another significant finding from the tested specimens, Sp6 and Sp4-second run, was that the lateral damage dimension is significant in triggering the sub-laminate opening and then delamination growth. Specimen Sp6 had an initial damage with a lateral dimension of 30.5 mm higher than specimen Sp4, which was 27.5 mm. The increased damage size might have triggered the delamination progression, i.e. the lateral damage size is an important factor for the damage progression. The same outcome is supported by static test results as specimens Sp1 and Sp2, which exhibited snap-buckling, had lateral damage dimension of 30 mm and 29.4 mm, respectively. Subsequent C-scan images through the thickness taken for specimen Sp6 showed no evidence of further damage progression after the initial growth taken after 116,000 cycles. This indicates that the impacted laminate is damage tolerant under the described fatigue cycle. Although a circular damage of around 30 mm diameter appeared in C-Scan images, the spiral morphology of the damage triggered only local areas of the damage to extend in a perpendicular direction to the beam longitudinal axis. Another factor, active in suppressing the damage from further progression was the anticlastic curvature attained by bending coupling between the longitudinal and lateral directions. Such a curvature effect might not exist in real structures with high aspect ratio laminated plates, i.e. the small sized specimens may result in conservative behaviour.

4.3 Testing of circular-imbedded delamination laminates under bending

4.3.1 Objectives

Barely visible impact damage, (BVID), is a through-thickness damage characterised by multiple delaminations spread across the thickness. Through literature, strength analyses of composites BVID under compression are performed in the following steps: predicting the size of the damage and then obtaining of compression strength. The different models used to predict the strength of impacted composites were usually calibrated against idealised configuration. This was commonly carried out by assuming one delamination exists within the plate thickness. In this section, a characterisation strategy for circular-imbedded delaminated laminates under bending is presented. Static and fatigue behaviour for single imbedded-circular PTFE delamination specimens are being investigated.

4.3.2 Static testing of circular-imbedded PTFE delamination specimens

Specimens with circular-imbedded PTFE layer were tested under static testing. Pilot tests were initially performed to investigate the likelihood of the sublaminate snap-buckling through changing the depth at which the PTFE should be inserted. Two specimens of 210×50×4 mm dimensions were manufactured with single imbedded-circular PTFE layer of 25 mm diameter. The PTFE layer with a thickness of 12 μmeter was situated in one specimen after the second layer, i.e. the (90°) layer and after the fourth layer in the second specimen, i.e. the (0°) layer. The specimens were statically loaded using the fixture shown in Figure 4.7. The inner and outer rollers were spaced at 65 mm and 185 mm, respectively. Testing speed was chosen for both tests to be 2.25 mm/min. Two strain gauges were attached to both specimens on each surface at the central point. The gauge attached to the top surface was to observe the snap-buckling moment through the change in strain direction. The first specimen with second layer delamination exhibited snap-buckling which consequently gave rise to final failure at a moment level of 1835 Nm/m. The second specimen with the fourth layer delam-

ination showed no snap-buckling until failure was reached at a moment level of 2142 Nm/m. In both specimens, anticlastic effect was clearly observed across the width and layer separation failure was visualised between the fourth and fifth layer. The curves plotted in Figure 4.13 represent the applied moment versus cross-head displacement for the two specimens.

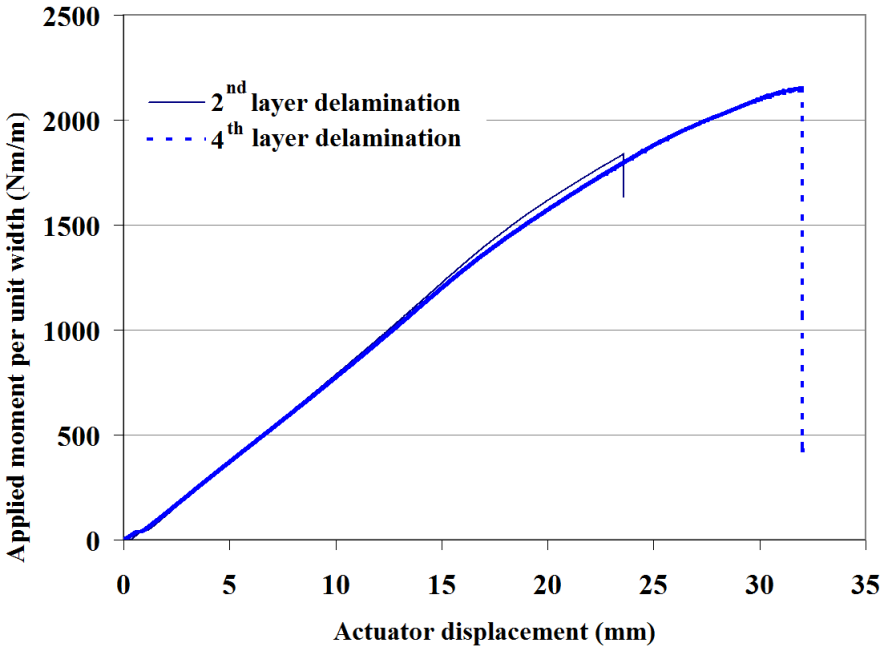

Figure 4.13: Applied moment versus actuator displacement for circular-imbedded delaminated specimens with 25 mm delamination under static testing.

After the pilot test had been carried out, the PTFE layers were placed after the second layer in all the specimens. For the sake of static behaviour evaluation, three specimens with a 31 mm diameter PTFE layer imbedded after the second layer, i.e. the (90°) layer. Specimens dimensions were 210 x W x t mm, presented in Table 4.4. The fixture rollers were fixed at the same distances in the aforementioned pilot study and the test speed was set to 2.25 mm/min.

Snap-buckling opening was only triggered in two specimens. It was observed to locally start at a central spot on the upper surface and then advanced towards one side of the specimen. Figure 4.14 shows a scheme of the damage growth direction post to snap-buckling. The damage emerged on the surface as an elliptic protruded shape with 8 mm width. Table 4.4 presents values of snap-buckling and failure moment levels. The first tested specimen, Sp1 exhibited no snap-buckling until it reached failure. A significant difference existed between both

snap-buckling and failure moment values for the other tested specimens, Sp2 and Sp3.

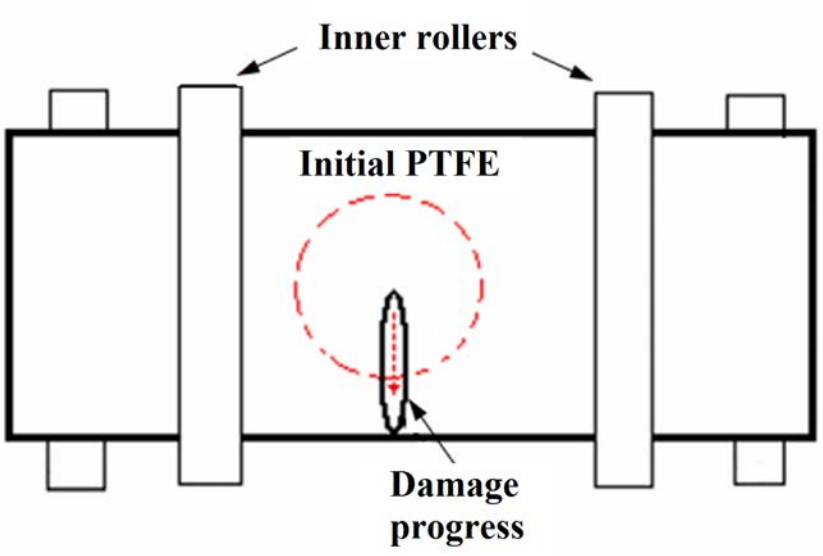

Figure 4.14: Plan view showing damage progress direction for the circular-imbedded delaminated specimen.

Table 4.4: Snap-buckling and failure moment values for circular-imbedded delaminated specimens with 31 mm diameter placed after the 2^{nd} layer

	Width (mm)	Thickness (mm)	Snap-buckling moment (Nm/m)	Failure moment (Nm/m)
Sp1	49.21	4.05	N/A	2235
Sp2	45.50	4.08	1480	1670
Sp3	46.35	4.07	600	1944

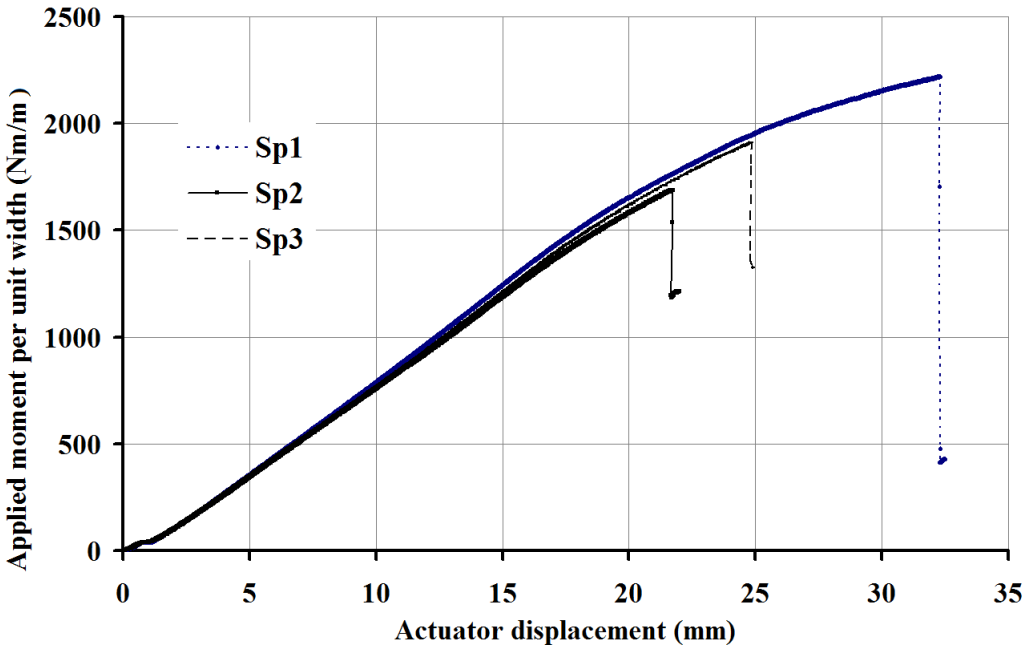

Figure 4.15: Applied moment versus actuator displacement for circular specimens with 31 mm delamination under static testing

4.3.3 Fatigue testing of circular-imbedded PTFE delamination

A fatigue testing programme was ensued following to the aforementioned static testing to investigate the influence of exhibiting a buckled delamination on the fatigue strength compared to static strength of similar tested specimens with circular-imbedded PTFE layer. Several tests were carried out to investigate the fatigue strength of circular-PTFE delaminated specimens. A static loading was initially applied to the specimen in order to induce a snap-buckling of the thin sub-laminate.

A load percentage up to 90% of the average propagation load levels exhibited in Table 4.4 was applied to three circular-imbedded specimens. The tested specimens exhibited anticlastic curvature and no evidence of snap-buckling appeared on the surface, hence the tests were stopped.

4.3.4 Discussion and Conclusions

Following the pilot test, a circular PTFE of 31 mm diameter was placed between second and third layer for the proposed study. Static test results showed significant scatter in the propagation level and snap-buckling moment levels. Snap-buckling of the sub-laminate appeared as a bulge in the upper surface of the specimen. The emerged shape appeared as a semi-cylinder starting from a local area within the circular PTFE and spreading towards one side of the specimen. One specimen with no snap-buckling had a higher propagation moment level compared to those exhibited snap-buckling. The resulting anticlastic curvature on the transverse suppressed the whole separated area from advancing under loading.

The damage progression occurred in the tested specimens was similar to the BVID specimen tested under static loading. Significant difference existed between snap-buckling moment levels and failure moment levels for all tested specimens. Due to the few number of samples, this outcome may need further investigation in order to be strengthed. The failed specimens showed a systematic separation of layers at ply level four in both static and fatigue tests. This suggests that this interface is the weakest one for the $[45/90/-45/0]_{4s}$ laminate under compression loading. Further evidence for such conclusion was provided by the failed circular-PTFE specimens. Although the PTFE was initially placed after the second layer for all specimens, layer separation failure systematically took place after the fourth layer.

Chapter 5

Conclusions, Future Work and Recommendations

5.1 Final conclusions

A study of buckling-driven delaminations under compression and bending loading was presented. The aim of the thesis was to verify the applicability of pre-developed analytical techniques for composite structures. Such tools can be employed in early design stages of composite structures.

Sandwich structures with impact damage were initially investigated under compression. The pre-developed analytical method to predict static failure strain of buckled delamination within a composite plate, [32], showed good correlation with the obtained experimental results. One new aspect in this work was to extend the model application to include sandwich structures assuming the compression load was mostly carried by the faces. The model required the knowledge of the critical depth at which the maximum damage exists. Based on the presented work, the author suggests that such critical depth is consistent for a given laminate at constant impact energy level.

The employment of the digital image correlation technique, DIC, offered a real-time tool to monitor the damage buckling and propagation under load. The damage dimensions devised from the DIC were different from those obtained

using the C-Scan technique. This was due to the fact that the C-Scan technique predicts the boundaries of the damage rather than giving accurate details about the through thickness morphology. While in real life situations, the multiple delamination nature of the damage suggests that the overall behaviour under loading was influenced by the jamming together of the delaminated layers.

On the other hand, the fatigue model, [43], assumed that propagation occurred at the final stages of the fatigue loading. The fatigue threshold strain was based on approximating the damage morphology as a circle encompassing the whole damage observed using the C-Scan technique. Hence, the approximated model was calibrated against the fatigue loading of an impacted sandwich specimen with a $[(\mp 45_C)_2, (90_C, 90_G)_4, (\mp 45_C)_2]$ face laminate. The average maximum damage dimension observed for different impact specimens of the same type was 38 mm. The series of fatigue tests for both tested laminates were performed using a comparatively small number of specimens. Therefore, in order to produce a more accurate characterisation, more specimens should be further tested at different severity levels.

The study of delamination buckling of monolithic laminates under bending was established in two steps: studying through-width delamination struts and then investigating two-dimensional plates. The first step led to a combined analytical model that predicts the buckling, post-buckling and propagation of delaminated composite structures under bending. Both the sub-laminate and the base laminate were assumed to behave like a geometrically nonlinear struts. The predicted propagation moments for unidirectional latminates were within 5% of the experimental values. A significant conclusion established from this study was that the Mode-II fracture was dominant at the delamination fronts under pure bending,

A subsequent study on composite plates under bending was carried out. The impact damage was investigated and the post impact behaviour was studied under static and fatigue loading. A further investigation was carried out on circular-imbedded delaminated plates. The purpose of such investigation was to characterise the static and fatigue behaviour of single delaminations under bending. Such an outcome is substantial for calibrating analytical or numerical models for such problems.

The low-dimensional analytical tools presented in this work have the advantage of being easy to implement in the early design stages of similar types of structures. This would offer industrial engineers an efficient prediction tool for making decisions concerning new parts or modifications earlier to the detail design stages where time-consuming numerical techniques are in use.

5.2 Future work and recommendations

For the sandwich work, such combined analytical-experimental technique can offer a useful tool to explore proposed laminated structures at early design stages. This is can be performed by initially setting up the proposed laminates. The laminated plates are then impacted by the forecasted levels of energy in operative life. The damage is then investigated by sectioning and C-scan techniques. The damage behaviour is then monitored using the DIC system that would give the approximate damage dimensions for different impact energies. Such dimensions could be incorporated into the analytical model [32] to predict the propagation strains for different energy levels.

As concluded from the static test experiment of the sandwich specimen with $[(\mp 45_C)_2, (90_C, 90_G)_4, (\mp 45_C)_2]$ face laminate, damage growth was monitored in two directions, the load and the transverse direction. In order to capture this phenomenon, an analytical tool was further developed by David Lovell, and presented in his final year project. The new analysis examined the concurrent propagation in the load direction and its transverse line by accounting for area change during the propagation. Such tool would be useful to determine the stability condition of the damage growth.

For the case of delaminated beams under bending, the developed analytical tool could be a useful means to establish *Paris* plots, for delaminated layers under bending fatigue. This can be established by obtaining the crack extension rate per cycle, (da/dN), and the fracture toughness component, G, for the delamination. Such information is significant as the fatigue results showed a drop in the crack extension threshold by up to 80%.

The drop in predicting the propagation moment for the quasi-isotropic laminate was due to the bending-twist coupling that appeared during experiments. Such drop suggested the inclusion of new bending stiffness terms to account for this coupling, i.e., D_{13} and D_{33}. The analysis has been introduced in a final year project by Rainer Groh under the supervision of Dr. Richard Butler.

Appendices

Appendix A

Methodology and Experimental Setup

A.1 Impact testing

The composite specimens were impacted on Instron/Dynatup 9250 HV impact machine at the University of Bristol shown in Figure A.1. They were fixed by the fixture shown in Figure A.2. The fixture has a window (75×125mm) and the four arms were for clamping the specimen. To allow for thick sandwich specimens, the clamps were mounted on metallic spacers of similar depth.

Figure A.1: The Instron-Dynatup impact machine.

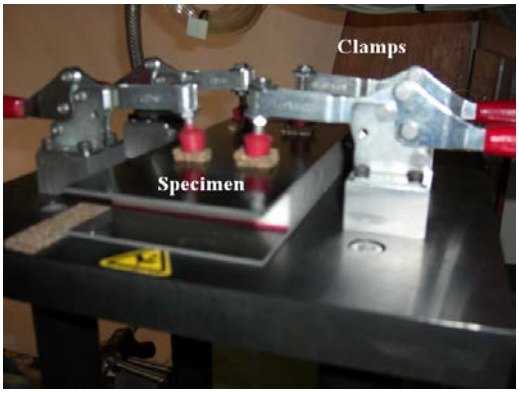

Figure A.2: The impact fixture arrangement.

A.1.1 Theory of working and machine operation

An impactor with a specified weight (W) is set to a height (H) so that the required impact energy is equal to ($W \times H \times g$). The drop energy, impact force, acceleration, and impact time were recorded using the impact software.

The impactor head was attached to a stem piece in order to extend its length to touch the specimen surface. The moving carriage (the load cell) weight was calibrated using the Impulse Test software. The moving carriage was then moved downwards in order to attach it to the falling weight and the weighing process was further repeated for the carriage-falling weight assembly. Each specimen was centred on the steel block and locked in place by the four clamps, so that the impactor hits the centre of the specimen above the window. Two pneumatic shock absorbers were adjusted by adding sufficient metallic spacers in order to ensure a maximum distance of 20 mm against the falling weight at its lowest position.

The crosshead was moved down until the impactor touches the specimen. The velocity flag attached to the crosshead was adjusted so that it just passed the velocity sensor on the side stand. The sensor block was then tightened to the machine stand.

The impactor and the moving crosshead was moved until it slightly touched the surface of the specimen. In the impact software, the displacement meter was set to zero. The specified energy value was entered, so that the machine automatically adjusted the crosshead to the proper height. Before the real test, a dummy specimen with a similar thickness to the real specimen was initially impacted to check the system functioning properly.

A.2 Ultrasonic C-Scan technique

The Ultrasonic C-Scan machine at the University of Bath was used to evaluate the damage within the impacted composite laminates.

Figure A.3: The Ultrasonic C-scan equipment.

The principle of C-Scan ultrasound technique [92], is based on the difference of sound wave speed when passing through different mediums. Generally, sound waves reflect completely at metallic-glass interfaces. Some proportion of the wave energy gets absorbed by the scanned material and then reflects when faceing a new interface, i.e. material-air, material-glass or material-water. Through the difference in time of reflection of the reflected energy levels, the existence of gaps or voids is assessed. The intensity of the reflected energy is equivalent to the thickness of the gap or the damage.

The specimen is placed in the water tank shown in Figure A.3. For sandwich specimens, steel and aluminium blocks were required to attach the specimen to the bottom of the tank using metallic weights. Throughout the work, a 35 MHz probe was employed for composite plate scans. The testing parameters, such as

speed of sound in the medium, probe frequency, filter parameters were accordingly set to suit each specimen type until a sufficient image resolution was attained.

A.3 Manufacturing of composite laminates

The prepreg plies with the designated angle direction were cut into the required length. They were then laid-up according to the laminate. After laying-up a group of eight layers, a bagging vacuum pressure of two bars was applied to ensure a homogenous thickness of the prepreg and to tack it into the tool surface. The vacuum also facilitated the air voids to released towards the surface and hence allowing a solid uniform laminate. A perforated release film was placed on top of the laminate to allow the removal after the curing cycle, at the same time; it helped to release any excess resin from the laminate to the bleeder fabric. The breather fabric was used to uniformly distribute the air pressure by allowing gas flow to escape through its medium. The scheme shown in Figure A.4 presents the manufacturing arrangement. By applying the curing cycle pressure, the excess resin was soaked through the bleeder fabric which produced a homogenised cured laminate. Cork tapes were placed around the laminate to stop any excess resin to flow sidewise and resulting in edgy burrs and sharp corners. The vacuum bag, made from a strong nylon material, was attached to the table using tacky tapes surrounding the setup. Two vacuum valves were installed as shown in the figure to establish a uniform vacuum pressure distribution over the laminate. A thermocouple was inserted through the tacky sealing tape and attached to the laminate in order to obtain an accurate temperature of the laminate throughout the curing cycle.

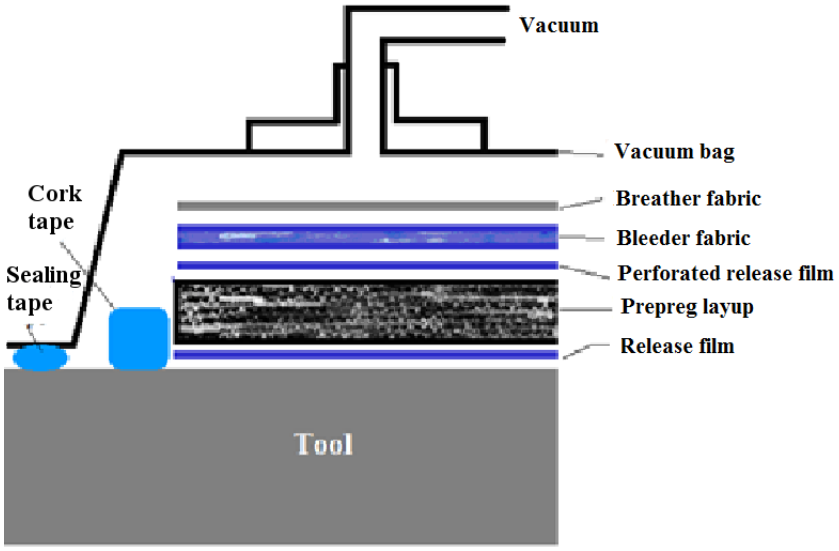

Figure A.4: The laminate setup scheme.

The composite materials used in this study had thermosetting resins, T800 and 8552, were cured under combined temperature and pressure according to the manufacturer data sheets, [93] and [94]. The temperature cycle was to allow homogenous diffusion of the resin through the fibres. The vacuum pressure was to keep a homogenised thickness and to draw the air bubbles from the curing laminate. The computer-controlled autoclave in Figure A.5 was used for the curing cycle implementation. The vacuum valves and thermocouples were attached to the bagged setup and checked before applying the cycle. As the temperature increased, the resin viscosity began to drop and was distributed through the fibres. The temperature dwell allowed enough time for a uniform temperature which incited air bubble release and consolidation of the laminate.

Specimens with M21 and 8552 epoxy resin were cured in an autoclave at the University of Bath. The curing cycle for both resin systems are presented in Figures A.6 and A.7. The heat-up ramps were taken 3°C/min while the cool down rates were set to 5°C/min.

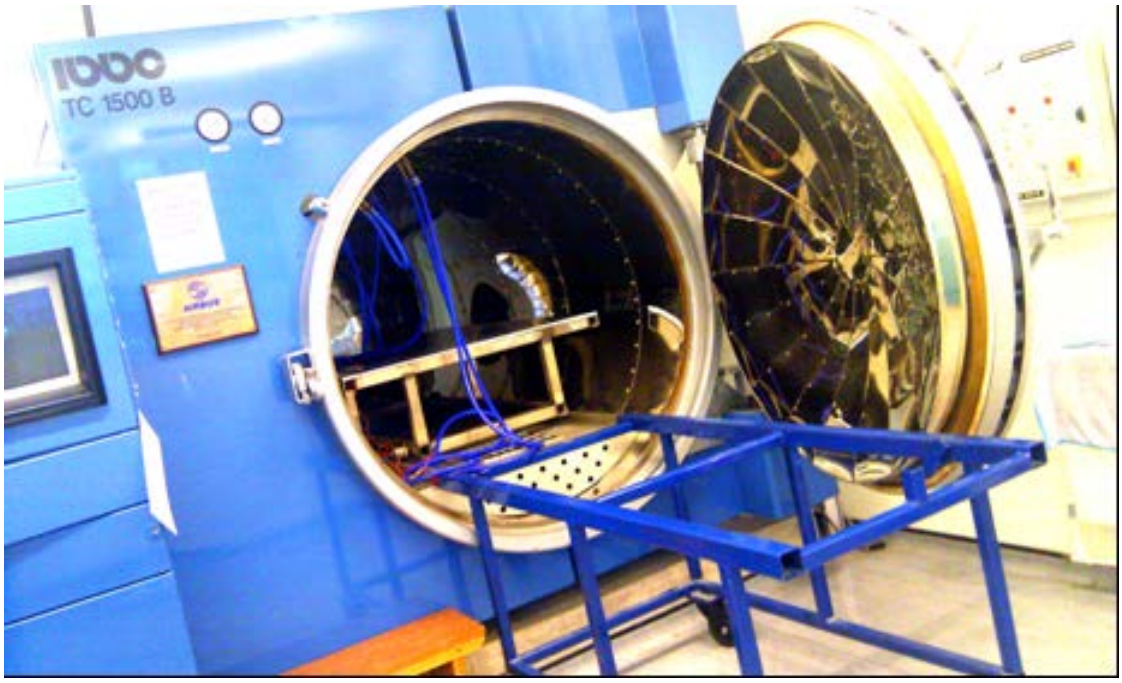

Figure A.5: Curing autoclave.

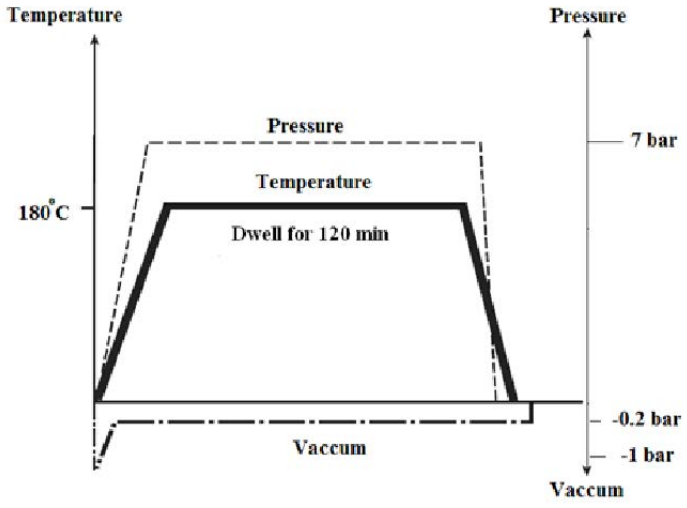

Figure A.6: Curing cycle used for manufacturing the M21 resin specimens.

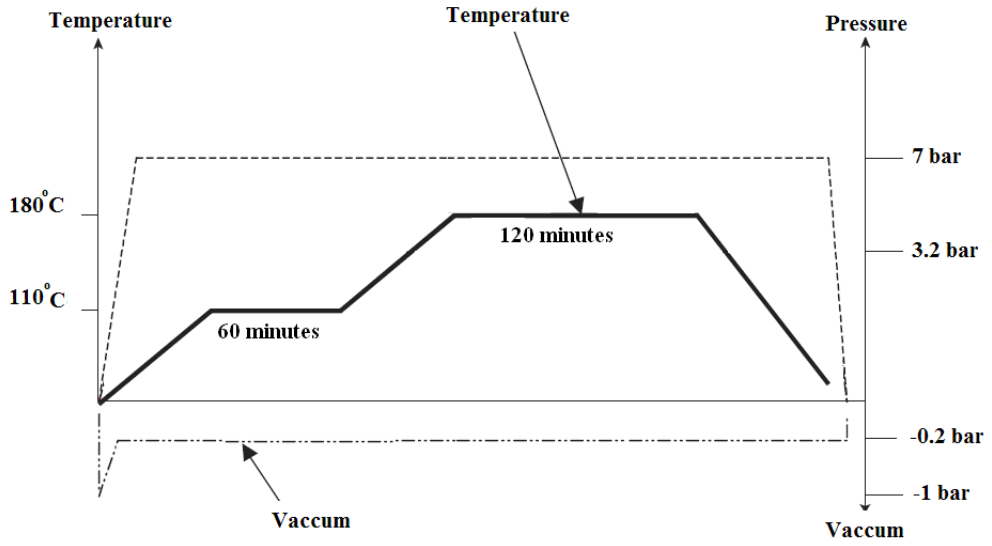

Figure A.7: Curing cycle used for manufacturing the 8552 resin specimens.

A.4 Digital image correlation, DIC

The digital image correlation technique is a non destructive testing method which is based on a mathematical algorithm that helps tracking the changes between similar images for moving objects by identifying the subsequent disposition of specific marked points on the tested surface, see Figure A.8. Two cameras were used to visualise the tested specimen surface from two different directions. By knowing the exact positions of the cameras lenses with respect to each other, the technique can be used to determine the three dimensional location of any point on the tested surface. Hence, a clear distinctive speckle pattern of points should be applied on the surface to ensure the clear interpretation of results. The speckle pattern was commonly painted on the specimen surface in white colour, i.e. white dots on black background.

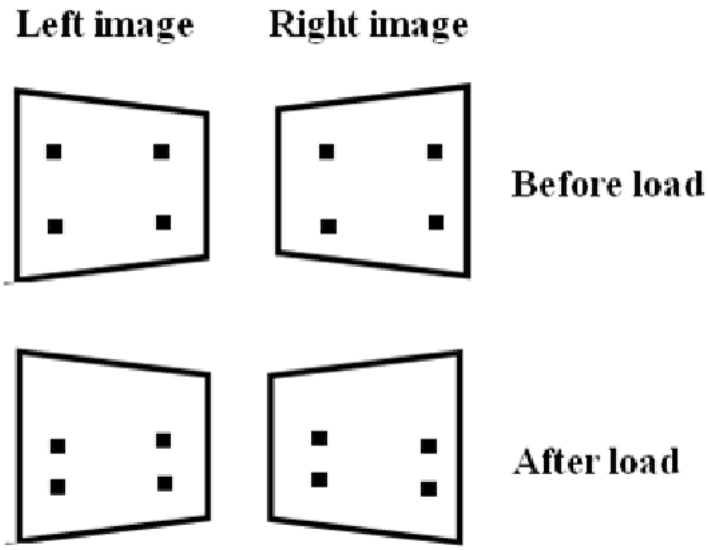

Figure A.8: DIC technique working principle.

The high speed cameras (FASTCAM SA1.1, Photron 192.168.0.11 lens: Nikon AF NIKKOR24 24-85mm 1:2.8-4 D) were utilised to record high resolution images during the subsequent deformation of the specimen under loading. The DIC camera setup is shown in Figure A.9. The images were then analysed through image processing software, (VIC3D-2007). The software was initially used to identify a reference image (usually taken at the zero load condition) which was later used to correlate the position of the speckle pattern in the subsequent images taken at different loads. The software algorithm calculated different deformation parameters for the studied surface with the speckle pattern on. Surface strains, displacements in the three different coordinates, x y z were obtained. In the current study, the DIC technique was used in monitoring the deformation of the delaminated area and the difference between such behaviour and any overall deformation of the specimen.

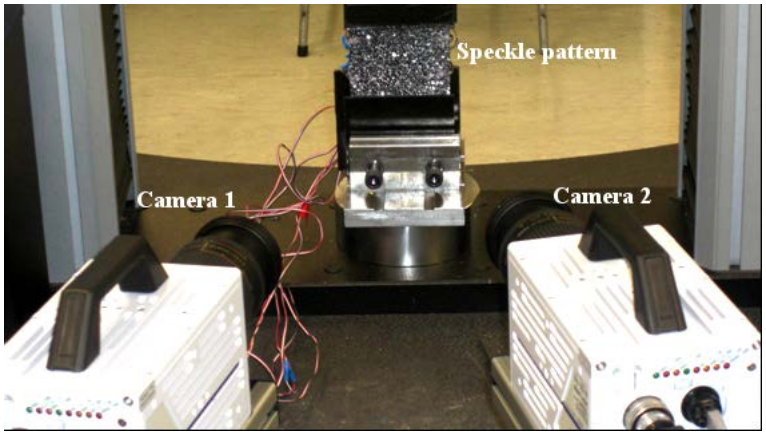

Figure A.9: A test setup using the DIC system.

A.5 Strain gauge installation procedures

Vishay Micro-measurements single axis strain gauges of 350 Ω and a gauge factor of GF=2.1 were used throughout the current study. The current procedure explains the steps to attach them on the tested specimens.

Attaching a strain gauge requires the following definite steps: The epoxy composite surface should be slightly sanded and cleaned using an emery sand paper in the order of 180, 320, and 400 grit, respectively. A careful force application was considered during the sanding process to avoid excessive removal of the hardened epoxy matrix and decreasing the overall thickness of the surface which would result in strain increase at the gauge spot. After finishing, the matrix debris and remains should be cleaned using wet wipes. A subsequent surface degreasing was performed using an alcohol wetted gauze sponge that helped picking any remnant epoxy or fibre debris from the surface. The sponge was used in a one-way stroke manner in order not to bring back any debris from neighbourhood areas. An M-prep conditioner was slightly brushed on the cleaned spot. It helped in establishing a better bond between the adhesive, the gauge and the surface. Positioning marks were plotted nearest to the approximate gauge position in order to facilitate alignment. The strain gauge was picked from its package by a tweezers and then placed on the sticky side of a PCT-2M Gauge installation tacky tape (3/4" wide) that was pre cut and placed on the working table. Such placement ensured easy handling and placement of the gauge. A similar procedure was re-

peated in order to place the connector terminal. The conditioner was brushed on both the gauge and the connector surfaces and then let them to dry for a few minutes. The tape was attached to the specimen surface from one side, slightly further from the gauge spot, while keeping the other end un-tacked. Small drops of Vishay M-Bond 200, strain gauge adhesive, were gently added at the tape junction with the surface. The other tape end was kept stretched and adjusted until good alignment with the marked positions on the surface is ensured. A thumb stroke was applied from the attached side of the tape towards the end in order to distribute a homogenous layer of the adhesive throughout. The pressure was maintained for two minutes for adhesive curing.

The tape was finally removed from the surface in order to expose the gauge and the connector. The connector pads on both the gauge and the terminals were slightly abraded using a 400 grit emery paper so as to scratch the surface and improve the adhesion with the soldering tin. The iron was heated up and used to melt the soldering wire and place small drops on each connecting pad. The connecting wires were cut into sufficient lengths and the ends were then stripped of the isolating layer to allow efficient attachment to the pads. Each wire terminal was connected to each pad using the soldering iron to melt the tin on the pads.

Appendix B

Published and presented articles from the current work

Conference papers

M. Kinawy and R. Butler, "Face damage growth of sandwich composites under compressive fatigue loading", 17^{th} International Conference on Composite Materials (ICCM-17), 27-31 July 2009, Edinburgh, UK.

M. Kinawy, R. Butler and G. W. Hunt, "Buckling and propagation of a delaminated composite beam in bending", AIAA 51^{st} SDM conference, May 2010, Orlando, Florida, USA.

Published articles

M. Kinawy, R. Butler and G. W. Hunt, "Bending strength of delaminated aerospace composites", Philosophical Transactions of The Royal Society A: Geometry and Mechanics of Layered Structures and Materials, 2011 - (accepted for publication)

M. Kinawy, R. Butler and G.W. Hunt, "Buckling and postbuckling of a delaminated composite beam in bending", 2011, AIAA Journal, 49 (3), pp. 670-672.

References

[1] H.T. Hahn and O. Turkgenc. The effect of loading parameters on fatigue of composite laminates part v", dot/faa/ar-01/24. Technical report, Department of Transportation, Federal Aviation Administration, Office of Aviation Research, Washington, D.C. 20591, U.S., 2001.

[2] G. A. Bibo and P. J. Hogg. The role of reinforcement architecture on impact damage mechanisms and post-impact compression behaviour,. *Journal of Materials Science*, 31:1115–1137., 1996.

[3] G. A. Bibo and P. J. Hogg. Influence of reinforcement architecture on damage mechanisms and residual strength of glass-fibre/epoxy composite systems. *Composites Science and Technology*, 58:803–813, 1998.

[4] E. Greenhalgh, S. Singh, D. Hughes, and D. Roberts. Impact damage resistance and tolerance of stringer stiffened composite structures. *Plastics Rubber and Composites*, 28, No.5:228–251, 1999.

[5] H.Y. Choi and F.-K. Chang. A model for predicting damage in graphite/epoxy laminated composites resulting from low-velocity point impact. *Journal of Composite Materials*, 26(14):2134–2169, 1992.

[6] C. Bouvet, B. Castanie, and J-J. Barrau. Modelling of impact damage in laminated composites. In *13th European Conference on Composite Materials, ICCM-13, Stockholm, Sweden.*, June 2008.

[7] M. De Freitas, A. Silva, and L. Reis. Numerical evaluation of failure mechanisms on composite specimens subjected to impact loading. *Composites: Part B*, 31:199–207, 2000.

[8] G. A. O. Davies and X. Zhang. Impact damage prediction in carbon composite structures. *International Journal of Impact Engineering*, 16(1):149 – 170, 1995.

[9] D.R. Ambur and J. H. Jr. Starnes. Effect of curvature on the impact damage characteristics and residual strength of composite plates. In *39th AIAA/ASME/ASCE/AHS/ASC Structures, Structural Dynamics, and Materials Conference, Long Beach, California.*, 1992.

[10] K. Shivakumar, A. Dora, and F. Abali. interlaminar shear test for laminated textile fabric composites. In *International Conference on Composites Materials*, ICCM 13, Beijing, China, 2001.

[11] ASTM-D2344. Standard test method for short-beam strength of polymer matrix composite materials and their laminates. *ASTM*, 2006.

[12] ASTM D3846. Standard test method for in-plane shear strength of reinforced plastics.

[13] M. Elawadly, K. On the interlaminar shear stress response for e-glass/epoxy composite. *Journal of Composite Materials*, 37(23):2149–1258, 2003.

[14] L.G. Melin and J. Schön. Buckling behaviour and delamination growth in impacted composite specimens under fatigue load: an experimental study. *Composites Science and Technology*, 61(13):1841 – 1852, 2001.

[15] A. S. Chen, D. P. Almond, and B. Harris. In situ monitoring in real time of fatigue-induced damage growth in composite materials by acoustography. *Composites Science and Technology*, 61(16):2437 – 2443, 2001.

[16] H. Chai, W. G. Knauss, and C. D. Babcock. Observation of damage growth in compressively loaded laminates. *Journal of Experimental Mechanics*, 23(3):329–337, 1983.

[17] M. Kharazi, H.R. Ovesy, and M. Taghizadeh. Buckling of the composite laminates containing through-the-width delaminations using different plate theories. *Composite Structures*, 92(5):1176 – 1183, 2010.

[18] W. J. Bottega and A. Maewal. Delamination buckling and growth in laminates. *Journal of Applied Mechanics*, 50, 1, 1983.

[19] B.D. Davidson. Delamination buckling. theory and experiment. *Journal of Composite Materials*, 25(10):1351–1378, 1991. cited By (since 1996) 30.

[20] G. J. Short, F. J. Guild, and J. Pavier, M. The effect of delamination geometry on the compressive failure of composite laminates. *Composite Science and Technology*, 61:2075–2086, 2001.

[21] H. Chai, C.D. Babcock, and W. Knauss. One dimensional modelling of failure in laminated plates by delamination buckling. *International Journal of Solids and Structures*, 17:1069–1083, 1981.

[22] H. Chai and C.D. Babcock. Two-dimensional modelling of compressive failure in delaminated laminates. *Journal of Composite Materials*, 19:67–98, 1985.

[23] G. Flanagan. Two dimensional delamination growth in composite laminates under compression loading. In J. D. Whitcomb, editor, *Composite Materials: Testing and Design (Eighth Conference),*, ASTM STP 972, pages 180–190, Philadelphia, USA, 1988. American Society for Testing and Materials.

[24] B. Shan and A Pelegri. Approximate analysis of the buckling behavior of composites with delamination. *Journal of Composites Materials*, 37:673–685, 2003.

[25] J. D. Whitcomb. Parametric analytical study of instability-related delamination growth. *Composites Science and Technology*, 25(1):19 – 48, 1986.

[26] C. S. Yerramalli and A. M. Waas. A nondimensional number to classify composite compressive failure. *Journal of Applied Mechanics*, 71(3):402–408, 2004.

[27] G.A. Kardomateas. The initial post-buckling and growth behavior of internal delaminations in composite plates. *Journal of Applied Mechanics*, 60:903, 1993.

[28] S. J. Britvek. *The Stability of Elastic Systems*. Pergamon, New York., 1973.

[29] Z. Suo and J. W. Hutchinson. Interface crack between two elastic layers. *International Journal of Fracture*, 43:1–18, 1990. 10.1007/BF00018123.

[30] G.W. Hunt, B. Hu, R. Butler, Almond D.P., and Wright J.E. Nonlinear modeling of delaminated struts. *AIAA Journal*, 42(11):2364–2372.

[31] J.E. Wright. Compound bifurcations in the buckling of a delaminated composite strut. *Nonlinear Dynamics*, 43:59–72, 2006.

[32] A.T. Rhead and R. Butler. Compressive static strength model for impact damaged laminates. *Composite Science and Technology*, 69 (14):2301–2307, 2009.

[33] N. Uda, K. Ono, and K. Kunoo. Compression fatigue failure of cfrp laminates with impact damage. *Composites Science and Technology*, 69(14):2308 – 2314, 2009. The Sixteenth International Conference on Composite Materials with Regular Papers.

[34] A.R. Rhead, D. Marchant, and R. Butler. Compressive strength of composite laminates following free edge impact. *Composites Part A: Applied Science and Manufacturing*, 41(9):1056 – 1065, 2010. Special Issue on 10th Deformation & Fracture of Composites Conference: Interfacial interactions in composites and other applications.

[35] F.W. Williams, M.S. Anderson, D. Kennedy, R. Butler, and G. Aston. User manual for viconopt. 1990.

[36] R.L. Ramkumar. Effect of low velocity damage on the fatigue behaviour of graphite epoxy laminate. In *Long term behaviour of composites, ASTM STP813, 116-135.*, pages 116–135, 1983.

[37] M. H. Beheshty and B. Harris. A constant life model of fatigue behaviour for carbon-fibre composites: the effect of impact damage. *Composites Science and Technology*, 58:9–18, 1998.

[38] M. H. Beheshty and B. Harris. An empirical fatigue-life model for high performance fibre composites with and without impact damage. *part A: Applied Science and Manufacturing*, 30:971–987, 1999.

[39] R. Jones, J.F. Williams, and T. E. Tay. Is fatigue testing of impact damaged laminates necessary?. *Composite Structures*, 8:1–12, 1987.

[40] D. G. Katerelos, A. Paipetis, and V. Kostopoulos. A simple model for the prediction of the fatigue delamination growth of impacted composite panels. *Fatigue and Fracture of Engineering Materials and Structures*, 27(10):911–922, 2004.

[41] M. De Freitas and R. De Carvalho. Residual strength of a damaged laminated cfrp under compressive fatigue stresses. *Composite Science and Technology*, 66:373–378, 2006.

[42] R. Butler, D.P. Almond, G.W. Hunt, B. Hu, and N. Gathercole. Compressive fatigue limit of impact damaged composite laminates. *Composites Part A: applied science and manufacturing*, 38:1211–1215, 2007.

[43] A. Rhead, R. Butler, and G.W Hunt. Post-buckled propagation model for compressive fatigue of impact damaged laminates. *International Journal of Solids and Structures*, 38:4349–4361, 2008.

[44] P.T. Curtis, J. Gates, and C.G. Molyneux. Impact damage growth in carbon fibre composites. *Defence Research Agency, Farnborough, Hampshire, Technical Report 93009*, 1993.

[45] J.I. Rome, P.M. Schubel, V.K. Goyal, and J. Tuck-Lee. Predicting compression-after impact strength of composite sandwich structures. In *AIAA/ASME/ASCE/AHS/ASC Structures, Structural Dynamics, and Materials 7-10, Schaumburg, IL*, 2008.

[46] C. Kassapoglou. Buckling, post-buckling and failure of elliptical delaminations in laminates under compression. journal of composite structures. *Journal of Composite Structures*, 9:139–159, 1988.

[47] C. Kassapoglou and Abbott R. A correlation parameter for predicting the compressive strength of composite sandwich panels after low speed impact. In *AIAA-1988-2294, Structures, Structural Dynamics and Materials Conference, 29th*, number AIAA-1988-2294, pages 642–650, Williamsburg, VA,, Apr 18-20 1988. AIAA.

[48] D.R. Ambur and Cruz J. Low-speed impact response characteristics of composite sandwich panels. In *36th AIAA/ASME/ASCE/AHS/ASC SDM-Conference, AIAA 95-1460-CP,4, 2681-2689*, 1995.

[49] G.A. Kardomateas. Postbuckling characteristics in delaminated kevlar/epoxy laminates: an experimental study. *Journal of Composites Technology and Research (ASTM)*, 12(2):85–90, 1990.

[50] F. Edgren and L.E. Asp. Compressive failure of impacted ncf composite sandwich panels characterisation of the failure process. *Journal of Composite Materials*, 38(6):495–514, 2004.

[51] M. W. Czabaj, A.T. Zehnder, B.D. Davidson, A.K. Singh, and D.P. Eisenberg. Compression after impact of sandwich composite structures: Experiments and modeling. In *51st AIAA/ASME/ASCE/AHS/ASC Structures, Structural Dynamics, and Materials Conference¡BR¿ 18th 12 - 15 April 2010, Orlando, Florida*, 2010.

[52] N.A. Fleck and I. Sridhar. End compression of sandwich columns. *Composites Part A*, 33:353–359, 2002.

[53] N. Kulkarni, H. Mahfuz, S. Jeelani, and L.A. Carlsson. Fatigue crack growth and life prediction of foam core sandwich composites under flexural loading. *Composite Structures*, 59(4):499 – 505, 2003.

[54] M. Burman and D. Zenkert. Fatigue of foam core sandwich beams–1: undamaged specimens. *International Journal of Fatigue*, 19(7):551 – 561, 1997.

[55] D. Zenkert and M. Buruman. Compression and shear fatigue of a closed cell foam. In *16th International Conference on Composite Materials, Kyoto, Japan*, 2007.

[56] B. Freeman, E. Schwingler, M. Mahinfalah, and K. Kellogg. The effect of low-velocity impact on the fatigue life of sandwich composites. *Composite Structures*, 70(3):374 – 381, 2005.

[57] A. Shipsha, S. Hallstrm, and D. Zenkert. Failure modelling of impact damage in sandwich beams- a 2d approach: Part i experimental investigation. *Journal of Sandwich Structures and Materials*, 5(1):7–31, 2003.

[58] G. A. Kardomateas and H. Huang. The initial post-buckling behavior of facesheet delaminations in sandwich composites. *Journal of Applied Mechanics*, 70:191–199, 2003.

[59] G.A. Kardomateas. Snap buckling of delaminated composites under pure bending. *Journal of Composites Science and Technology*, 39:63–74, 1990.

[60] K. Dransfield, C. Baillie, and Y Mai. Improving the delamination resistance of cfrp by stitching–a review. *Composites Science and Technology*, 50(3):305 – 317, 1994.

[61] W.b. Wang, R. A. Shenoi, and C. W. Cheng. Delamination buckling of a curved composite beam subjected to a closing bending moment. *Jounal of Ship Mechanics*, 10 No.6:102–114, 2006.

[62] T.J. Lu, Z.C. Xia, and J. W. Hutchinson. Delamination of beams under transverse shear and bending. *Materials Science and Engineering,*, A188:103–112, 1994.

[63] T. K. O'Brien. Development of a composite delamination fatigue life prediction methodology. Technical Report LF99-9386, Langley Research Center, 2009.

[64] B.D. Davidson and W. Zhao. An accurate mixed-mode delamination failure criterion for laminated fibrous composites requiring limited experimental input. *Journal of Composite Materials*, 41, 6:679–702, 2007.

[65] G. Matsubara, H. Ono, and K. Tanaka. Mode-ii fatigue crack growth from delamination in unidirectional tape and satin-woven fabric laminates of high strength gfrp. *International Journal of Fatigue*, 28:1177–1186, 2006.

[66] J.G. Williams. A review of the determination of energy release rates for strips in tension and bending: Part i - static solution. *Journal of Strain Analysis*, 28(4), 1993.

[67] Y Kim, J.F. Davalos, and E. Barbero. Delamination buckling of frp layer in laminated wood beams. *Composite Structures*, 37(3-4):311 – 320, 1997.

[68] L. E. Asp, A. Sjogren, and E.S. Greenhalgh. Delamination growth and thresholds in a carbon/epoxy composite under fatigue loading. *Journal of Composites Technology and Research, American Society for Testing and Materials*, 23 issue 2:55–68, 2001.

[69] R.J. Rothschilds, J.W Gillespie, and L.A. Carlsson. Instability-related delamination growth in thermoset and thermo-plastic composites. In J. D. Whitcomb, editor, *Proceeding of Composite Materials: Testing and Design Conference, ASTM STP 972*, 1988.

[70] B. Shan and A. Pelegri. Assessment of the fracture behavior of an asymmetrically loaded cantilever composite structure. *Journal of Engineering Materials and Technology*, 125:353–360, 2003.

[71] K. Tanaka and H. Tanaka. Stress-ratio effect on mode-ii propagation of interlaminar fatigue cracks in graphite/epoxy composites. In E.A. Armanios, editor, *Composite Materials: Fatigue and Fracture*, volume 6 of *ASTM*, pages 126 –142. American Society for Testing and Materials, 1997.

[72] W. Wang and R. A. Shenoi. Delamination modelling of a curved composite beam subjected to an opening bending moment. *Journal of Strain Analysis*, 38(5):453–457, 2003.

[73] J.G. Williams. On the calculation of energy release rates for cracked laminates. *International Journal of Fracture*, 36, 2:101–119, 1988.

[74] F. Kosel, J. Petrisic, B. Kuselj, T. Kosel, V. Sajn, and M. Brojan. Local buckling and debonding problem of a bonded two-layer plate. *Archive of Applied Mechanics*, 74:704–726, 2005. 10.1007/s00419-005-0381-x.

[75] W. Fang and J. A. Wickert. Post buckling of micromachined beams. *Journal of Micromechanics and Microengineering*, 4, Number 3:116–122, 1994.

[76] J. Wang and P. Qiao. Fracture analysis of shear deformable bi-material interface. *Journal of Engineering Mechanics*, 132, 3:306–316, 2006.

[77] J. W. Hutchinson and Z. Suo. Mixed mode cracking in layered materials. In Academic Press, editor, *Advances in Applied Mechanics*, volume 29, pages 63–191, 1992.

[78] V. V. Bolotin and S.V. Nefedov. Growth of thin delamination in laminate composite beams under cyclic bending. *Mechanics of Composite Materials and Structures*, 3:275–295, 1996.

[79] K.D. Murphy and J.M. Nichols. A low-dimensional model for delamination in composite structures: Theory and experiment. *International Journal of Nonlinear Mechanics*, 45:13–18, 2008.

[80] W. Yin. The effects of laminated structure on delamination buckling and growth. *Jounal of Composite Materials*, 22:502–517, 1988.

[81] N.A. Warrior, A.K. Pickett, and N.S.F. Lourenco. Mixed-mode delamination - experimental and numerical studies. *Journal of Strain Analysis*, 39:153–159, 2003.

[82] A. Dobbinson. Evaluation of impact damage in composite sandwich structures using nde techniques and sectioning.

[83] L.A. Carlsson and G.A. Kardomateas. *Structural and Failure Mechanics of Sandwich Composites*. Springer, 2011.

[84] ASTM C364-99. Standard test method for edgewise compressive strength of sandwich constructions. Technical report, Annual Book of ASTM Standards, American Society for Testing and Materials, Vol.15.03, 1996.

[85] E.S. Greenhalgh. *Failure Analysis and Fractography of Polymer Composites*. Woodhead Publishing Limited, Cambridge, UK.

[86] Standard test method for mode i interlaminar fracture toughness of unidirectional fiber-reinforced polymer matrix composites. 2007.

[87] J. M. Thompson and G. W. Hunt. *A General Theory of Elastic Stability*. 1973.

[88] R. Zitoune and F. Collombet. Numerical prediction of the thrust force responsible of delamination during the drilling of the long-fibre composite structures. *Composites Part A: Applied Science and Manufacturing*, 38(3):858 – 866, 2007.

[89] C. Bouvet, S. Rivallant, and J. Barrau. Modelling of impact damage and permanent indentation on laminate composite plate. In *ECCM14 - 14th European Conference on Composite Materials*, June 2010, Budapest, Hungary.2010.

[90] M. Ilyas. *Damage Modeling of Carbon/Epoxy laminated composites submitted to impact loading*. PhD thesis, L Universite De Toulouse, July 2010.

[91] M. May and S.R. Hallett. A combined model for initiation and propagation of damage under fatigue loading for cohesive interface elements. *Composites Part A: Applied Science and Manufacturing*, 41,12:1787–1796, August 2010.

[92] C.J. Hellier. *Handbook of nondestructive evaluation*. McGraw-Hill, 2003.

[93] Hexcel corporation. Hexply m21 epoxy resin product data sheet.

[94] Hexcel corporation. Hexply 8552 epoxy resin product data sheet.